



FACULTY OF MEDICINE
DOCTORAL PROGRAM IN MEDICAL SCIENCES

**NANOPARTICLE USE FOR THE STUDY OF EXOSOME TRANSPORT TO
THE BRAIN THROUGH THE LYMPHATIC PATHWAY**

By

HÉCTOR MIGUEL RAMOS ZALDÍVAR

Thesis presented to the Faculty of Medicine of the Pontificia Universidad Católica de Chile to obtain the degree of Doctor in Medical Sciences

Tutor: Marcelo Andía

Cotutors: Alejandro Corvalán

Iva Polakovicova

Marcelo Kogan

December, 2022

Santiago, Chile

©2022, Héctor Miguel Ramos Zaldívar

©2022, Héctor Miguel Ramos Zaldívar

This license authorizes the partial or complete reproduction of this material, for academic purposes, for any media or procedure, by including the citation of this document.

AUTORIZACIÓN PARA LA REPRODUCCIÓN DE LA TESIS

(SELECCIONE UNA OPCIÓN)

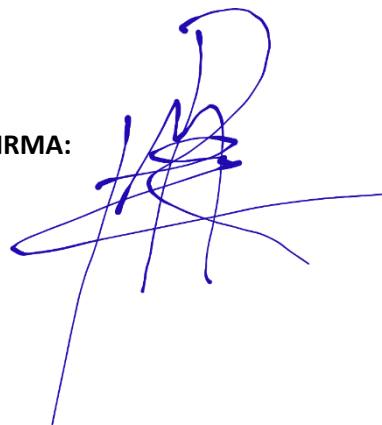
a) Ninguna parte de esta tesis puede reproducirse o transmitirse bajo Ninguna forma o por ningún medio o procedimiento, sin permiso por Escrito del(os) autor(es).

FECHA----- FIRMA

b) Se autoriza la reproducción total o parcial, con fines académicos, por cualquier medio o procedimiento, incluyendo la cita bibliográfica que acredita al trabajo y a su autor.

FECHA: 28 de Diciembre, 2022

FIRMA:

A handwritten signature in blue ink, consisting of several overlapping loops and lines, positioned to the right of the 'FIRMA:' label.

**To my son Santiago and my wife Karla, for the love of waking up to your voices,
the inspiration of chasing dreams by your side, and the beauty of praying together
at night.**

“¿Papá, hoy vas a ir a hacer un experimento?”

Santi

ACKNOWLEDGEMENTS

First, I thank God for guiding my journey to Chile and giving me the life, health, and the blessing of surrounding my path with extraordinary individuals that have taught me everything to achieve this dream. For allowing me to meet Dr. Corvalán and Dr. Iva Polakovicova, the day when our worlds and stories gathered to spark a new idea that has found its way to the pages of this thesis.

I thank my son Santiago and my wife Karla, who support me in every way possible and fill my days with joy and life. My mom and dad (María and Miguel), whose words have encouraged me to never give up, always allow my soul to dream, and work as hard as an idea requires, not for myself but as an instrument of God. My sister Kathy, for her support and her assistance in image quality supervision. My parents-in-law (Ivin and Sergio) and my siblings-in-law (German and Carol) for their constant support, wisdom, and love.

I thank my tutor Marcelo Andia, whose wisdom and support in every step of the project has been immeasurable. I thank my cotutors Alejandro Corvalán and Marcelo Kogan, for their guidance and expertise. To all of you for allowing me into your laboratories and teams and to make me feel part of your research family, in different campuses of the Pontificia Universidad Católica de Chile and the Universidad de Chile.

I am grateful to Edison Salas, for his support in iron nanoparticle preparation and characterization, designing experiments, and for giving me the opportunity to visit AINTECH to work on this project, even during the hardships of a pandemic. To Dr. Claudia Yefi, for her guidance in anatomical preparation for animal experiments, during mice surgeries, and in Western blot characterization. For welcoming me in the Veterinary Medicine Department, where knowledge is expanded with every visit on the marvels of the many forms and strategies that life can manifest. To Carlos Martínez for his assistance during mice anesthesia and care.

My gratitude to David Silva for his valuable work in histological analysis. To Ana Riveros for her assistance during electron microscopy. To Pedro Jara and Francisco Morales for their support in gold nanoparticle preparation and CT image discussion. To Dr. Patricia Burgos for her collaboration at Universidad San Sebastián. To Dr. Sergio Alvarez laboratory for his collaboration with electroporation procedures.

Special thanks to Wilda, Pablo, Andrés, Ignacio, Keila, Graciela, Carolina, María José, Alejandra, Natalia, Victor, Álvaro, Rocío, Leticia, Laura Parra, Laura Manjarres, Katherine, Juan Esteban, Camila, Karen, Daniela, Ingrid, Eloisa, Viviana, Miguel, Cristian. For the science, the advice, the teachings, the laughs, and your friendship.

To Dr. Jaime Núñez, Dr. Edwin Herrera, Dr. Benjamin Mena, and Dr. Misael Arguijo for encouraging me in this scientific journey to explore life and God's creation, since my early years as a medical student.

To the Universidad Católica de Honduras, Vicerrectoría de Investigación UC, Escuela de Medicina UC, and ANID BECAS/DOCTORADO NACIONAL 21211334, for their financial support at different stages of my doctoral program.

I thank the Program Chiefs that have led the enormous responsibility of the Doctoral Program of Medical Sciences, allowing us to develop our potential in the best environment possible: Dr. Jaime Pereira, Dra. Claudia Sáez, Dra. Silvana Zanlungo, Dr. Jorge Carvajal, Dra. Andrea Leiva, Dra. Carolina Bizama.

To my Evaluation Committee, Dr. Mauricio Cuello and Dr. Flavia Zacconi, for all their incredibly valuable scientific revisions and advice that improved every aspect in the development and reporting of this work.

Finally, this work is dedicated to the life and memory of Dr. Iva Polakovicova. I will be forever grateful for her mentoring and friendship. The impact of her science will live through generations.

Table of Contents

DEDICATION	iv
ACKNOWLEDGEMENTS	v
Abstract	x
Chapter 1: Introduction.....	1
1.1 Exosomes and current hypotheses on their brain uptake	1
1.2 The blood brain barrier pathway hypothesis	4
1.2.1 <i>In vitro</i> models.....	4
1.2.2 Evaluation of uptake and transcytosis	6
1.2.3 <i>In vivo</i> evaluations of the BBB hypothesis for EVs	12
1.3 The choroid plexus hypothesis.....	16
1.4 The lymphatic pathway	16
Chapter 2: Hypothesis and Objectives	19
Hypothesis.....	19
General Objective.....	19
Specific objective 1: To prepare nanoparticle-loaded exosomes:	19
Specific objective 2: To administer nanoparticle-loaded exosomes in mice via the lymphatic system, employing magnetic resonance imaging for their evaluation on the cervical and central nervous system tissues.	19
Specific objective 3: To validate through histological analysis the presence of nanoparticle-loaded exosomes in the meningeal lymphatic vessels.	20
Chapter 3: Methods	21
3.1 For specific objective 1a: To synthesize iron nanoparticles and stabilize them with polyethylene glycol, polyvinylpyrrolidone, or citrate to optimize incorporation into cells and exosomes.	21
3.1.1 Iron oxide nanoparticle synthesis	21
3.1.2 Characterization of iron oxide nanoparticles.....	22
3.2 For specific objective 1b: To prepare B16F10 derived exosomes loaded with iron nanoparticles.....	22
3.2.1 Exosome purification.....	22
3.2.2 Nanoparticle internalization to exosomes	23
3.2.3 Characterization of exosomes.....	23
3.3 For specific objective 1c: To evaluate the cell viability of SH-SY5Y cells exposed to nanoparticles and loaded exosomes.....	23
3.3.1 Cell viability assay.....	23

3.4 Three stages were developed for specific objective 2: To administer nanoparticle-loaded exosomes in mice via the lymphatic system, employing magnetic resonance imaging for their evaluation on the cervical and CNS tissues.	24
3.4.1 Stage I	24
3.4.2 Stage II	25
3.4.3 Stage III	27
3.4.4 Gold nanoparticle synthesis	29
3.4.5 Characterization of gold and Chinese ink nanoparticles.....	30
3.5 For specific objective 3: To validate through histological analysis the presence of nanoparticle-loaded exosomes in the meningeal lymphatic vessels.....	31
3.5.1 Formalin-fixed, paraffin-embedded (FFPE) tissue processing for histology and special stains	31
3.6 Animals.....	32
3.7 Statistical Analysis	32
Chapter 4: Results	33
4.1 Specific objective 1a.....	33
4.1.1 SPIONs characterization for 1.5 T MRI	33
4.1.2 Optimal concentration of SPIONs for 1.5 T MRI signal detection	34
4.2 Specific objective 1b.....	38
4.2.1 Exosome purification and characterization	38
4.2.2 SPION functionalization and characterization for exosome loading	40
4.2.3 Exosome loading with SPIONs.....	42
4.3 Specific objective 1c	44
4.4 Specific objective 2a.....	45
4.4.1 Mice intracerebroventricular injection of Evans Blue dye.....	45
4.5 Specific objective 2b.....	46
4.5.1 Mice deep cervical lymph node injection with Evans Blue dye	46
4.5.2 Mice intracerebroventricular injection of Chinese ink.....	47
4.5.3 Mice deep cervical lymph node injection with Chinese ink.....	49
4.6 Specific objective 2c	50
4.6.1 MRI imaging of SPIONs and SPION-loaded exosomes through cervical and meningeal lymphatic vessels.....	50
4.7 Specific objective 3 and histological analysis of retrograde and anterograde flow through the cervical and meningeal lymphatic system.	52
4.7.1 Gold nanoparticles characterization	52
4.7.2 Normal brain anatomy of controls.....	53
4.7.3 Retrograde flow evaluation of gold nanoparticles <i>post-mortem</i>	54

4.7.4 Retrograde flow evaluation of Chinese ink <i>post-mortem</i>	56
4.7.5 Retrograde flow evaluation of Chinese ink <i>in vivo</i>	57
4.7.6 Retrograde flow evaluation of SPIONs and SPION-loaded exosomes <i>in vivo</i>	61
4.7.7 Immunohistochemistry evaluation of nanoparticles and the lymphatic marker LYVE-1 in the retrograde flow analysis.....	62
4.7.8 Anterograde flow evaluation of gold nanoparticles <i>post-mortem</i>	70
4.7.9 Anterograde flow evaluation of Chinese ink <i>post-mortem</i>	73
4.7.10 Anterograde flow evaluation of gold nanoparticles <i>in vivo</i>	74
4.7.11 Anterograde flow evaluation of Chinese ink <i>in vivo</i>	75
4.7.12 Anterograde flow evaluation of SPIONs and SPION-loaded exosomes <i>in vivo</i>	76
Chapter 5: Discussion	78
5.1 Reproducibility and repeatability on the connection between the meningeal and cervical lymphatic vessels.....	78
5.2 Bidirectional motion of SPIONs, SPION-loaded exosomes, Chinese ink, and gold nanoparticles through the cervical and meningeal lymphatic system	79
5.3 Future perspectives of the study	79
5.4 Conclusion	81
References.....	83
Supplementary Material	92
1. MicroCT analysis of the retrograde flow of gold nanoparticles from the cervical lymphatic vessels to the brain.	92
2. Transcriptome analysis on tumor sample.....	93
3. Immunohistochemistry of four positive lymphatic markers performed on the meningeal lymphatic tumor sample.	96
3.1 LYVE-1.....	96
3.2 PDPN.....	97
3.3 DSP	98
3.4 PROX1.....	99

List of Tables

Table 1. <i>In vitro</i> models that have evaluated the BBB hypothesis.....	5
Table 2. Uptake inhibition techniques used to evaluate endocytic pathways.	8
Table 3. Nanoparticle concentrations used for anterograde and retrograde flow evaluations.	31
Table 4. MicroBCA Quantitation of Total Protein	38
Table 5. DLS characterization of functionalized SPIONs	42
Supplementary Table 1. Transcriptome analysis of a meningeal lymphatic tumor (Genes associated with lymphatic system)	93
Most characteristic lymphatic markers.....	95

List of Figures

Figure 1. Uptake and transcytosis mechanisms for crossing of extracellular vesicles through the BBB.	10
Figure 2. Comparison of BBB structures of zebrafish, mice, and humans.....	15
Figure 3. Anatomical pathways and barriers of the CNS as potential routes for extracellular vesicles.	18
Figure 4. Evaluation of anterograde and retrograde flow of different nanoparticle solutions through the cervical and meningeal lymphatic system.	27
Figure 5. Iron oxide nanoparticles characterization.	33
Figure 6. MRI visualization of different percentages of SPION synthesized stocks.	35
Figure 7. T1(ms) weighted MRI map parameters.	36
Figure 8. MRI SPION analysis on chicken muscular tissue.	37
Figure 9. Characterization of B16F10 exosomes.....	39
Figure 10. Western blot analysis.....	40
Figure 11. SPION characterization.	41
Figure 12. STEM visualization and histogram of SPIONs.	42
Figure 13. Exosome + SPIONs characterization.	44
Figure 14. Cell viability at different nanoparticle concentrations.	44
Figure 15. Intracerebroventricular injection of Evans Blue dye.	45
Figure 16. Deep cervical lymph node injection of Evans Blue dye.	46
Figure 17. Characterization of Chinese ink.	48
Figure 18. Intracerebroventricular injection of Chinese ink.	48
Figure 19. Deep cervical lymph node injection of Chinese ink.	50
Figure 20. MRI analysis of the anterograde flow of SPIONs and SPION-labeled exosomes through the cervical and meningeal lymphatic system.	51
Figure 21. MRI analysis of the retrograde flow of SPIONs and SPION-labeled exosomes through the cervical and meningeal lymphatic system.	52
Figure 22. Gold nanoparticle characterization.	53
Figure 23. Normal mouse brain anatomy.	54
Figure 24. Retrograde flow of gold nanoparticles <i>post-mortem</i> using Gold Enhancement technique.	55
Figure 25. Retrograde flow of Chinese ink nanoparticles <i>post-mortem</i>	57
Figure 26. Retrograde flow of Chinese ink nanoparticles <i>in vivo</i>	60
Figure 27. Carotid artery and jugular vein of a mouse injected with Chinese ink nanoparticles at the deep cervical lymph node <i>in vivo</i>	60

Figure 28. Retrograde flow evaluation of SPIONs in vivo using Perls' Prussian Blue.	62
Figure 29. Gold nanoparticles and LYVE-1 immunohistochemistry.....	64
Figure 30. Gold nanoparticles and LYVE-1 immunohistochemistry.....	65
Figure 31. Chinese ink and LYVE-1 immunohistochemistry.....	66
Figure 32. Chinese ink and LYVE-1 immunohistochemistry.....	68
Figure 33. SPIONs and LYVE-1 immunohistochemistry.	69
Figure 34. Anterograde flow of gold nanoparticles <i>post-mortem</i> using Gold Enhancement technique.	70
Figure 35. Cephalic structures stained after injection into the cisterna magna of gold nanoparticles.....	72
Figure 36. Anterograde flow of Chinese ink in <i>post-mortem</i> evaluations.....	73
Figure 37. Cephalic structures stained after injection into the cisterna magna of Chinese ink. 74	
Figure 38. Anterograde flow evaluation of gold nanoparticles in vivo.....	74
Figure 39. Anterograde flow of Chinese ink in in vivo evaluations.....	76
Figure 40. Anterograde flow of SPIONs in in vivo evaluations.	77
Supplementary Figure 1. MicroCT scan analysis of the retrograde flow of gold nanoparticles from the cervical lymphatic vessels to the brain.	92
Supplementary Figure 2. Immunohistochemistry analysis for LYVE-1 on a meningeal lymphatic tumor sample.....	96
Supplementary Figure 3. Immunohistochemistry analysis for PDPN on a meningeal lymphatic tumor sample.....	97
Supplementary Figure 4. Immunohistochemistry analysis for DSP on a meningeal lymphatic tumor sample.....	98
Supplementary Figure 5. Immunohistochemistry analysis for PROX-1 on a meningeal lymphatic tumor sample.....	99

Abstract

Introduction: Exosomes are extracellular vesicles with a size of 50-150 nm that have been associated with the transportation of various biological contents and with intercellular communication. Given their role in metastasis, understanding exosome tissue distribution is critical to cancer pathophysiology. The exact routes and mechanisms of exosome distribution from peripheral organs to the central nervous system (CNS) remain unknown. A possible route is through the recently discovered brain lymphatic system, due to its connection with the deep cervical lymph nodes and its morphological characteristics.

Hypothesis: Metastatic cell-derived exosomes are transported from the deep cervical lymph nodes to the central nervous system through the meningeal lymphatic vessels.

Objective: To develop nanoparticle-loaded exosomes derived from a metastatic cell line and administer these exosomes via the cervical and meningeal lymphatic system to evaluate their arrival to the central nervous system.

Methodology: Superparamagnetic iron oxide nanoparticles (SPIONs) (mean size 8.3 ± 2.9 nm and Zeta potential 36.8 ± 5.44 mV) were prepared by chemical coprecipitation of ferric and ferrous chlorides. Exosomes (41.77 ± 1.64 nm and -10.8 ± 2.49 mV) were isolated from the melanoma B16F10 cell line through the Exo-Spin column protocol and loaded with SPIONs through electroporation. Gold nanorods (11.25 ± 0.57 nm and 45.4 ± 7.62 mV) were prepared and functionalized with polyethylene glycol. Chinese ink nanoparticles (61.62 ± 4.84 nm and -6.34 ± 0.63 mV) were also used. C57BL/6 mice were used to evaluate the anterograde and retrograde route of the lymphatic meningeal system with *post-mortem* and *in-vivo* procedures. All animal procedures were approved by the Ethical Animal Committee of our institution. Mice were anesthetized with isoflurane. To evaluate the anterograde nanoparticle flow we injected 10 μ L of each nanoparticle solution in the cisterna magna (3 animals per condition). To evaluate the retrograde nanoparticle flow we injected 10 μ l of each nanoparticle solution (SPIONs 3200 μ g/mL; exosomes + SPIONs 1.67×10^{11} particles/mL; gold nanorods 1.71×10^{14} particles/mL; Chinese ink 10%) in the deep cervical lymph node (3 animals per condition). The animals were euthanized after 30 min post injection. The head and neck were fixed with 4% paraformaldehyde for histological analysis and *post-mortem* MRI imaging.

Results: Anterograde pathway: Both SPIONs and SPION-loaded exosomes showed hypointense signals of cervical lymphatic structures after intracerebroventricular injections through the cisterna magna in the T2w and T2* MRI images. Gold Enhancement technique confirmed anterograde flow of both gold nanorods and Chinese ink nanoparticles by cervical lymphatic staining. Macroscopically, cisterna magna injections showed staining of deep cervical lymph nodes within the first minute after the administration of Evans Blue dye and Chinese ink. Retrograde pathway: Both SPIONs and SPION-loaded exosomes revealed hypointense signals in the brain ventricles and parenchyma in MRI T2w image and T2* map, after 30 min of deep cervical lymphatic injection. Gold Enhancement staining showed histological confirmation of the arrival of gold nanorods and Chinese ink nanoparticles to the brain parenchyma from the cervical injections. Macroscopically, deep cervical lymph node injections with Evans Blue and Chinese ink showed staining of the meninges and brain parenchyma. Nanoparticles colocalized with the stain of meningeal lymphatic vessels using anti-LYVE-1.

Discussion: The cervical and meningeal lymphatic system can transport nanoparticles not only in the classically described lymphatic drainage towards the thorax but can also serve as an access gate to the brain. This newly discovered mechanism for the meningeal lymphatic pathway could be exploited in the theranostic field of nanomedicine to deliver drugs for the treatment of various neurological diseases and the developing of diagnostic contrast media. The understanding of cancer exosome distribution through the cervical and meningeal lymphatic system will aid in a more profound comprehension of brain metastasis pathophysiology.

Chapter 1: Introduction

1.1 Exosomes and current hypotheses on their brain uptake

Extracellular vesicles (EVs) are particles delineated by a lipid bilayer that are naturally released from cells but cannot replicate (1). Although microvesicles, exosomes, and apoptotic bodies are usually regarded as the three main subtypes of EVs, classification varies upon biogenesis, release pathway, size, content, and function (2). Other nomenclature can be found in the literature based on whether they have an endosomal origin (exosomes) or are derived from the plasma membrane (ectosomes, microparticles, microvesicles) (1,3). Furthermore, the Minimal Information for Studies of Extracellular Vesicles 2018 (MISEV2018), has proposed the use of operational terms based on the physical characteristics of EVs, such as size (“small EVs” < 200nm and “medium/large EVs” > 200nm); their biochemical composition (CD63+/CD81+- EVs, Annexin A5-stained EVs, etc.); or descriptions of conditions or cell of origin (podocyte EVs, hypoxic EVs, large oncosomes, apoptotic bodies) (1). EVs show roles in diverse processes such as intercellular communication, transportation of biological contents, homeostasis, and cellular response to environmental changes on the parent and recipient cells (4–7).

Exosomes are extracellular vesicles with a size of 50-150 nm that have been associated with the transportation of various biological contents and with intercellular communication (8,9). Their cargos include nucleic acid material (RNA and DNA), non-coding RNAs (like miRNA), proteins (e.g. tetraspanins, heat shock proteins, Alix, TSG101, clathrin, MCH I and MCH II), sphingolipids (ceramide and cholesterol) and occasionally even viruses or their parts (10). The variety of molecules highlights the relevance of these vesicles in a myriad of processes that can influence homeostasis and cellular response to environmental changes.

Exosome biogenesis occurs as a normal cellular mechanism that takes advantage of the endocytic recycling pathway. Vesicles formed from endocytosis at the plasma membrane fuse to develop early endosomes. After maturation, intraluminal vesicles in late endosomes bud off into an intra-cytoplasmic lumen. These multivesicular bodies (MVB)

evade lysosomal fusion and fuse directly with the plasma membrane supported by the soluble NSF attachment protein receptor complex (SNARE) (10,11). Finally, they are released to the extracellular space and can reach cells in the local region or at distant tissues. Exosomes have been found in almost all fluids, including blood (~ 3,000,000 per microliter), plasma, cerebrospinal fluid, breast milk, bile, urine, saliva, amniotic and synovial fluid (12).

The relevance of EVs research in the past two decades has increased exponentially, as demonstrated by a 733-fold rise in publication output since the year 2000 (13). This is mainly due to their potential diagnostic and therapeutic applications in fields such as cancer, neurodegenerative, and immunological diseases (14–16). For example, a phase I study by Escudier et al. that used autologous Dendritic Cell-Derived EVs (DEX) loaded with Melanoma-associated antigen 3 (MAGE-3) as immunotherapy in metastatic melanoma patients showed no major toxicity, a partial response, and tumor regressions at skin and lymph node sites (17). Other phase I and phase II studies have confirmed these antitumor effects of DEX and MAGE-3 on advanced non-small cell lung cancer patients (18,19); ascites-derived EVs combined with granulocyte–macrophage colony-stimulating factor (GM-CSF) on colorectal cancer (20); tumor cell-derived EVs packed with methotrexate in lung cancer (21); and even plant-derived EVs loaded with curcumin in colon cancer (NCT01294072)(22). In Alzheimer Disease (AD), possible biomarkers with diagnostic relevance have been identified, such as elevated lysosome-associated membrane protein 1 (LAMP1) and cathepsin D levels in plasma EVs (23), and low levels of EV-associated miRNA-193b in cerebrospinal fluid (24,25). In immunology, EVs derived from mesenchymal stem cells and dendritic cells have shown positive results in reduction of inflammation and promotion of tissue regeneration in preclinical models of osteoarthritis, autoimmune uveitis, and Irritable Bowel Syndrome (26–29). Most recently, EVs research has also played a role in developing vaccines against COVID-19, by expressing the SARS-CoV-2 Spike protein on their surface or by delivering mRNAs of viral proteins (30).

Exosomes have also been linked with the promotion of cancer metastasis. Tumors increase the rate of exosome production and are associated with the preparation of the pre-metastatic niche. Gastric cancer exosomes carrying CD97 and Let-7, for example, have been shown to induce oncogenic activity previous to metastatic growth, particularly in lymphatic tissue (31,32). Cargos containing integrin, MET oncogenes, miRNA, hsp90

and annexin-II molecules promoting epithelial-mesenchymal transition (EMT) have been described to regulate and induce metastasis in otherwise normal cellular microenvironments (33–35). Besides inducing EMT, exosomes such as those of melanoma control degradation of the extracellular matrix (ECM) by metalloproteases (MMPs), activating integrins, epidermal growth factor and Notch receptors (36–38). Given the role in metastasis, understanding exosome tissue distribution is critical to cancer pathophysiology. In this regard, the brain is one of the most clinically relevant sites since overall survival after diagnosis is usually poor (39). In melanoma, early detection and surgical removal result in a five-year survival rate of 92% and a ten-year survival rate of 89% (40). However, if metastasized to the brain, the one-year survival rate falls to 32-62% (41). Autopsies have also revealed that 75% of deaths related to melanoma are associated with brain metastases (42). Nevertheless, the exact routes and mechanisms of exosome distribution from peripheral organs to the central nervous system (CNS) are still largely unknown.

Once they reach other cells, exosome content uptake seems to occur following different endocytic pathways, including clathrin-dependent endocytosis, and clathrin-independent pathways such as caveolin-mediated, macropinocytosis, phagocytosis, and lipid raft mediated internalization (43,44). The cargo has been described to control many cellular physiological responses such as immunity, coagulation, inflammation, and angiogenesis; and pathological responses as in cancer malignant transformation, viral replication, and neurodegeneration (9,12,45).

However, as highlighted by Margolis et al., many concepts remain obscure with untested hypotheses and speculations awaiting experimental proofs (46); including implications of size diversity, biogenesis pathways, and surface characteristics on biological effects, targeting, and cell physiology (46). One of the most outstanding unsolved issues to date regarding EVs lies in their ability to reach the brain, seemingly crossing biological barriers in a bidirectional manner to influence either neurons or peripheral tissues. A more detailed comprehension on this phenomenon becomes particularly important when considering the potential for the use of EVs as vehicles in pharmacology and therapeutics. In the last 10 years advances have been made in the evaluation of the therapeutic effects of EVs in pre-clinical models of brain diseases such as AD, stroke, traumatic brain injury, and intracerebral hemorrhage (47). Unfortunately, there is still inconsistency in the scarce literature available that evaluates the mechanisms for exosomes reaching the brain.

1.2 The blood brain barrier pathway hypothesis

There is evidence that exosomes can somehow surpass the Blood-Brain Barrier (BBB). Nevertheless, whether exosomes are directly crossing the BBB or using alternate pathways is yet to be clarified.

1.2.1 *In vitro* models

In vitro models that have evaluated this route are summarized in Table 1. Different versions of the Boyden Chamber assay have been applied to assess migration of EVs through a BBB model. Nevertheless, simulation of the BBB layer has differed substantially among experiments, most evaluating monolayer models derived from different species.

Morad *et al.* used the human brain-seeking MDA-MB-231 breast cancer cell line that derives from a metastatic pleural effusion site (48). This group was able to detect EVs crossing to the abluminal side of the monolayer transwell. Tominaga *et al.* also utilized breast cancer lines MDA-MB-231-luc-D3H1 and MDA-MB-231-luc-D3H2LN, and generated a subset of brain metastatic derivative populations (BMD2a and BMD2b) (49). However, they were able to detect EVs in endothelial cells but not pericytes of a bilayer transwell, or in astrocytes in the abluminal side of the assay. This highlights the importance of the number of layers used for BBB models, as described previously, even when using similar cells of origin for EVs.

Chen *et al.* analyzed EVs from a different cell line, the human HEK 293T cells of the embryonic kidney epithelium (50). Even though they employed a monolayer as Morad *et al.*, EVs from these experiments were unable to significantly cross the BBB unless an inflamed environment was simulated with TNF- α treatment (up to approximately 10% of exosomes crossed from the luminal to abluminal chamber after 18 hours) (50). Matsumoto *et al.* isolated EVs from human red blood cells (RBC) instead, both from Parkinson's disease and healthy control patients (51). Consistent with Chen *et al.*, they showed that despite being largely impermeable to RBC-EVs under healthy conditions, the BBB monolayer model allowed increased crossing of EVs after administration of lipopolysaccharide (LPS) to mimic inflammation (51). Finally, although not a transwell,

Kuroda *et al.* evaluated successful incorporation, but not crossing, of the melanoma cell line SK-Mel-28 PKH67-labeled EVs into human blood–brain barrier endothelial hCMEC/D3 cells after incubation at 37 °C (52).

Table 1. *In vitro* models that have evaluated the BBB hypothesis

Author	Model	Result
Morad <i>et al.</i>	Transwell Monolayer	EVs crossed monolayer
Tominaga <i>et al.</i>	Transwell Bilayer	Detected in endothelium but not pericytes or astrocytes
Chen <i>et al.</i>	Transwell Monolayer	Crossed only with TNF- α treatment
Matsumoto <i>et al.</i>	Transwell Monolayer	Crossed only with LPS treatment
Kuroda <i>et al.</i>	Incorporation of melanoma cell line SK-Mel-28 PKH67-labeled EVs into human BBB endothelial hCMEC/D3	Successful incorporation but not crossing of the endothelium

EVs extracellular vesicles, TNF- α tumor necrosis factor alpha, LPS lipopolysaccharide

Results from transwell experiments differ considerably depending on the EV cell of origin and the cell layers in the assay construction. Those originating from breast cancer showed internalization in endothelial cells, pericytes, and astrocytes independently, but could not cross beyond the endothelium when faced with more than one layer (49). Studies using EVs derived from the HEK 293T cell line and human erythrocytes demonstrated crossing of a BBB monolayer only when associated with inflammation (50,51).

The increase in EVs permeability under inflammatory conditions appear to favor an active transcellular transport rather than passive paracellular diffusion (50,51). Matsumoto *et al.* showed an LPS dose-dependent decrease in TEER, that reached a reduction of approximately 75% at 100 ng/mL (51). The permeability of EVs increased almost 300% relative to vehicle controls after treatment with an LPS dose of 100 ng/mL (51).

Pharmacokinetic studies in mice showed that the unidirectional influx constant (K_i) of RBC-EVs was not significantly different compared to albumin in normal conditions (51). However, under LPS treatment, the K_i of mice was significantly higher for RBC-EVs compared to the much smaller albumin molecule, which suggests that RBC-EVs cross the BBB more easily (LPS; $0.5533 \pm 0.1704 \mu\text{L/g-min}$ vs control; $0.1079 \pm 0.05487 \mu\text{L/g-min}$, $p = 0.0199$) (51).

Results with TNF- α treatment from Chen *et al.* support the idea of an active transcellular transport mechanism of EVs in inflammatory conditions (50). Most interestingly, no significant differences in bioluminescence activity were observed for paraformaldehyde-fixed BMECs under both TNF- α activated and untreated conditions at all time points, unlike the much greater exosome crossing of the living BMECs under TNF- α (up to approximately 10% of EVs) compared to untreated condition (50). Immunofluorescence of VE-cadherin, ZO-1, and Claudin-5 showed that their expression levels were significantly down-regulated after TNF- α treatment, which also plays a role in the altered intercellular permeability of BMECs (50).

BMEC monolayer experiments have resulted in essential descriptions on potential interactions of EVs with the endothelial component of the BBB. Still, the mechanisms proposed for these vesicles to reach the brain parenchyma could be insufficient to establish the whole process clearly. The BBB is also supported by mural cells comprising of vascular smooth muscle cells and pericytes, as well as glial astrocytic cells that contribute to the regulation of components that ultimately reach neurons (53). These have rarely been considered in BBB transwell experiments evaluating EVs. Tominaga *et al.* is the only group that has considered using a BBB kit made of primary cultures of monkey *Macaca irus* brain capillary endothelial cells with an added Wistar rat pericyte layer before reaching Wistar rat astrocytes at the base of the well (54). Still, astrocyte crossing was not addressed.

1.2.2 Evaluation of uptake and transcytosis

Uptake refers to the internalization pathways of particles through the cell membrane that usually occur through pinocytosis, which can be subcategorized into clathrin-mediated endocytosis, caveolae-mediated endocytosis, clathrin- and caveolae-independent endocytosis and micropinocytosis (Figure 1) (55). Following uptake, intracellular trafficking of particles, including EVs, will determine their destination within cellular

compartments (55). Some will encounter degradation after integrating with lysosomes (55). However, some will escape this pathway with the possibility of cellular release (Figure 1) (55).

Transcytosis is the transport of macromolecular cargo from one side of a cell to the other within a membrane-bounded carrier(s) (Figure 1) (56). Transport pathways of substances across the BBB include paracellular diffusion, transcellular diffusion, protein-mediated transport (such as GLUT-1, CNT2, and MCT1), receptor-mediated transcytosis, and adsorptive-mediated transcytosis (57,58). From these mechanisms, active transcytosis has been suggested as the most likely in EVs crossing of the BBB (57). Studies by Chen *et al.* and Morad *et al.* have shed light on specific processes that might be involved. Both identified a significant reduction of EVs internalization or crossing through brain endothelial cells at 4°C, indicating that an active mechanism should be responsible for transport. Morad *et al.* further treated with Dynasore, an inhibitor of endocytosis, decreasing the rate of EVs detected in abluminal chambers of transwell analyses (48).

Using uptake inhibition techniques associated with measurements by flow cytometry from cultured BMECs in 12-well plates exposed to labeled EVs, as well as assays evaluating colocalization of EVs to specific proteins, several endocytic pathways have been examined (Table 2 and Figure 1): macropinocytosis, clathrin-dependent endocytosis, and lipid raft/caveolae-dependent endocytosis (48,50).

Table 2. Uptake inhibition techniques used to evaluate endocytic pathways.

Mechanism	Author	Cells and EVs	Inhibitor (concentration)	Pre-treatment duration	Incubation with EVs	Uptake of Evs
Macropinocytosis	Morad <i>et al.</i>	BMECs + TdTom-Br-EVs	EIPA (100 μ M); cytochalasin D (500 nM)	30 min	3 h	Decreased
	Chen <i>et al.</i>	BMECs + PKH26-labeled exosomes	EIPA (1mM); cytochalasin D (20 μ M)	30 min	1 h	Decreased
Clathrin-dependent endocytosis	Morad <i>et al.</i>	BMECs + TdTom-Br-EVs	Chlorpromazine (20 μ M); ML141 (100 μ M)	30 min	3 h	Decreased
	Chen <i>et al.</i>	BMECs + PKH26-labeled exosomes	Chlorpromazine (15 μ M)	30 min	1 h	Decreased
Lipid raft/caveolae-dependent endocytosis	Morad <i>et al.</i>	BMECs + TdTom-Br-EVs	Filipin III (10 μ M)	30 min	3 h	No effect
	Chen <i>et al.</i>	BMECs + PKH26-labeled exosomes	Filipin III (5 μ M); M β CD (5 mM); nystatin (5 μ M)	30 min	1 h	Decreased

EIPA: 5-(*N*-ethyl- *N*-isopropyl) amiloride; M β CD: methyl- β -cyclodextrin.

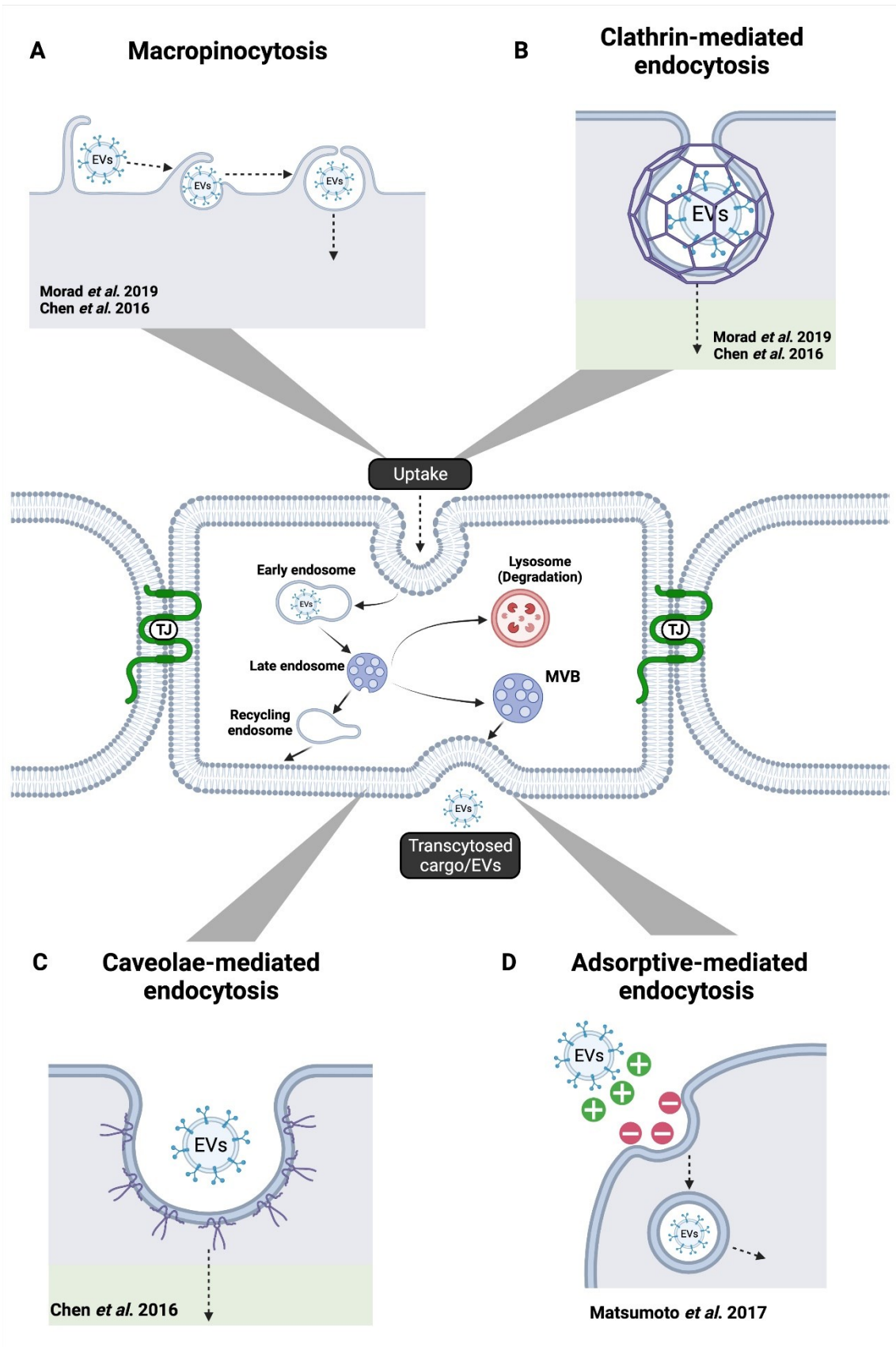


Figure 1. Uptake and transcytosis mechanisms for crossing of extracellular vesicles through the BBB. The figure shows four uptake mechanisms that have been evaluated and proposed for the active transport of EVs across the BBB and the authors that have described evidence to support them: (A) Macropinocytosis (48,50). (B) Clathrin-mediated endocytosis (48,50). (C) Caveolae-mediated endocytosis (50). (D) Adsorptive-mediated endocytosis (51). The fate of EVs after internalization include recycling to the plasma membrane, degradation of EVs by lysosomes, and final transcytosis of EVs and their cargos to the extracellular space. EVs: extracellular vesicles; BBB: blood brain barrier; MVB: multivesicular body; TJ: tight junctions

Morad *et al.* used 5-(*N*-ethyl- *N*-isopropyl) amiloride (EIPA) and cytochalasin D to block macropinocytosis, which decreased the uptake of EVs significantly (approximately a 50% and 75% reduction relative to control, respectively) (48). This was supported by TdTom-EVs partially colocalizing with 70 kDa dextran, a marker for macropinocytosis, under fluorescence microscopy images (48). Similarly, Chen *et al.* treated with the same inhibitors and their results concurred under TNF- α inflammatory conditions after 18h incubation (approximately an 80% and 45% reduction relative to control, for EIPA and cytochalasin D respectively). Inhibition was assessed by EVs uptake assay using confocal microscopy and image analysis (50).

Clathrin-dependent endocytosis was inhibited by chlorpromazine and a Cdc42/Rac1 GTPase inhibitor, ML141, in Morad *et al.* studies (48). These were able to decrease EVs uptake significantly (approximately a 40% and 60% reduction relative to control, for chlorpromazine and ML141 respectively). TdTom-EVs also colocalized with Alexa647 transferrin, a marker of this pathway. In agreement with these findings, Chen *et al.* evidenced an attenuation of EVs uptake when blocking with chlorpromazine alone (approximately a 55% reduction in the native condition and a 71% reduction in the TNF- α condition, relative to control) (50).

However, the two groups differ on their results for lipid raft/caveolae-dependent endocytosis experiments. Morad *et al.* could not identify a role of this route, as inhibition by filipin showed no effect on EVs uptake in endothelial cells by flow cytometry (48). There was also a lack of colocalization of EVs with caveolin. In contrast, Chen *et al.* pre-incubated BMECs with cholera toxin B (CtxB), a late endosomal compartment marker, and found a decrease of PKH67-labeled exosomes uptake by BMECs after treatment with filipin III (approximately a 27% reduction in the native condition and a 64% in the TNF- α condition, relative to control) (50). They observed the same results with two additional inhibitors: methyl- β -cyclodextrin (approximately a 51% reduction in the native condition and a 61% reduction in the TNF- α condition, relative to control) and nystatin

(approximately a 37% reduction in the native condition and a 46% reduction in the TNF- α condition, relative to control) (50). Therefore, the authors concluded that caveolae-dependent endocytosis is one likely route of EV internalization (50).

Other positive colocalization results by Morad *et al.* included Rab11 (a marker of recycling endosomes), BODIPY conjugated DQ-ovoalbumin (a marker of endolysosomal structures), VAMP-3 (marker of exocytosis and recycling), VAMP-7 (marker of lysosome fusion), and SNAP23/Syntaxin 4 (complex on the basolateral membrane) (48). These indicate that EVs fate after internalization can include recycling, transcytosis, or degradation. Chen *et al.* did not evaluate these parameters.

Antibody and knockdown strategies have also been used to test for the influence of surface receptors of BBB endothelial cells on exosome uptake. Kuroda *et al.* utilized anti-integrin $\alpha 5$ and anti-integrin αV antibodies, which were able to reduce the uptake by 11.8% (52). Interestingly, CD46 small interfering RNA (siRNA) transfection into hCMEC/D3 endothelial cells also revealed a 39.0% decrease of exosome uptake (52).

Transcytosis might be the primary active mechanism for EVs crossing the healthy BBB (57). There is evidence that macropinocytosis and clathrin-dependent endocytosis have a role even in EVs originating from different cell types (48,50). However, lipid raft/caveolae-dependent endocytosis shows inconsistent data depending on the technique used and EVs' originating cell line. As only two groups have examined this specific problem, differences in the data could also be model dependent.

Given the intracellular processes that involve uptake and transcytosis, without live-imaging and proper tracing, it is difficult to determine whether the same EVs from the discussed assays permeate across the BBB. It cannot be excluded that the contents from the internalized EVs are released from the original lipid bilayer, repacked in structures such as multivesicular bodies (MVB), and again released as EVs. In addition, the mere identification of a dye or fluorescent marker on the opposite side of a transwell assay does not guarantee its association to the lipid bilayer of an EV.

1.2.3 *In vivo* evaluations of the BBB hypothesis for EVs

Human and mouse models

The following section will describe evidence in mouse models and human research participants that indicates EVs can somehow move in a bidirectional manner through the BBB. However, there is only indirect data to suggest the mechanisms of transcytosis. Alzheimer's studies in humans, for instance, have revealed that exosomes with Central Nervous System (CNS) components can be detected in the peripheral blood and have emerged as potential biomarkers (59–63). Morad *et al.* performed retro-orbital injections of TdTom-Br-EVs isolated from brain-seeking MDA-MB-231 breast cancer cells and evaluated the distribution of EVs to the brain in nude mice (48). Histological analyses showed that Br-EVs were taken up by glial fibrillary acidic protein (GFAP)+ astrocytes. Shi *et al.* were able to detect exosomes carrying CNS α -syn in blood, which is correlated with Parkinson's disease, by an immunoaffinity capturing protocol that isolates L1 cell adhesion molecule (L1CAM)-containing exosomes in human or mouse plasma (64). However, it is worth mentioning that a recent report by Norman *et al.* has recommended against the use of L1CAM as a marker in neuron-derived EVs isolation protocols as they demonstrated no association between L1CAM with EVs in human cerebrospinal fluid or plasma (65). Nonetheless, Shi *et al.* discuss that exosomes possibly cross multiple layers of the BBB by jumping from cell-to-cell via the MVB compartment, citing a theory by Record *et al.* that relates exosomes to processes observed in HIV, but do not test the hypothesis experimentally in their model (64,66–68).

Adsorptive mediated transcytosis (AMT) was proposed by Matsumoto *et al.* after analyzing the co-injection of unlabeled RBC-EVs and labeled ^{125}I -RBC-EVs in CD1-mice (51). As increasing doses of unlabeled EVs did not affect LPS-induced entry of labeled EVs, they concluded that probably the transfer mechanism does not occur via a saturable process (51). The authors further examined the influence of wheat germ agglutinin (WGA), a potent AMT inducer, which increased brain uptake of ^{125}I -RBC-EVs relative to controls (51). Nevertheless, RBC-EVs were found to colocalize with antibodies against Iba-1-labeled microglia, but not GFAP-labeled astrocytes or MAP2-labeled neurons (51).

Another method that has been utilized to evaluate the EVs transport from the brain to peripheral blood, and therefore indirectly proving crossing of the BBB, is orthotopic

xenotransplantation in mice of human tumor cells (69). García-Romero *et al.* were able to isolate human gDNA from EVs originated from glioblastoma-cancer stem cells (GBM27 and GBM38), circulating in the bloodstream after transplantation. However, they did not address possible mechanisms of transcytosis at the level of the BBB (69). The mouse model of Tominaga *et al.* did not analyze transcytosis *in vivo* either but showed promotion of cancer cell metastasis by EVs through the destruction of the BBB by miR-181c and its target gene downregulation, PDPK1 (49). This could also play a role in the crossing of EVs populations in cancer.

Banks *et al.* surveyed EVs from 10 different sources, including six cancer and four non-cancerous cell lines in CD-1 mice (70). These included EVs from mice macrophages (J774A.1), fibroblasts (NIH-3T3), and oral squamous cells (SCCVII), as well as human T cells (primary T cell), keratinocytes (HaCaT), melanoma (MEL526), breast (MDA-MB-231), head and neck cancer cells (PCI-30 and SCC-90), and leukemia (Kasumi) (70). They used the capillary depletion and the intracerebroventricular injection methods to determine, through radioactive 0.5mCi ¹²⁵I labeling of EVs, the degree to which EVs crossed the BBB from the peripheral blood compartment or the brain-to-blood efflux rate, respectively (70).

All EVs tested in Banks *et al.* analyses were reported to cross the BBB with different influx rates (70). Neither species nor cancer state seemed to influence the uptake (70). For additional characterization, LPS, WGA, and mannose 6-phosphate (M6P) impact on uptake were measured (70). LPS increased uptake of six human EVs populations and decreased uptake from one murine type (70). AMT uptake appeared to increase in half of the EV types (J774A.1, NIH-3T3, HaCAT, SCC-90, Kasumi) exposed to WGA (70). In contrast, M6P blocked uptake of fibroblast EVs, exhibiting dependence on the mannose 6-phosphate receptor for transport of this type of EVs (70). Despite this relevant description of EVs crossing compartments, no direct visualization of transcytosis through the BBB was executed.

Zebrafish model

To date, there is only one study that evaluates *in vivo* crossing of EVs through a direct study of the BBB. Morad *et al.* developed a Tg(kdrl:GFP) zebrafish model from embryos incubated in E3 medium at 28.5 °C (48). Experiments were performed 6-7 days postfertilization, when an intracardiac injection of TdTom-Br-EVs (5 nL of a 400 µg/mL

suspension per injection) was done using the Narishige Injection System (48). One hour postinjection, live imaging of embryos was conducted using a Nikon Eclipse Ti inverted microscope with a Yokogawa spinning disk scan head and an Andor iXon EM-CCD camera (48). Integrity of the BBB was verified by intracardiac injections of unlabeled Br-EVs (60 $\mu\text{g}/\text{mL}$), 10 kDa dextran-Alexa Fluor 647, and 70 kDa rhodamine B-dextran (60 $\mu\text{g}/\text{mL}$) (48).

This group was able to detect Br-EVs in the brain parenchyma at the time of imaging and time-lapse showed movement of EV-containing endocytic vesicles within endothelial cells (48). Some vesicles were able to reach the plasma membrane and fuse with it. The integrity of the BBB was preserved against 10 kDa and 70 kDa dextran (48). Together, this evidence demonstrated crossing of EVs through the BBB in a process suggestive of transcytosis.

The zebrafish has been described as a suitable model for BBB studies (71,72). However, there are several factors that need to be considered before drawing conclusions on mammals based on this model (Figure 2). Endothelial cells at the BBB are indeed comparable as demonstrated by conserved genetic expression of tight junction molecules such as ZO-1 and Cldn5, as well as the glucose transporter Glut1, the efflux pump Pgp, and the transcytosis inhibitor Mfsd2a (71,73–75). Nevertheless, zebrafish pericytes do not express canonical mammalian markers such as Rgs5a, Desmin a/b, or Cspg4, and originate from both neural crest and mesenchyme, rather than just from neural crest as in mice and humans (76–85).

Another critical difference between mammalian and zebrafish BBB is the astrocyte component (Figure 2). Zebrafish do not possess classic stellate astrocytes (76). Instead, they express radial glia lacking polarization of Aqp4, with processes that rarely become in contact with the vasculature (71,76,86). This could contribute to an impaired BBB function compared to mammals. Zebrafish is considered a more ancestral endothelial BBB with a less complex neurovascular unit (76). Therefore, more studies are still needed to determine if EVs can surpass the BBB in mammals *in vivo* as they do in zebrafish.

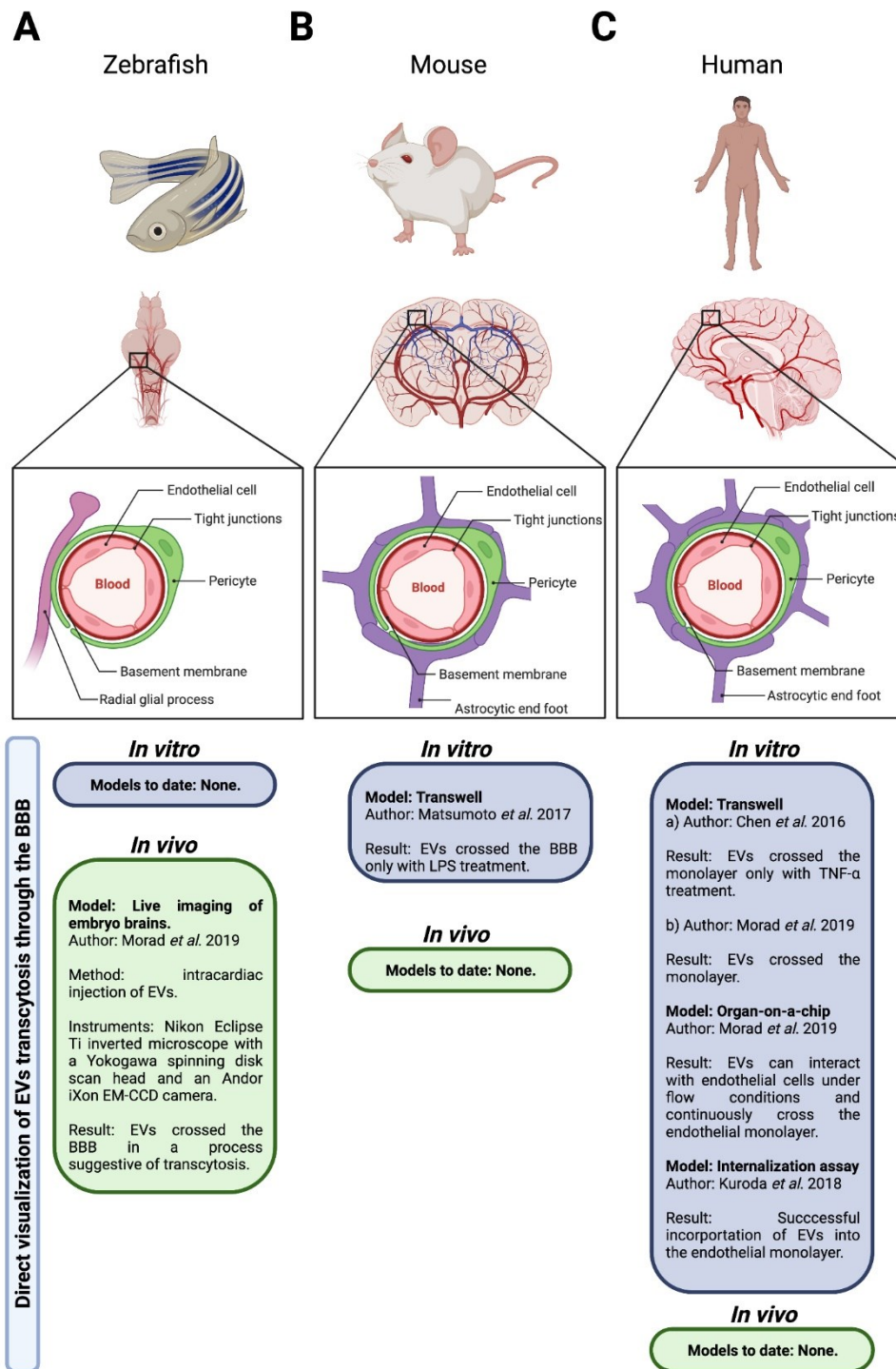


Figure 2. Comparison of BBB structures of zebrafish, mice, and humans. The figure shows the main components of the BBB, including endothelial cells with specialized tight junctions, pericytes, and astrocytic or glial processes. (A) The zebrafish BBB has a less complex neurovascular unit that lacks classic stellate astrocytes, with radial glial processes that rarely become in contact with the vasculature. (B) The mouse BBB presents astrocytic end feet in close contact with the vasculature. (C) Compared to mice, the human BBB shows a greater number of astrocytic end feet. Also shown are the *in vitro* and *in vivo* models that have evaluated direct visualization of EVs transcytosis through the BBB in these species. EVs: extracellular vesicles; BBB: blood brain barrier; EM-CCD: electron multiplication charge-coupled device; TNF- α : tumor necrosis factor alpha; LPS: lipopolysaccharide.

1.3 The choroid plexus hypothesis

Evidence has emerged on the role of exosomes in the transport of micronutrients, such as 5-methyltetrahydrofolate (5MTHF), through the blood-cerebrospinal fluid barrier at the choroid plexus (Figure 3) (87). Grapp *et al.* injected exosomes derived from folate receptor α (FR α)-transfected Z310 cells (an immortalized rat choroid plexus cell line) into the lateral ventricle of C57BL/6 mice (87). By labeling exosomes using the PKH26 dye and through immunohistochemistry analysis, they were able to show that exosomes penetrated the brain parenchyma and colocalized with GFAP-positive astrocytes as well as NeuN-positive neurons (87). They suggest a clathrin-independent pathway through glycosylphosphatidylinositol-anchored protein-enriched endosomal compartments that promote FR α translocation to multivesicular bodies before being released as exosomes (87). This pathway at the choroid plexus should be further examined as an EVs transportation site to the CNS.

1.4 The lymphatic pathway

This thesis will present the findings of the potential bidirectional motion of EVs from brain and peripheral tissues through the recently discovered meningeal lymphatic vessels. Until recently, the CNS was considered to have immune privilege, lacking a lymphatic drainage system despite several previous reports by Schwalbe (1869), Brierley and Field (1948), and Csanda and Földi (1960s) that were longed disregarded (88). However, Louveau *et al.* (2015) provided definite evidence of their existence, with a detailed description of their anatomical and histological characteristics, both in the C57BL/6 mouse and humans (89).

Brain lymphatics of about 20 to 30 μ m in diameter were discovered in the meningeal spaces parallel to the dural sinuses of rodents, expressing all the molecular hallmarks of lymphatic endothelial cells (Figure 3) (89–91). These included positive immunostaining for LYVE-1, podoplanin, and VEGFR3 (89). They exhibit initial type afferent lymphatic vessel features, with the absence of surrounding smooth muscle and valves (89). The system allows for the carrying of both fluid and immune cells from the cerebrospinal fluid (CSF) and is connected to the deep cervical lymph nodes (89). Ha *et al.* recently described a protocol to visualize and map dural lymphatic vessels *in vivo* through magnetic resonance imaging (MRI) by administering gadolinium-based contrast agents

(gadofosveset and gadobutrol) in human and nonhuman primates (92). These findings were also confirmed in humans, with vessel sizes varying from 7 to 842 μ m (93).

Their connection with the deep cervical lymph nodes and their contribution to immune cell transport opens the possibility of a new and yet unexplored route for EVs to reach and leave the CNS. Given their initial type characteristics, the meningeal lymphatic pathway might represent a less stringent barrier for EVs crossing compared to the classical BBB associated to blood vessels. Anatomical and molecular evidence that supports the notion that this is a more permissive route include the punctate expression pattern of Claudin-5 and VE-cadherin, the lack of integrin- α 9 expression typical of lymphatic valves, and the expression of a non-continuous basement membrane (89).

Demonstrating and understanding exosome distribution through this CNS lymphatic system could also aid in the development of better drug therapies based on these extracellular vesicles, the creation of better and more precise diagnostic and surveillance mechanisms for early tumor discovery, and a more profound comprehension of metastasis pathophysiology. This thesis will describe the preparation of exosomes loaded with superparamagnetic iron oxide nanoparticles (SPIONs) for MRI analysis to evaluate the bidirectional motion through the cervical and meningeal lymphatic system of the mouse. We will also show the results of experiments using gold nanoparticles, Chinese ink nanoparticles, and SPIONs as we explore further projections of a newly discovered mechanism to access the brain from peripheral tissues.

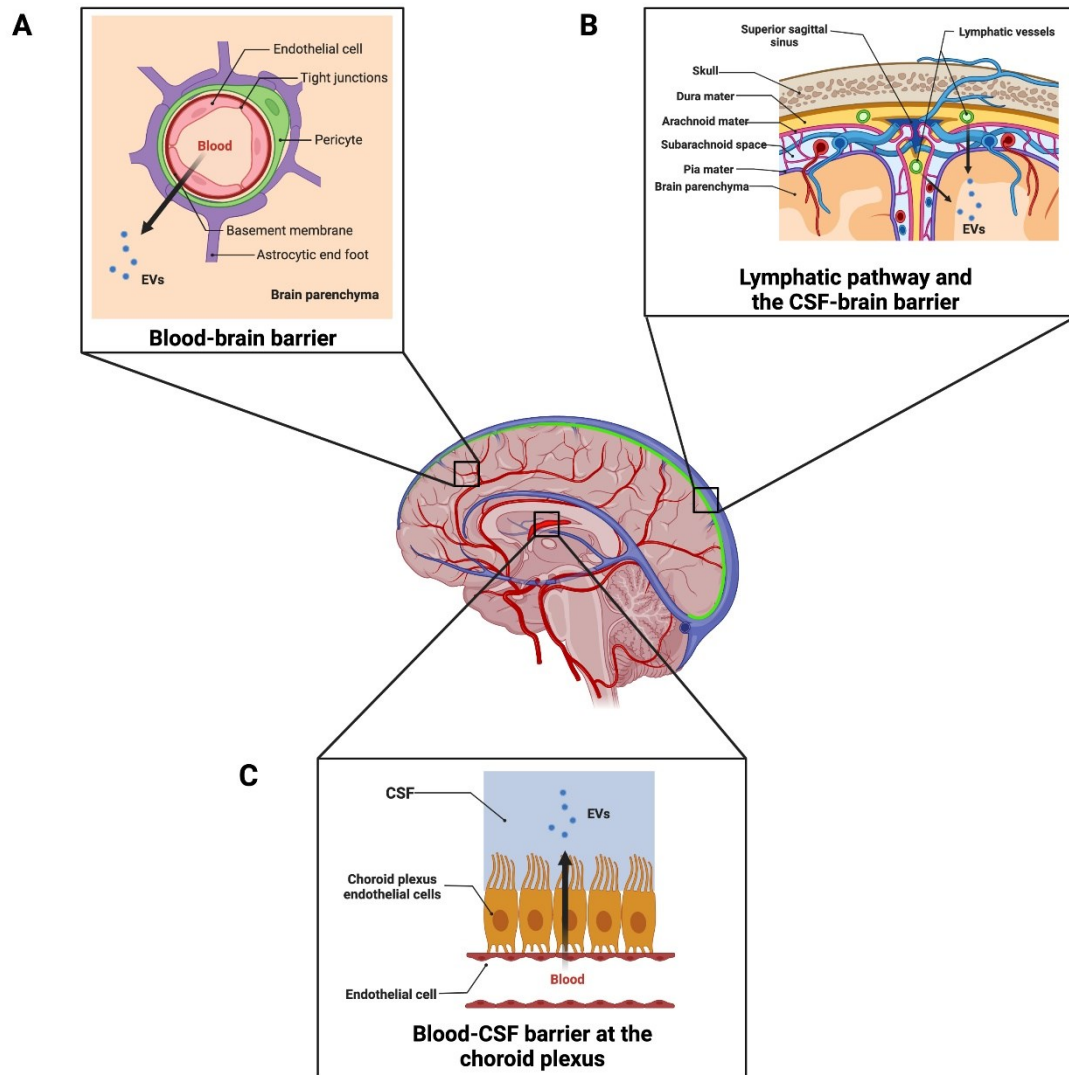


Figure 3. Anatomical pathways and barriers of the CNS as potential routes for extracellular vesicles. The figure shows theoretical vascular points of entrance for EVs and checkpoint barriers to the brain parenchyma that should be further examined. (A) The classical path that has been evaluated for EVs crossing from peripheral blood to the brain is through arterial flow and the BBB, comprised of endothelial cells, pericytes, and astrocytes (48,50–52). (B) The recently discovered meningeal lymphatic vessels expose a route to the CSF-brain barrier not yet explored and that EVs could exploit to access the brain parenchyma (89). (C) A third entrance point is through the Blood-CSF barrier at the choroid plexus (87). EVs: extracellular vesicles; BBB: blood brain barrier; CNS: Central Nervous System; CSF: cerebrospinal fluid

Chapter 2: Hypothesis and Objectives

Hypothesis

Metastatic cell-derived exosomes are transported from the deep cervical lymph nodes to the central nervous system through the meningeal lymphatic vessels.

General Objective

To develop nanoparticle-loaded exosomes derived from a metastatic cell line and administer these exosomes via the cervical and meningeal lymphatic system to evaluate their arrival to the central nervous system.

Specific objective 1: To prepare nanoparticle-loaded exosomes:

- a) To synthesize iron nanoparticles and stabilize them with polyethylene glycol, polyvinylpyrrolidone, or citrate to optimize incorporation into cells and exosomes.
- b) To prepare B16F10-derived exosomes loaded with iron nanoparticles.
- c) To evaluate the cell viability of SH-SY5Y cells exposed to nanoparticles and loaded exosomes.

Specific objective 2: To administer nanoparticle-loaded exosomes in mice via the lymphatic system, employing magnetic resonance imaging for their evaluation on the cervical and central nervous system tissues.

- Stage I: intracerebroventricular injection (into cisterna magna) of Evans Blue and Chinese Ink.

- Stage II: injection of Evans Blue and Chinese ink in the deep cervical lymph nodes.

- Stage III: MRI imaging of SPION-loaded exosomes through cervical and meningeal lymphatic vessels.

Specific objective 3: To validate through histological analysis the presence of nanoparticle-loaded exosomes in the meningeal lymphatic vessels.

Chapter 3: Methods

3.1 For specific objective 1a: To synthesize iron nanoparticles and stabilize them with polyethylene glycol, polyvinylpyrrolidone, or citrate to optimize incorporation into cells and exosomes.

3.1.1 Iron oxide nanoparticle synthesis

Samples of iron oxide nanoparticles were prepared by a chemical coprecipitation process from $\text{FeCl}_3 \cdot 6\text{H}_2\text{O}$ (432 mg), and $\text{FeCl}_2 \cdot 4\text{H}_2\text{O}$ (159mg). Ferric and ferrous chlorides were dissolved in 19mL of Milli-Q water with vigorous magnetic agitation at room temperature. One mL of ammonium (25%) was added to the solution with vigorous magnetic agitation for 10 min. After the previous mixture, three washes with Milli-Q water were performed, maintaining iron-nanoparticles in an 80 mL beaker with a neodymium magnet. Then, the superparamagnetic iron oxide nanoparticles (SPIONs) were washed twice with nitric acid. Finally, iron-nanoparticles were dissolved in Milli-Q water for later characterization. Two synthesis procedures were performed with an additional 90 min centrifugation at 13200 rpm followed by supernatant removal and dissolution of the precipitate in Milli-Q water.

For the stabilization of the synthesized particles, a volume of 0.5 mL of 0.5M sodium citrate was mixed with 4.5 mL of iron-nanoparticle solution, followed by 1.5h of magnetic agitation. 0.6 mL of sodium hydroxide was added to increase pH. Citrate-stabilized SPIONs were then washed once with Milli-Q water and diluted in 50 mL volume of Milli-Q water.

For particle functionalization, polyethylene glycol (PEG) in amino and carboxylic forms, polyvinylpyrrolidone (PVP), and alginate were tested. Once stabilized and functionalized SPIONs were prepared as previously described, 1 mL of the iron oxide nanoparticle solution was dissolved in 4 mL of Milli-Q water. Separate tubes with 1 mL of Milli-Q water and 1 mg of each compound were prepared. From the tubes, 500 μL were drawn into a container and mixed with 5 mL of the original SPION solution.

SPION synthesis and functionalization was done at the Department of Chemistry, Pharmacology and Toxicology of the Universidad de Chile in Dr. Marcelo Kogan's laboratory.

3.1.2 Characterization of iron oxide nanoparticles

The morphology and particle size of SPIONs was investigated by transmission electron microscopy (STEM, FEI Quanta 250) operating at 10.00 kV. Dynamic light scattering system for nanoparticle analysis (DLS) was used for size determination. The superficial charge was measured by a Zeta Potential Analyzer. SPIONs concentrations obtained from the synthesis were measured using Nanoparticle Tracking Analysis (NTA) by NanoSight. pH of the solutions was determined by pH meter. The concentration of iron nanoparticles in solutions was determined by inductively coupled plasma mass spectrometry (ICP MS). Characterization of nanoparticles was done at the Department of Chemistry, Pharmacology and Toxicology of the Universidad de Chile in Dr. Marcelo Kogan's laboratory.

3.2 For specific objective 1b: To prepare B16F10 derived exosomes loaded with iron nanoparticles.

3.2.1 Exosome purification

The B16F10 cell line was cultured using Exo-free medium and the isolated supernatant was centrifuged twice: first at 300g for 10 min at 4 °C and then at 16000g for 20 min at 4 °C. Filtration followed through 0.2 µm pore size filters. For purification, an Exo-spin (CELL GS) protocol was conducted, as ultracentrifugation was not available. Extracellular vesicles were first concentrated using a 10 kDa filter to separate larger cellular structures and then diluted in filtered PBS (0.1 µm pore size). The samples were then precipitated using Exo-spin Buffer overnight and then centrifuged for 1 hour at 16000g. The obtained pellet with exosomes was resuspended in 100 µL of PBS. Exo-spin columns were prepared with two consecutive washes with 250 µL of PBS at 50g for 10 sec. Finally, diluted exosomes were passed through the column using 200 µL of PBS and collected in microcentrifuge tubes.

3.2.2 Nanoparticle internalization to exosomes

Suspended exosomes, purified as previously described, were electroporated in 4 mm path length electroporation cuvettes. A single pulse was applied to each exosome sample under the high voltage setting and at an electric field of 0.75 kV/cm. Following electroporation, nanoparticle-loaded exosomes were reisolated using the Exo-spin protocol. This technique was done at the Department of Chemistry, Pharmacology and Toxicology of the Universidad de Chile in Sergio Alvarez's laboratory.

3.2.3 Characterization of exosomes

Exosomes were characterized by protein concentration (microBCA assay), shape by transmission electron microscopy (STEM, FEI Quanta 250), concentration and size with NanoSight. Western blot analysis was performed to determine the presence of exosome markers EEA1 and TSG101. Cell extracts and exosomes were lysed at 4°C in lysis buffer (50 mM Tris-HCl pH 7.4, 150 mM NaCl, 1 mM EDTA, 1% Triton X-100) supplemented with a cocktail of protease inhibitors [416 µM 4-(2-Aminoethyl)benzenesulfonyl fluoride, 0.32 µM Aprotinin, 16 µM Bestatin, 5.6 µM E-64, 8 µM Leupeptin and 6 µM Pepstatin A; Sigma-Aldrich] and phosphatase inhibitors (1 mM NaF, 0,3 mM Na₂P₂O₇ and 1 mM Na₃VO₄; Sigma-Aldrich). Cell lysates were collected and lysed for 30 min at 4°C in rotation. Extracts were further centrifuged for 20 min at 13.000xg at 4°C. Samples with an equivalent amount of protein were denatured at 65°C for 5 min with Laemmli SDS-PAGE sample buffer and analyzed by SDS-PAGE. This characterization was done at the Laboratory of Oncology of the Pontificia Universidad Católica de Chile, the Department of Chemistry, Pharmacology and Toxicology of the Universidad de Chile, and the Centro de Biología Celular y Biomedicina (CEBICEM) of Universidad San Sebastián.

3.3 For specific objective 1c: To evaluate the cell viability of SH-SY5Y cells exposed to nanoparticles and loaded exosomes.

3.3.1 Cell viability assay

Cell viability was evaluated by the Alamar blue assay on SH-SY5Y cells. This neuroblastoma cell line was grown in 75 cm² flasks using DMEM with high glucose content, supplemented with 10% FBS (fetal bovine serum) and 1% antibiotic and

antimycotic solution. The cells were kept in a humidified atmosphere with 5% CO₂ - 95% air at 37 °C.

SH-SY5Y cells were seeded at a density of 40,000 cells per well in 96-well plates. After 24 h, cells were incubated with gold nanorods functionalized with PEG, Chinese ink, SPIONs, exosomes from the B16F10 cell line or exosomes loaded with SPIONs at different dilutions (1, 1/10, 1/100, 1/1000 and 1/10000) for 24h. Triton X-100 at 1% for 10 minutes was applied as a positive control of cell death. Cell viability was determined by reduction of resazurin (Alamar Blue Assay) and measuring fluorescence (560 nm excitation / 590 nm emission) using a Cytation™ 5 multi-mode microplate reader from BioTek Instruments, Inc. (Winooski, USA). The results are expressed as a percentage of the control conditions of three independent experiments and three replicates per experiment.

The results of the cytotoxicity activity tests are presented as means ± standard deviation (SD). Significance was accepted at P <0.05. Statistical comparisons between groups were evaluated with Mann-Whitney statistical test.

The cell cultures and the Alamar blue assay were performed at the Laboratory of Chemistry and Pharmacy at the Pontificia Universidad Católica de Chile.

3.4 Three stages were developed for specific objective 2: To administer nanoparticle-loaded exosomes in mice via the lymphatic system, employing magnetic resonance imaging for their evaluation on the cervical and CNS tissues.

3.4.1 Stage I

The first stage was performed to validate the findings of Louveau *et al.* on the communication of lymphatic meningeal vessels with the deep cervical lymph nodes of C57BL/6 mice. Since the existence of retrograde transport of cancer exosomes through the lymphatic vessels towards the brain relies on the presence of anatomical communication between the compartments, replicating the findings of this study was key prior to interrogating any motion of biological material through these structures.

To confirm the existence of the anatomical connection between CNS ventricular and lymphatic spaces with deep cervical lymph nodes, *post-mortem* injections with Evans

Blue dye (Sigma-Aldrich) and Chinese ink (10%) were performed in the cisterna magna of mice (n=3) followed by neck evaluations. Animals were euthanized by ketamine (300mg/kg) and xylazine (30 mg/kg) overdose, and the hair of the cervical region was shaved. Skin and subcutaneous tissue were dissected at the midline of the neck, extending the field laterally at the supraclavicular area until both mandibular glands were exposed. Glands were detached from the clavicle surface and moved cranially. The sternocleidomastoid muscles were then displaced until the deep cervical nodes, surrounded by adipose tissue were identified.

A syringe with a 30G needle was loaded with a 1% solution of Evans Blue (dye content $\geq 75\%$, 960.81 g/mol) or Chinese ink (10%) in distilled water. Sequential injections of 50 μ L, 100 μ L, and 150 μ L of the solution were administered in the cisterna magna; by placing the mouse in prone position, flexing the head at a 135⁰ angle with the body, and penetrating directly underneath and laterally to the end of the occipital bone towards the foramen magnum through the intact skin. After every injection, mice were immediately placed in supine position under a stereoscopic microscope for image acquisition.

Experiments for this stage were conducted at the School of Veterinary Medicine of the Pontificia Universidad Católica de Chile.

3.4.2 Stage II

Once the reproducibility of the findings of Louveau *et al.* was verified, the inverse route was tested with an Evans blue injection in the deep cervical lymph nodes of C57BL/6 mice (n=3). One sham control mouse was included besides the Evans blue group. The presence of subsequent staining of the ventricular space and brain parenchyma by anatomical analysis was determined. The purpose of this experiment was a first approximation to measuring the efficacy of the cervical and meningeal lymphatic vessels as a two-way lane for transport between compartments. This was done before interrogating the system with more complex biological structures, as cancer exosomes.

To evaluate the anatomical possibility of retrograde flow from neck lymphatic structures to the CNS spaces, *post-mortem* injections with Evans Blue dye were administered in the deep cervical lymph nodes of mice (n=3) followed by partial craniectomy. Animals were euthanized by ketamine (300mg/kg) and xylazine (30 mg/kg) overdose, cervical region

shaved, and dissection for lymph node identification as previously described. A syringe with a 30G needle was loaded with a 1% solution of Evans Blue (dye content ≥ 75 %, 960.81 g/mol) in distilled water. An injection of 100 μ L of the solution was administered in the deep cervical lymph node. After every injection, we immediately proceeded to craniectomy by electrical drilling of a triangular window. The intact brain and meninges were exposed 10 min after administration. Mice were placed in prone position under a stereoscopic microscope for image acquisition.

Experiments for this stage were conducted at the School of Veterinary Medicine of the Pontificia Universidad Católica de Chile with the collaboration of Dr. Claudia Yefi.

3.4.3 Stage III

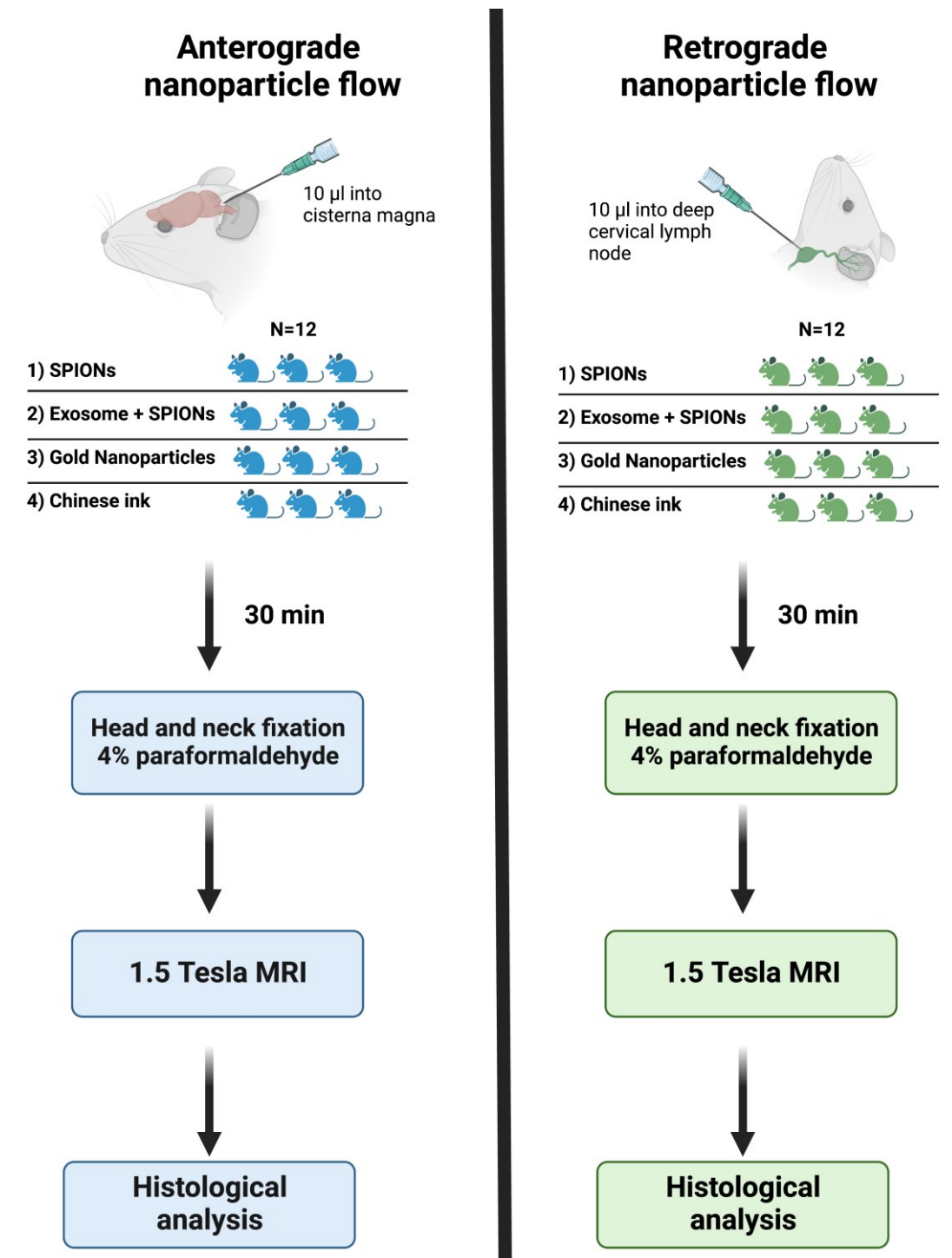


Figure 4. Evaluation of anterograde and retrograde flow of different nanoparticle solutions through the cervical and meningeal lymphatic system.

The purpose of this experiment was to evaluate the anterograde and retrograde flow through the cervical and meningeal lymphatic vessels of cancer exosomes using SPIONs for MRI signaling purposes (Fig. 4). The anterograde flow was defined as the classically

described motion of lymphatic components towards the thorax. The retrograde flow was defined as the possibility of the different nanoparticle solutions injected into the deep cervical lymph node to travel towards the meningeal lymphatic vessels and the brain. However, given the pharmacological relevance that a new entrance point to the brain can have, SPIONs, gold, and Chinese ink nanoparticles were also tested.

For *post-mortem* anterograde evaluations different nanoparticle solutions (gold nanoparticles and Chinese ink concentrations are seen in Table 3) were injected into the cisterna magna of C57BL/6 mice (n=3 per condition), after euthanasia by ketamine (300mg/kg) and xylazine (30 mg/kg) overdose. Milli-Q water and distilled water injections were used for controls (n=3 per condition). A syringe with a 30G needle was loaded with 50 μ L of each solution and administered in the cisterna magna; by placing the mouse in prone position, flexing the head at a 135⁰ angle with the body, and penetrating directly underneath and laterally to the end of the occipital bone towards the foramen magnum through the intact skin. The head and neck were preserved by fixation with 4% paraformaldehyde for histological Gold Enhancement analysis.

For *post-mortem* retrograde flow evaluation different nanoparticle solutions (concentrations are seen in Table 3) were injected into the deep cervical lymph node of C57BL/6 mice (n=3 per condition), after euthanasia by ketamine (300mg/kg) and xylazine (30 mg/kg) overdose. Milli-Q water and distilled water injections were used for controls (n=3 per condition). A syringe with a 30G needle was loaded with 50 μ L of each solution and administered into the deep cervical lymph node. To locate the lymph node skin and subcutaneous tissue were dissected at the midline of the neck, extending the field laterally at the supraclavicular area until both mandibular glands were exposed. Glands were detached from the clavicle surface and moved cranially. The sternocleidomastoid muscles were then displaced until the deep cervical nodes, surrounded by adipose tissue, were identified. The head and neck were preserved by fixation with 4% paraformaldehyde for histological Gold Enhancement analysis.

For *in vivo* anterograde flow evaluation different nanoparticle solutions (SPIONs, exosomes loaded with SPIONs, gold nanoparticles, and Chinese ink concentrations are seen in Table 3) were injected into the cisterna magna of C57BL/6 mice (n=3 per condition). Milli-Q water, distilled water, phosphate buffer saline, and mice with no injections were used for controls (n=3 per condition). Animals were anesthetized with isoflurane and kept under anesthesia with a nasal cannula supplying 1% isoflurane during

the entire procedure. A syringe with a 30G needle was loaded with 10 μL of each solution and administered in the cisterna magna; by placing the mouse in prone position, flexing the head at a 135° angle with the body, and penetrating directly underneath and laterally to the end of the occipital bone towards the foramen magnum through the intact skin. Euthanasia by excess anesthesia was performed 30 min after injection. The head and neck were preserved by fixation with 4% paraformaldehyde for MRI and histological analysis.

For *in vivo* retrograde flow evaluation different nanoparticle solutions (concentrations are seen in Table 3) were injected into the deep cervical lymph node of C57BL/6 mice (n=3 per condition). Milli-Q water, distilled water, phosphate buffer saline, and mice with no injections were used for controls (n=3 per condition). Animals were anesthetized with isoflurane and kept under anesthesia with a nasal cannula supplying 1% isoflurane during the entire procedure. A syringe with a 30G needle was loaded with 10 μL of each solution and administered into the deep cervical lymph node. To locate the lymph node skin and subcutaneous tissue were dissected at the midline of the neck, extending the field laterally at the supraclavicular area until both mandibular glands were exposed. Glands were detached from the clavicle surface and moved cranially. The sternocleidomastoid muscles were then displaced until the deep cervical nodes, surrounded by adipose tissue, were identified. Euthanasia by excess anesthesia was performed 30 min after injection. The head and neck were preserved by fixation with 4% paraformaldehyde for MRI and histological analysis.

The process of image acquisition was performed with a clinical 1.5 Tesla MRI scanner (Philips Achieva). Perls' Prussian blue was used for iron tissular content analysis. Gold Enhancement was used for gold and Chinese ink analysis.

3.4.4 Gold nanoparticle synthesis

For the preparation of a seed solution of GNPs, a cold-prepared sodium borohydride solution (600 μL , 0.01 M) was added to 250 μL of 0.01 M HAuCl_4 in 9.75 mL of 0.1 M cetyltrimethylammonium bromide (CTAB) in a flask, under vigorous magnetic stirring. The seed solution was kept at 27°C for 2 h, before use. After that, 55 μL of 0.1 M ascorbic acid solution (Sigma Chemical Co., St. Louis, MO, USA) was added to a growth solution containing 75 μL of 0.01 M AgNO_3 (Sigma Chemical Co., St. Louis, MO, USA), 9.5 mL of 0.1 M CTAB, and 500 μL of 0.01 M HAuCl_4 . Further, 250 μL of 0.1 M HCl and 12 μL of the previously prepared seed solution were added. The solution was incubated for

10 min at 27 °C and then centrifuged at a 7030× g for 15 min. After centrifugation, the supernatant was removed, and the pellet was resuspended in milli-Q water.

The GNRs were conjugated with asymmetrical PEGs that have a thiol group (SH) at one end, and a methoxy (HS-PEG-OMe MW 5K, JenKem Technology, TX, USA) or a carboxylic acid group (HS-PEG-COOH MW 5K, JenKem Technology, TX, USA) at the other. A total of 50 μL of 1 mM HS-PEG-OMe in a water solution was added to 10 mL of 1 nM GNRs-CTAB and stirred for 10 min. After centrifugation at RCF of 16,100× g for 10 min, the pellet was resuspended in 10 mL of milli-Q water. Subsequently, 300 μL of 1 mM HS-PEG-COOH solution was added into the water solution, and the suspension obtained was stirred for one hour. Further, the suspension was centrifuged at 16,100× g for 10 min, and the pellet was resuspended in 100 μL of 0.1 M 2-(N-morpholino)ethanesulfonic acid (MES) buffer pH 5.5. Subsequently, 0.2 mg of ethyl-3-(3-dimethylaminopropyl)-carbodiimide (EDC) and 0.5 mg of sulfo-N-hydroxysuccinimide (Sulfo-NHS) in 100 μL of MES were added and mixed for 15 min. The excess of EDC/Sulfo-NHS was subsequently removed by centrifugation at 16,100× g for 10 min.

3.4.5 Characterization of gold and Chinese ink nanoparticles

The morphology and particle size of SPIONs was investigated by transmission electron microscopy (STEM, FEI Quanta 250) operating at 10.00 kV. Dynamic light scattering system for nanoparticle analysis was used for size determination. The superficial charge was measured by a Zeta Potential Analyzer. Concentrations obtained from the synthesis were measured using Nanoparticle Tracking Analysis (NTA) by NanoSight. Chinese ink was obtained from commercially available ARTEL and used at a concentration of 10%.

Table 3. Nanoparticle concentrations used for anterograde and retrograde flow evaluations.

Nanoparticle	Concentration
SPIONs	3200 µg/mL
Exosomes + SPIONs	1.67×10^{11} particles/mL
Gold nanoparticles	1.71×10^{14} particles/mL
Chinese ink	10%

3.5 For specific objective 3: To validate through histological analysis the presence of nanoparticle-loaded exosomes in the meningeal lymphatic vessels.

3.5.1 Formalin-fixed, paraffin-embedded (FFPE) tissue processing for histology and special stains

Whole brain and neck samples were fixed for 24 hours on 4% PFA and then processed for paraffin embedding. Coronal sections of 4 µm were cut from each paraffin block, then sections were dried, deparaffinized and re-hydrated on distilled water. Gold Enhancement was performed with Nanoprobes GoldEnhance™ LM Kit according to manufacturer's instructions. Once this procedure was done, the sections were counterstained with eosin. Nanoparticles were illustrated by Perls' Prussian blue staining for iron content (31). Tissue was deparaffinized and hydrated with distilled water, immersed in 10% aqueous potassium ferrocyanide and 20% aqueous hydrochloric acid for 20 min. Images of the stained slides were taken with an ICC50W Camera on a DM500 Leica Microscope at 4x, 10x, 20x, and 40x magnification.

Immunohistochemistry analysis was performed on the different sections with joint staining with Gold Enhancement and Perls' Prussian blue to evaluate colocalization with an endothelial marker of lymphatic vessels (LYVE-1). After deparaffinization, antigen recovery was done using buffer Tris-EDTA pH 9.0 in a pressure cooker for 20 min. Endogenous peroxidase was blocked with 3% hydrogen peroxide for 15 min. Blocking of non-specific binding was performed with 3% BSA/PBS for 30 min. Overnight incubation at 4°C with the primary antibody, Recombinant Anti-LYVE1 antibody [EPR21771] (ab218535), was done at 1:5000 dilution. This was followed by incubation with the secondary antibody, Goat Anti-Rabbit IgG H&L (HRP) ab6721 (Abcam), for 1 hour at 25°C. Each slide was then developed with DAB for 1 min. Lung, gall bladder,

and spleen tissues were used as controls. Quantification of histological images were performed with the software Image J.

Histological analyses were conducted in the Histology Department of the Advanced Center for Chronic Diseases at the Universidad de Chile.

3.6 Animals

Male C57BL/6 mice were purchased from the animal facility of the Pontificia Universidad Católica de Chile and housed in temperature and humidity-controlled rooms, maintained on a 12h/12h light/dark cycle. All procedures complied with regulations of the CEC-CAA (Comité Ético Científico para el Cuidado de Animales y Ambiente) of the Pontificia Universidad Católica de Chile. Only adult animals (eight to ten weeks) were used in this study. The sample size was chosen following similar, previously published experiments (89,94–96). Animals from different cages in the same experimental group were selected to assure randomization.

3.7 Statistical Analysis

A chi-squared test was used for comparison of categorical variables. The rest of the statistical analyses were done using nonparametric statistics. Values such as the median and interquartile ranges were used for description. Group differences were determined by the Wilcoxon test for two-level comparisons or the Kruskal-Wallis test for multiple comparisons, and when significant, followed by a Dunn post-hoc test. All these analyses were done using software SPSS v25 (IBM Corp., IL, USA).

Experiments for this stage were conducted at the Center for Medical Investigations, School of Medicine of the Pontificia Universidad Católica de Chile.

Chapter 4: Results

4.1 Specific objective 1a

4.1.1 SPIONs characterization for 1.5 T MRI

Coprecipitation of ferric and ferrous chlorides with ammonium associated with an acidic pH of 1 produced appropriate iron nanoparticle sizes below 10 nm. Dynamic light scattering analysis revealed a mean diameter of 9 nm for the iron-nanoparticles regardless of centrifugation or Milli-Q serial washes after synthesis (Figure 5B). The superficial net charge was positive, at approximately 40 mV (Figure 5C). Electron microscopy confirmed nanoparticles of about 8 nm with few aggregates in the solution (Figure 5A).

The first series of syntheses included samples with sodium citrate stabilization. Measurements by NTA showed a higher concentration in the sodium citrate stabilized SPIONs compared to nanoparticles (NP) alone (2.17×10^{13} NP/mL vs. 6.16×10^{12} NP/mL). Subsequent syntheses without stabilization had a concentration of similar magnitudes at 4.3×10^{12} NP/mL. pH measured qualitatively through pH test strips was sensitive to Milli-Q water washes. Citrate stabilization and nanoparticles alone in the first syntheses produced acidic SPIONs of pH=2. Subsequent syntheses were centrifuged to minimize the number of nanoparticles lost in washes. After washing once, pH was increased to values between 6 and 7.

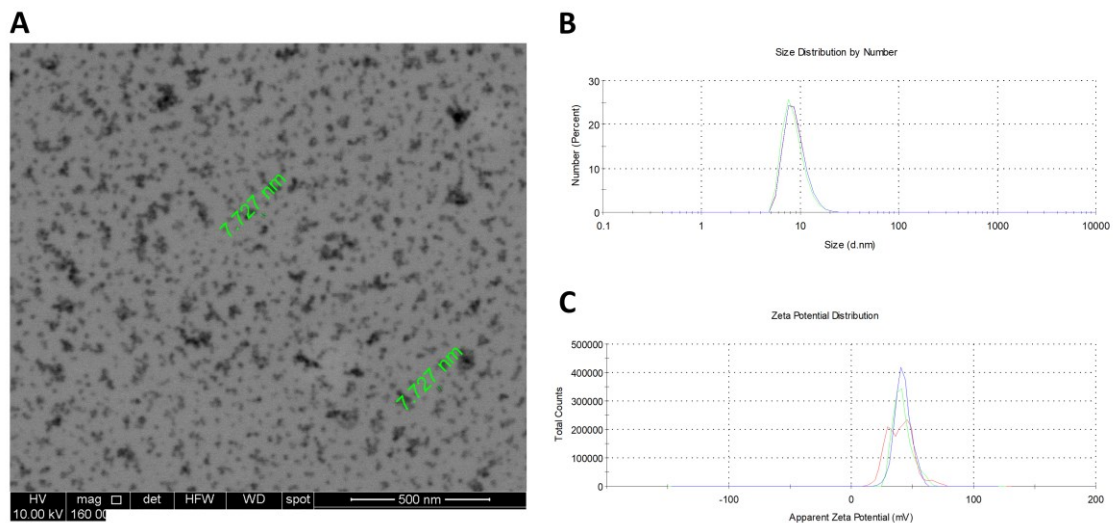


Figure 5. Iron oxide nanoparticles characterization. (A) Scanning transmission electron microscopy (STEM) of iron oxide nanoparticles in Milli-Q water solution. (B) SPIONs sizes measured in nanometers (nm) by Dynamic Light Scattering Analysis after coprecipitation method and series of centrifugations. (C) Net surface charge measured in millivolts (mV) by the Zeta Potential Analyzer.

4.1.2 Optimal concentration of SPIONs for 1.5 T MRI signal detection

Non-stabilized and sodium citrate stabilized SPIONs underwent an initial evaluation based on the percentage of stock dilutions per condition (80%, 60%, 40%, 20%, 10%, 1%) as a first approximation to MRI detection thresholds (Figure 6A). T1, T2, and T2* weighted MRI map parameters were able to detect SPIONs at 1% concentration in primary stocks, corresponding to a magnitude of 10^{10} nanoparticles per milliliter. Higher concentrations were unable to detect any signal. Agarose controls showed a T1 time close to 1800 ms, similar to that of water visualization in MRI analysis. T1 times of 1% SPIONs were below 400ms (Figure 6B). T2 times of SPIONs were below 200ms and T2* times were below 50ms (Figure 6C and 6D). Using this data, an upper limit of detection range was established at a concentration of 10^{10} NP/mL.

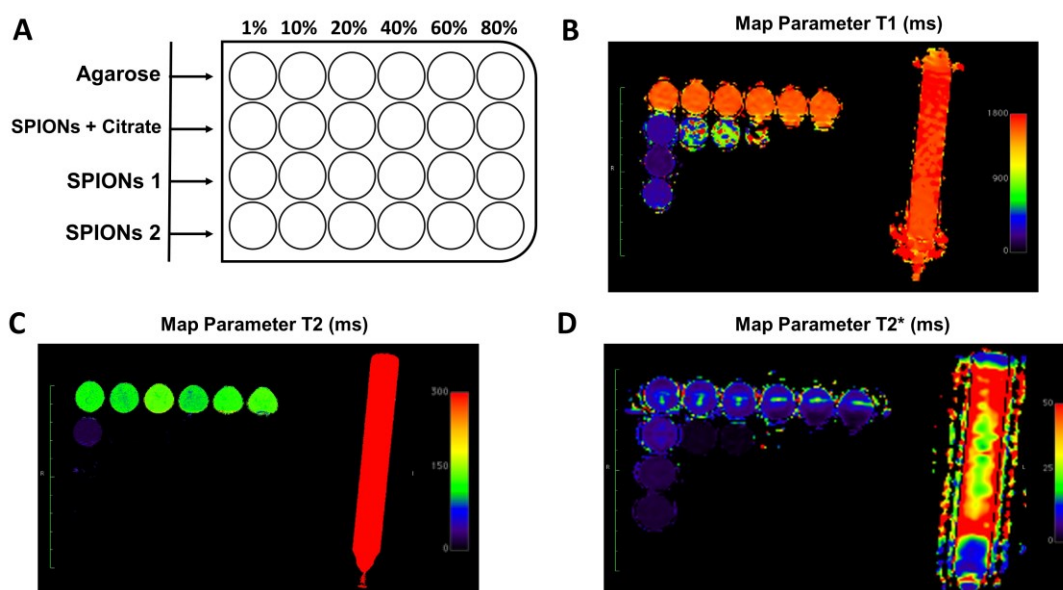


Figure 6. MRI visualization of different percentages of SPION synthesized stocks. (A) 24 well configuration. (B) T1 (ms) 1.5T MRI map parameter. (C) T2 (ms) 1.5T MRI map parameter (D) T2* (ms) 1.5TMRI map parameter.

To evaluate the lower limit of detection range in 1.5T MRI, 10 samples of SPIONs were prepared at decreasing concentrations by a factor of 10, starting at 10^{10} NP/mL. Iron-nanoparticle solutions with human blood and Milli-Q water were prepared, and plain blood, agarose and Milli-Q water in Eppendorf tubes as controls. Detection occurred at two marked concentrations in both human blood and Milli-Q water SPION solutions: 10^{10} and 10^9 nanoparticles per milliliter (Figure 7A and 7B). SPIONs at concentrations of 10^8 NP/mL also presented a signal, although weak. T1 weighted MRI map parameters showed times close to or below 400 ms at 10^{10} and 10^9 NP/mL (Figure 7C). T1 Milli-Q controls were at 2481.8 ± 61.9 ms and agarose at 2133.0 ± 15.7 ms. All other concentrations were in time intervals above 1250 ms at T1. A lower limit of detection range was established at a concentration of 10^9 NP/mL. T2 data concurred with T1 parameters of concentration range detection in 1.5 T MRI.

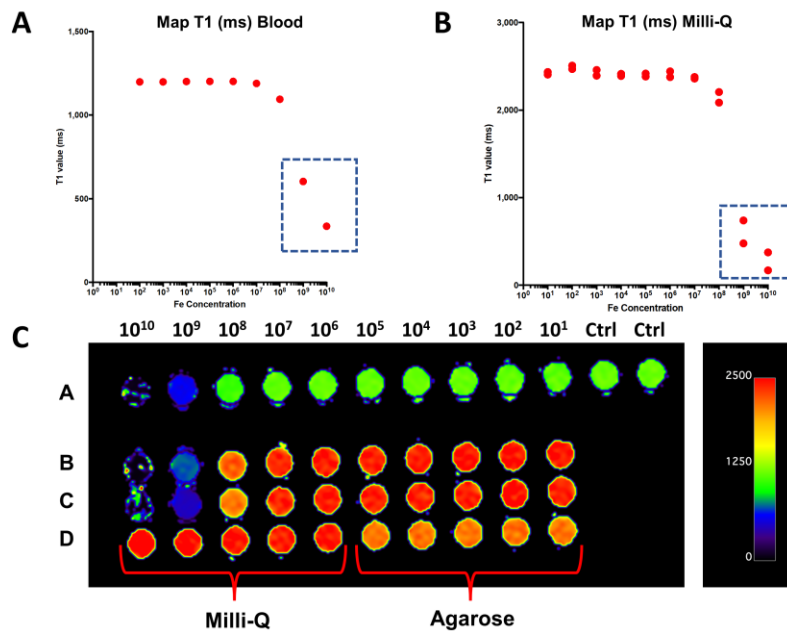


Figure 7. T1(ms) weighted MRI map parameters. (A) Concentration thresholds for contrast detection in blood. (B) Concentration thresholds for contrast detection in Milli-Q water solution. (C) Map parameters for SPIONs dissolved in blood and Milli-Q water; water and agarose controls are shown.

When 2g of chicken muscular tissue slices were used, MRI visualization of SPIONs had overall T1 times between 600 and 800ms. Even though the T1 time maps were close to non-pathological muscular tissue (about 800 ms), the T1 intensity revealed a hypointense area circumscribed to the injection site in concentrations of 1×10^{10} , 5×10^9 , 1×10^9 , and a weaker area in 5×10^8 nanoparticles per milliliter (Figure 8A). Muscle exposed to SPIONs + Gadobutrol showed mostly T1 times below 600 ms with a hyperintense signal. All Gadobutrol controls also presented T1 times lower than 600 ms. Gadobutrol produced better contrast visualization, with lower T1 times.

Assessment of T1 maps of complete chicken chest muscular tissue revealed that SPIONs can be visualized at 10^{10} NP/mL and even lower concentrations (10^8 and 10^6 NP/mL), despite being a disperse signal through the tissue, with T1 times lower than 500ms (Figure 8B). SPIONs + Gadobutrol produced a more restricted and clearly defined area after injections, with T1 times of less than 300ms. SPIONs dissolved in blood also revealed circumscribed areas of MRI signal enhancement with T1 times lower than 300ms. Therefore, aqueous solutions can be visualized in MRI at concentrations that range between 10^9 to 10^{10} nanoparticles per milliliter, while muscular tissue appears to allow for lower concentration visualization at 10^6 nanoparticles per milliliter, although a weaker signal.

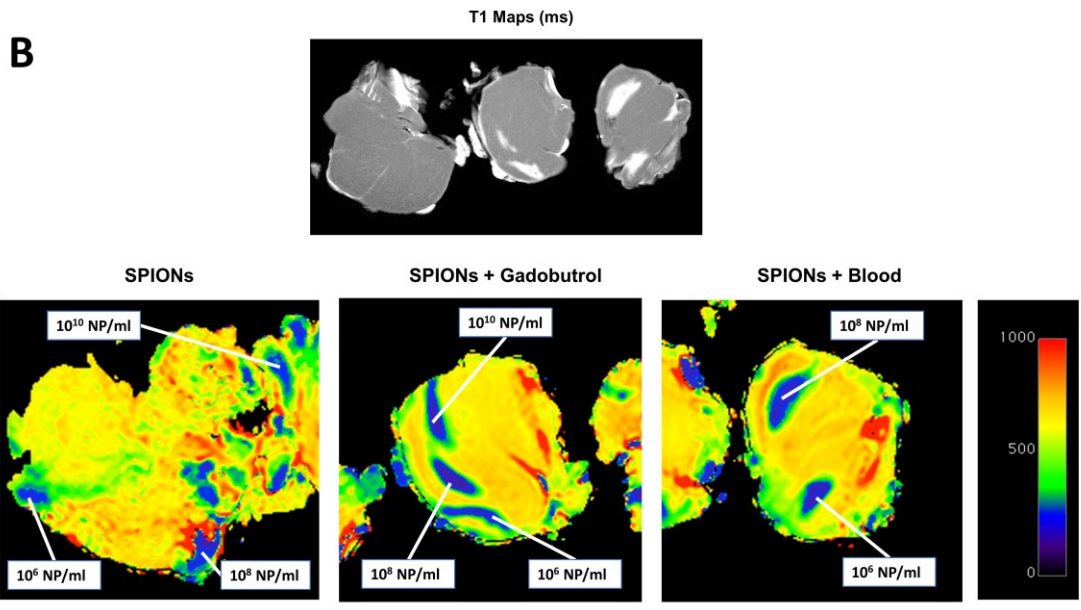
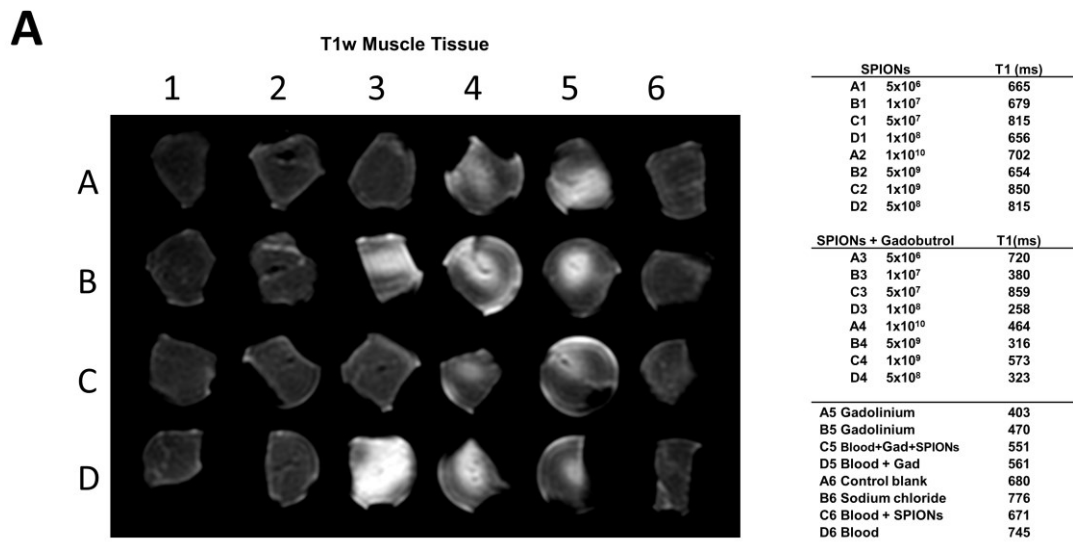


Figure 8. MRI SPION analysis on chicken muscular tissue. (A) T1 weighted image and time (ms) rates for SPIONs, gadobutrol, and blood concentrations. (B) T1 map parameters (ms) for SPION injections in whole chest chicken muscle at different concentrations.

4.2 Specific objective 1b

4.2.1 Exosome purification and characterization

Exosome characterization with DLS revealed an average size of $41.8 \text{ nm} \pm 1.6$ (Figure 9A), and a mean zeta potential of $-10.8 \pm 2.5 \text{ mV}$. The MicroBCA (ThermoScientific) assay kit was used for total protein quantitation. Measurements were performed with and without lysis with radio immunoprecipitation assay (RIPA) buffer (ThermoScientific). Concentration results are shown in Table 4. Electron microscopy of exosomes can be seen in Figure 9B. Western blot analysis confirmed the presence of EV markers EEA1 and TSG101 (Figure 10).

Table 4. MicroBCA Quantitation of Total Protein

	Concentration ($\mu\text{g/mL}$)	Average absorbance (562 nm)	Average minus blank (562 nm)
2 μL B16F10 EVs	114.01	1.13	1.05
2 μL B16F10 EVs Lysate	91.01	0.92	0.85
5 μL B16F10 EVs	218.39	2.06	1.98
5 μL B16F10 EVs Lysate	186.26	1.77	1.70

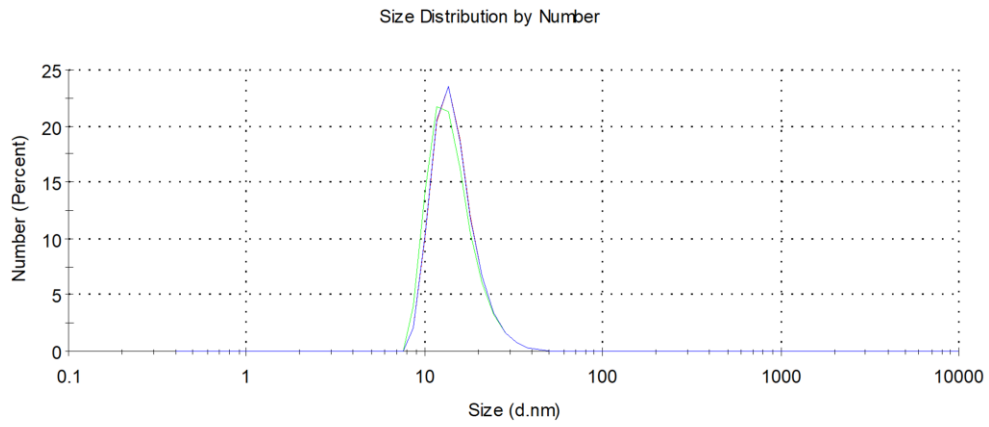
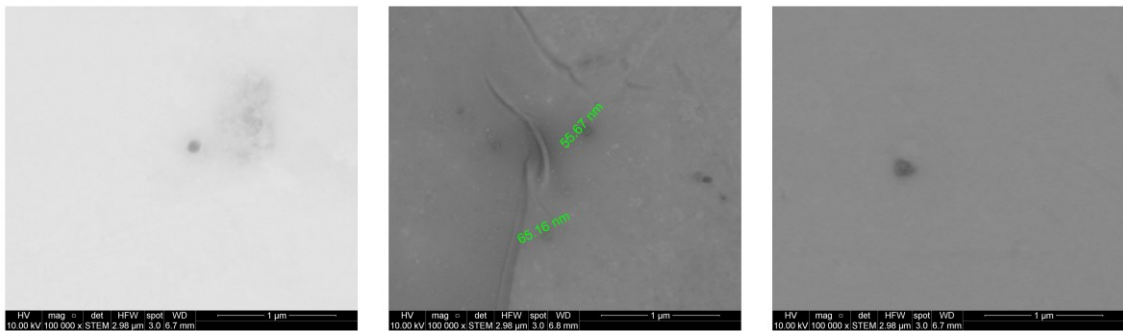
A**B**

Figure 9. Characterization of B16F10 exosomes. (A) DLS size characterization of B16F10 purified exosomes. (B) Electron microscopy of B16F10 exosomes.

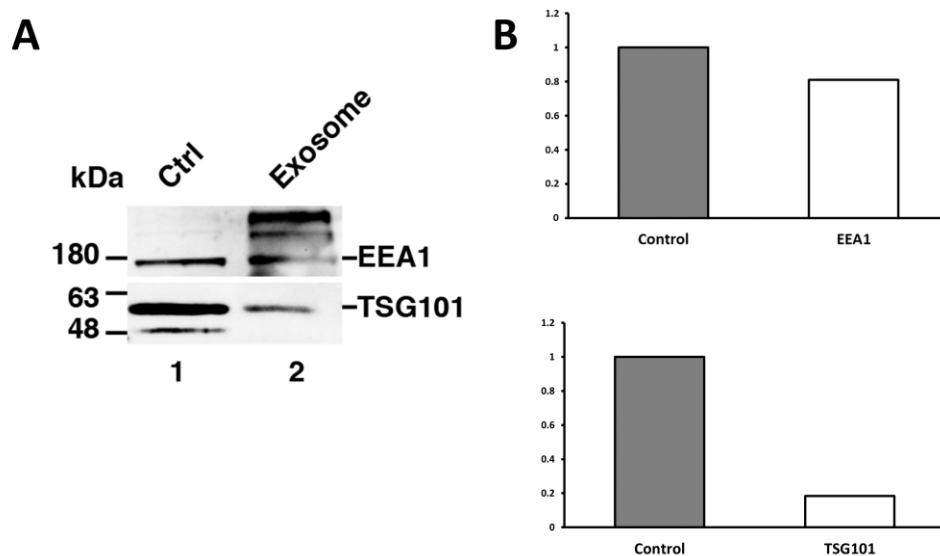


Figure 10. Western blot analysis. (A) Western blot of EV markers EEA1 and TSG101. Control was performed using a cellular extract from the B16F10 melanoma cell line. (B) Western Blot quantification of EEA1 and TSG101 with respect to control.

4.2.2 SPION functionalization and characterization for exosome loading

In preparation for exosome loading, samples of iron oxide nanoparticles were processed by chemical coprecipitation from $\text{FeCl}_3 \cdot 6\text{H}_2\text{O}$ (432 mg), and $\text{FeCl}_2 \cdot 4\text{H}_2\text{O}$ (159mg) and functionalized with PEG 5000- NH_2 (1 mg in 1 mL of Milli-Q water), PEG 5000-COOH (1 mg in 1 mL of Milli-Q water), PVP (1 mg in 1 mL of Milli-Q water), or alginate (1 mg in 1 mL of Milli-Q water), as previously described.

DLS of iron nanoparticles showed a mean (\pm SD) diameter of 14.28 ± 5.57 nm (Figure 11A). The zeta potential was positive at 36.9 ± 0.51 mV (Figure 11B). Transmission electron microscopy (TEM) confirmed SPION mean size of 7.08 ± 2.2 nm (Figure 12). Total iron concentration of prepared stock samples determined by atomic absorption spectroscopy was 3200 mg/L. After a ten-fold stock dilution with Milli-Q water, pH measured qualitatively through pH test strips was 7.

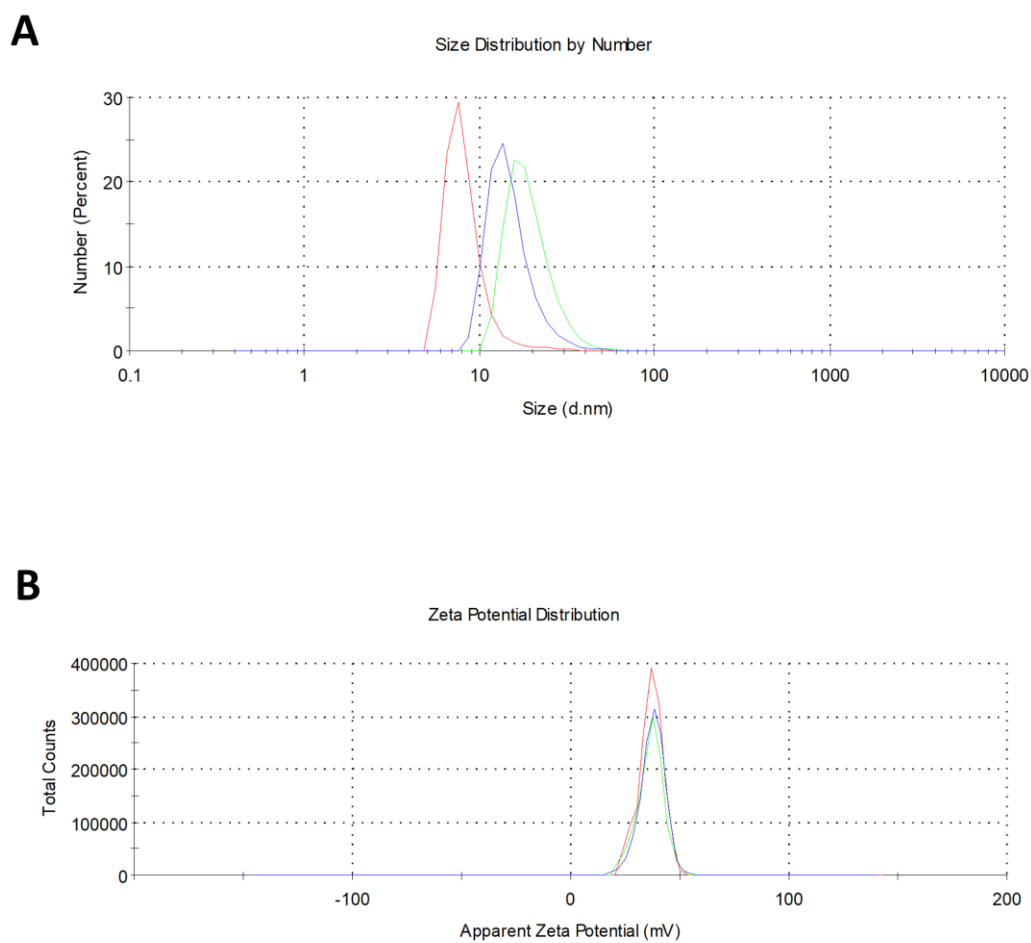


Figure 11. SPION characterization. (A) DLS analysis of SPION size distribution. (B) Zeta potential characterization of SPIONs.

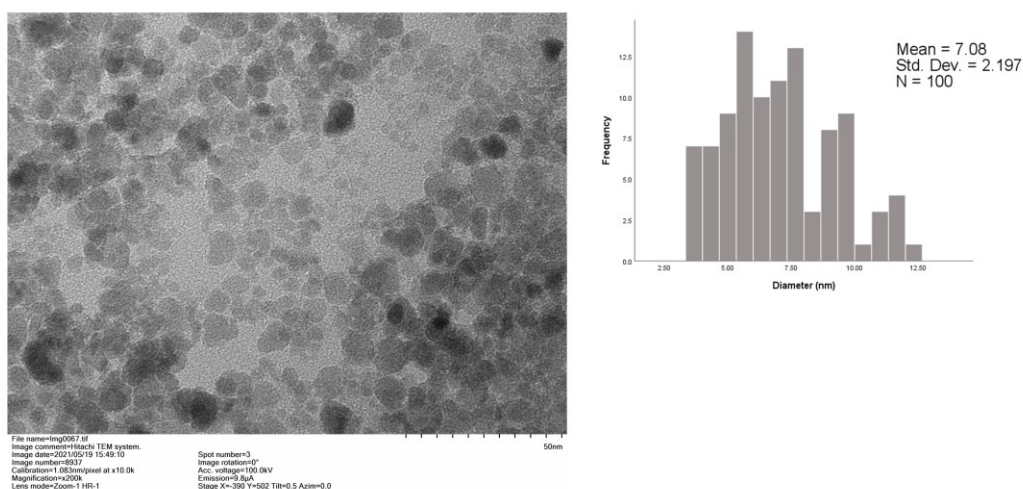


Figure 12. STEM visualization and histogram of SPIONs.

Table 5 shows the mean (\pm SD) size and zeta potential of functionalized SPIONs. Increase in mean size and changes in superficial net charge indicate successful functionalization of all tested systems. As mean sizes of functionalized SPIONs were close to those obtained from exosome purification, only SPIONs without functionalization were further used for loading into exosomes through electroporation.

Table 5. DLS characterization of functionalized SPIONs

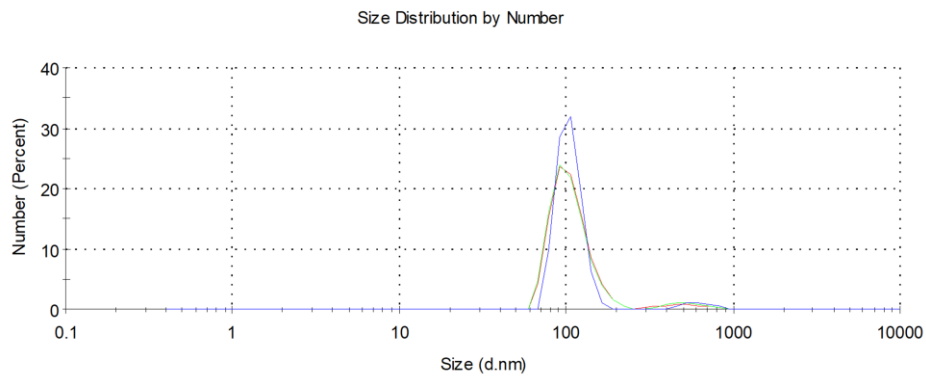
Functionalization	Mean size (\pm SD) (nm)	Mean Z potential (\pm SD) (mV)
PEG 5000-NH2	31.9 \pm 1.83	39.5 \pm 1.22
PEG 5000-COOH	39.16 \pm 9.84	40.2 \pm 3.20
PVP	42.12 \pm 3.45	16.2 \pm 0.25
Alginate	41.03 \pm 30.48	-1.35 \pm 0.81

4.2.3 Exosome loading with SPIONs

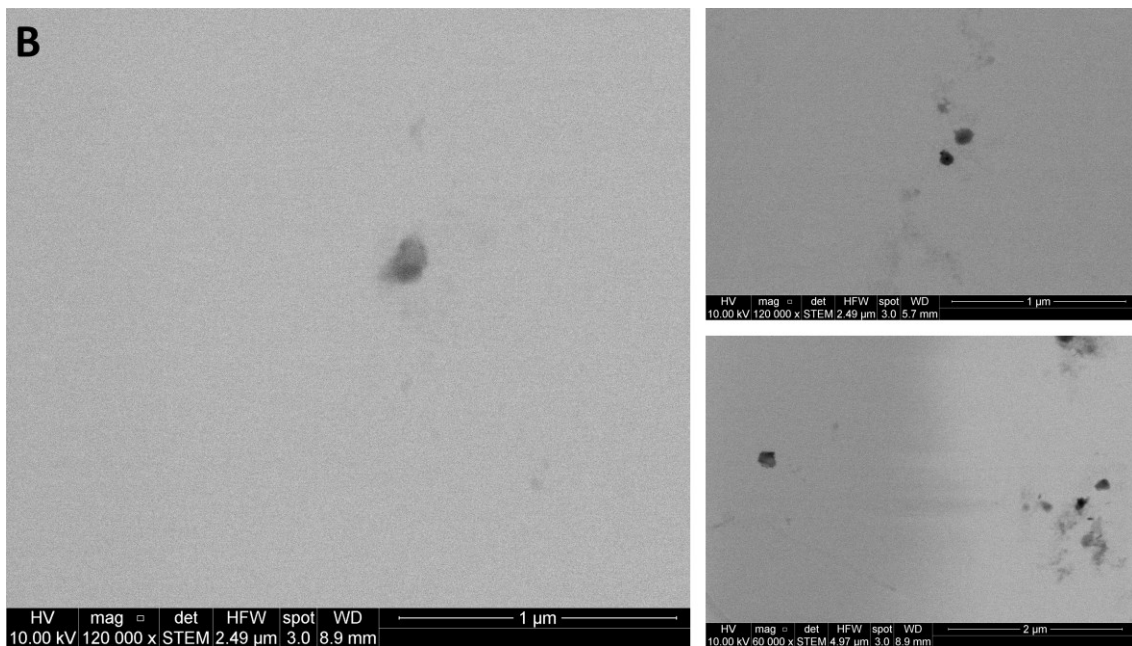
Exosomes purified from the B16F10 melanoma cell line were electroporated with SPIONs as previously described. After reisolating the labeled exosomes with Exo-spin columns, DLS revealed an exosome population of an average size of 106 nm \pm 27.35

(Figure 13A) and a mean zeta potential of -17.1 ± 0.53 mV. Electron microscopy showed the presence of SPIONs within the extracellular vesicles (Figure 13B). Figure 13C shows both B16F10 exosomes and exosomes electroporated with SPIONs as seen in electron microscopy.

A



B



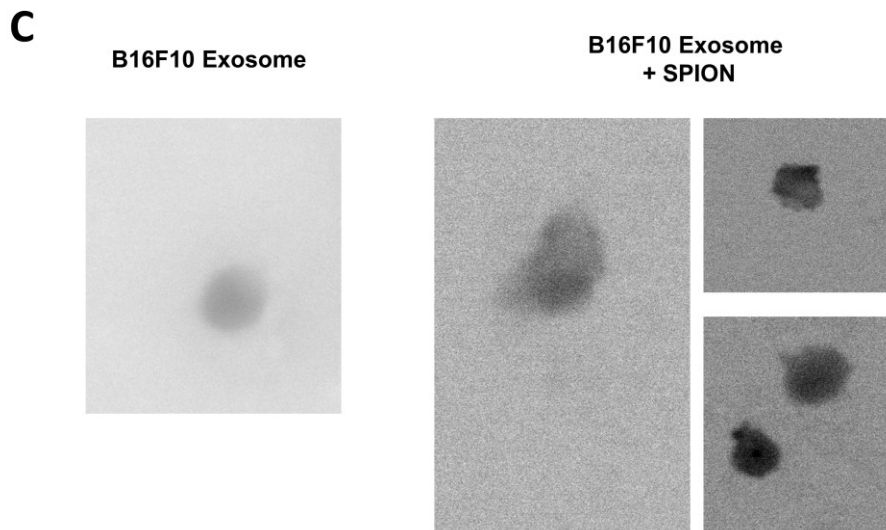


Figure 13. Exosome + SPIONs characterization. (A) DLS size characterization of electroporated exosomes. (B) STEM visualization of electroporated exosomes. (C) STEM visualization of exosomes with and without SPIONs labeling.

4.3 Specific objective 1c

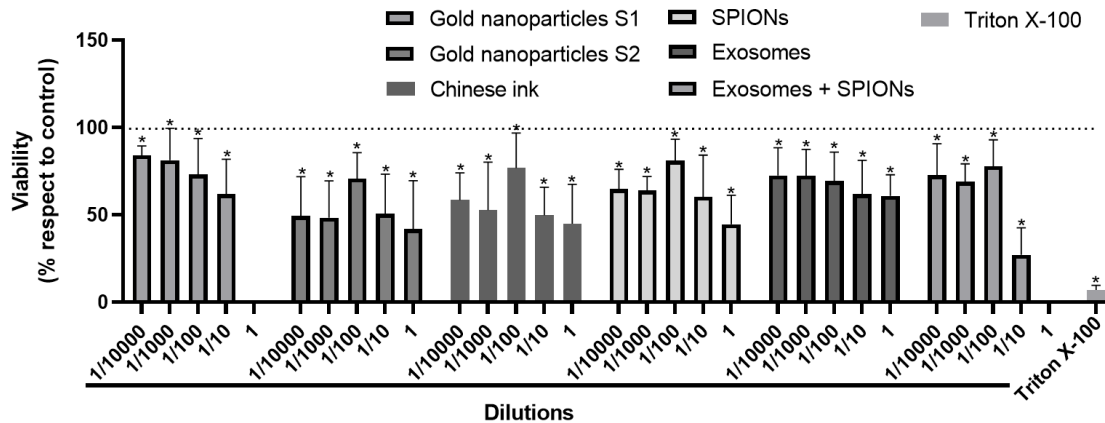


Figure 14. Cell viability at different nanoparticle concentrations. SPIONs indicates superparamagnetic iron oxide nanoparticles. The asterisks (*) represent statistically significant differences ($p < 0.05$).

Cell viability was evaluated by Alamar blue of SH-SY5Y cells lines treated with gold nanoparticles from two synthesis (S1 and S2) functionalized with PEG, Chinese ink, SPIONs, exosomes from B16F10 cell line or exosomes loaded with SPIONs at different dilutions (1, 1/10, 1/100, 1/1000 and 1/10000) for 24h (Fig. 14). Positive control of cell death, cells treated with Triton X-100 at 1% for 10 minutes. Data are expressed as percentage of viability with respect to control cells. Data are shown as mean \pm SD ($n =$

3). Mann-Whitney statistical test was performed between the control group and different nanoparticles concentrations. The asterisks (*) represent statistically significant differences ($p < 0.05$). Figure 14 shows that although the cell viability is reduced by the exposure to the different concentrations of nanoparticles, viability is preserved between 50-80% with respect to controls, particularly under the 1/10 dilution of each condition. Accordingly, we used concentrations below a dilution of 1/10 of the corresponding nanoparticle solutions for *in vivo* experiments.

4.4 Specific objective 2a

4.4.1 Mice intracerebroventricular injection of Evans Blue dye

To confirm the existence of the anatomical connection between CNS ventricular and lymphatic spaces with deep cervical lymph nodes, *post-mortem* injections with Evans Blue dye (Sigma-Aldrich) were performed in the cisterna magna of mice ($n=3$) followed by neck evaluations. Intracerebroventricular injections through the cisterna magna showed staining of deep cervical lymph nodes within the first minute after the administration of Evans Blue dye in all mice (Figure 15).

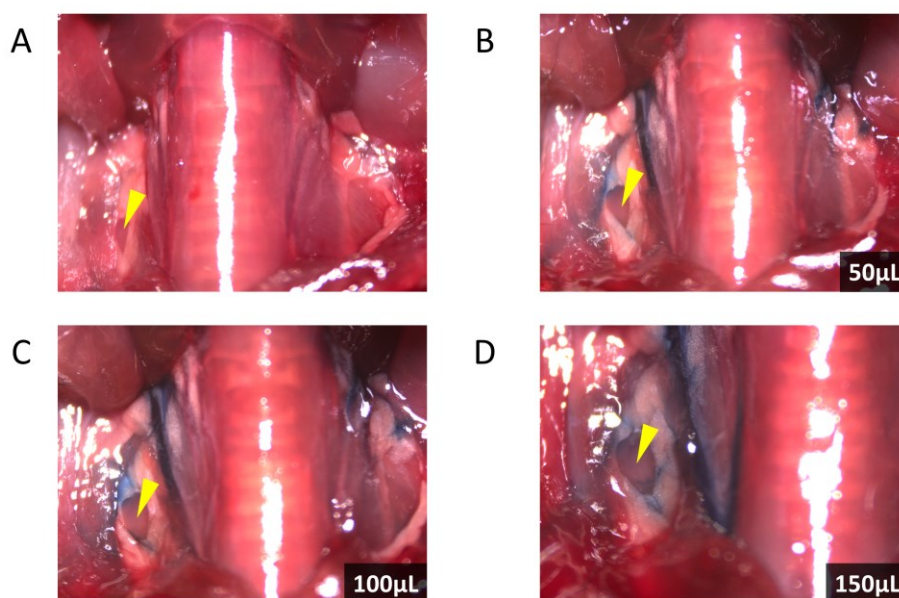


Figure 15. Intracerebroventricular injection of Evans Blue dye. (A) Right deep cervical lymph node before dye administration. (B-D) Sequential injections of 50µL, 100µL, and 150µL of 1% Evans Blue dye into the cisterna magna. Yellow arrowheads indicate the lymph node.

4.5 Specific objective 2b

4.5.1 Mice deep cervical lymph node injection with Evans Blue dye

To evaluate the anatomical possibility of retrograde flow from neck lymphatic structures to the CNS spaces, *post-mortem* injections with Evans Blue dye were administered in the deep cervical lymph nodes of mice (n=3) followed by partial craniectomy. Animals were euthanized by ketamine (300mg/kg) and xylazine (30 mg/kg) overdose, cervical region shaved, and dissection for lymph node identification as previously described. A syringe with a 30G needle was loaded with a 1% solution of Evans Blue (dye content $\geq 75\%$, 960.81 g/mol) in distilled water. An injection of 100 μ L of the solution was administered in the deep cervical lymph node. After every injection, we immediately proceeded to craniectomy by electrical drilling of a triangular window. The intact brain and meninges were exposed in about 10 min since administration. Mice were placed in prone position under a stereoscopic microscope for image acquisition. Deep cervical lymph node injections showed staining of the meninges and brain parenchyma in all mice, in a pattern consistent to the territory adjacent to venous sinuses and perivenous regions, which corresponds to the expected description of meningeal lymphatics running parallel to venous structures (Figure 16).

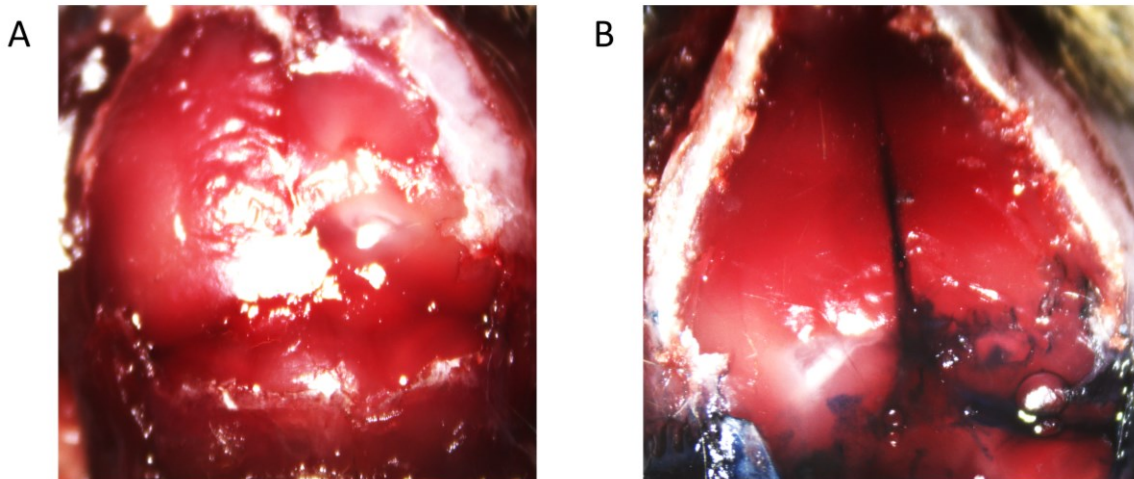
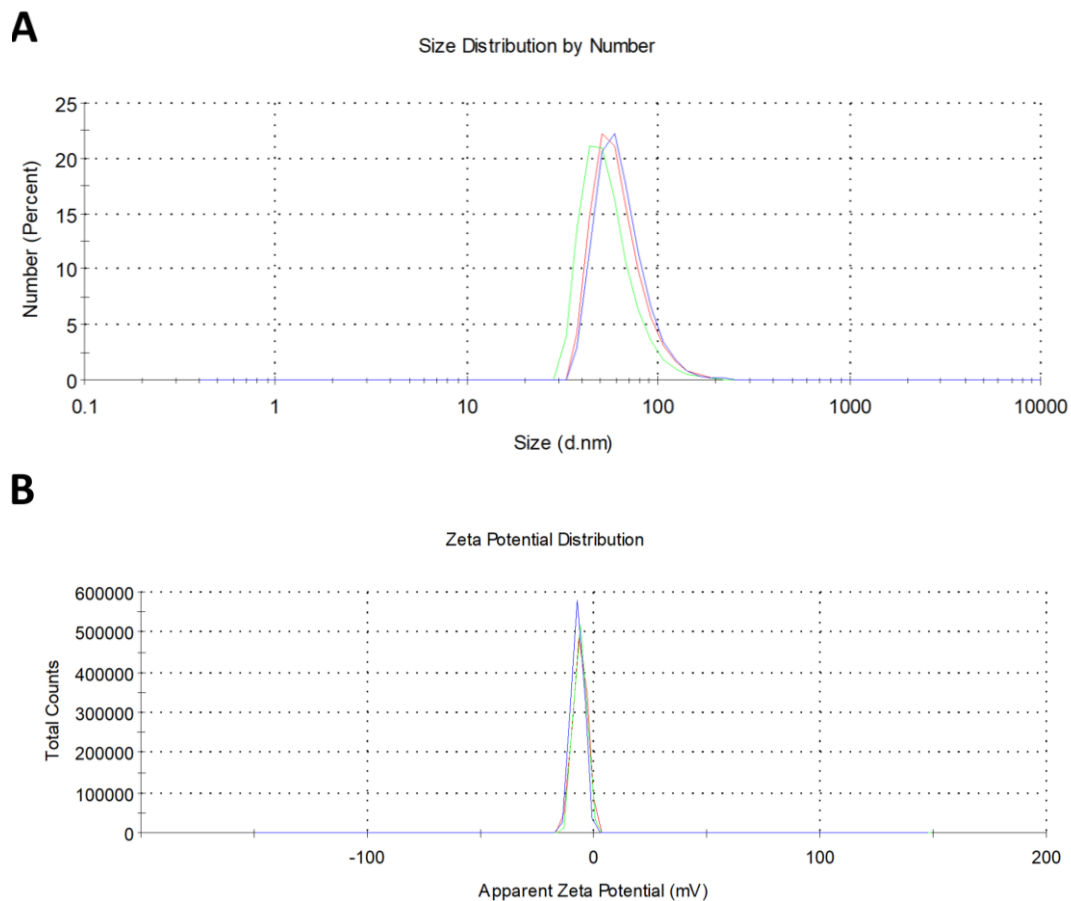


Figure 16. Deep cervical lymph node injection of Evans Blue dye. (A) Control mouse brain and meninges without dye administration. (B) Staining of the meninges and brain parenchyma after the injection of 100 μ L of a 1% solution of Evans Blue dye, in a pattern consistent to the territory of venous sinuses and perivenous region.

4.5.2 Mice intracerebroventricular injection of Chinese ink

Chinese ink has been previously used for staining of lymphatic structures (97–99), which led to its consideration to validate Evans Blue findings with another dye. Chinese ink (Artel) was characterized by DLS, which revealed a mean (\pm SD) size of 61.62 ± 4.84 nm and mean (\pm SD) surface zeta potential of -6.34 ± 0.63 mV (Figure 17A and 17B), and electron microscopy (Figure 17C). The measurements correspond to expected sizes and surface charge values observed by DLS of purified exosomes from the B16F10 melanoma cell line used for this study. Therefore, the administration of Chinese ink prior to the use of the SPION-loaded exosome system can provide valuable information as a model of behavior of exosome-like nanoparticles through the cervical and meningeal lymphatic pathway.



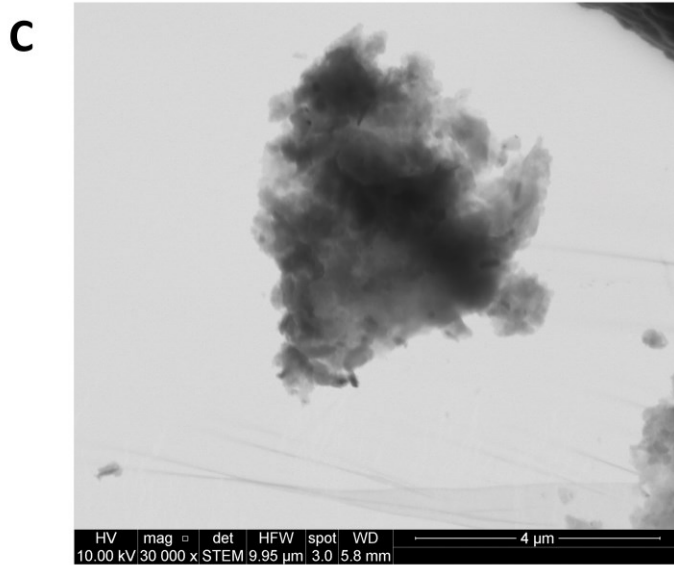


Figure 17. Characterization of Chinese ink. (A) DLS analysis of Chinese ink nanoparticle size distribution. (B) Zeta potential of Chinese ink nanoparticles. (C) Electron microscopy image of Chinese ink.

Post-mortem injections with 10% Chinese ink diluted in distilled water were performed into the cisterna magna of mice (n=3) followed by neck evaluations, replicating de procedures described previously for the Evans Blue assays. Intracerebroventricular injections through the cisterna magna showed staining of deep cervical lymph nodes within the first minute after the administration of Chinese ink in all mice (Figure 18).

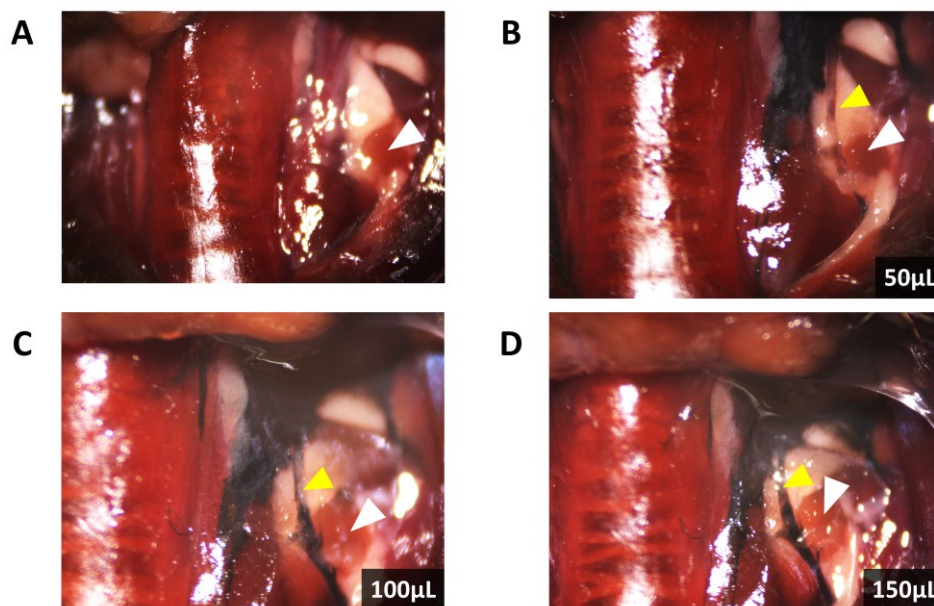


Figure 18. Intracerebroventricular injection of Chinese ink. (A) The left deep cervical lymph node before administration. (B-D) Sequential injections of 50 μ L, 100 μ L, and 150 μ L of 10% Chinese ink into the cisterna magna. White arrowheads indicate the lymph node and yellow arrowheads indicate vessels arising near the internal jugular vein into the deep cervical lymph nodes.

4.5.3 Mice deep cervical lymph node injection with Chinese ink

Post-mortem injections with 10% Chinese ink diluted in distilled water were administered in the deep cervical lymph nodes of mice (n=3) followed by partial craniectomy to evaluate the anatomical possibility of retrograde flow from neck lymphatic structures to the CNS spaces. Procedures for dissection, lymph node exposure and injections, and craniectomy were performed as previously described for the Evans Blue assays. Deep cervical lymph node injections showed staining of reticular vessels in all mice, surrounding the region of the transverse venous sinuses (Figure 19B and 19D), parietal vessels (Figure 19C), and a confined area of parietal brain parenchyma (Figure 19C).

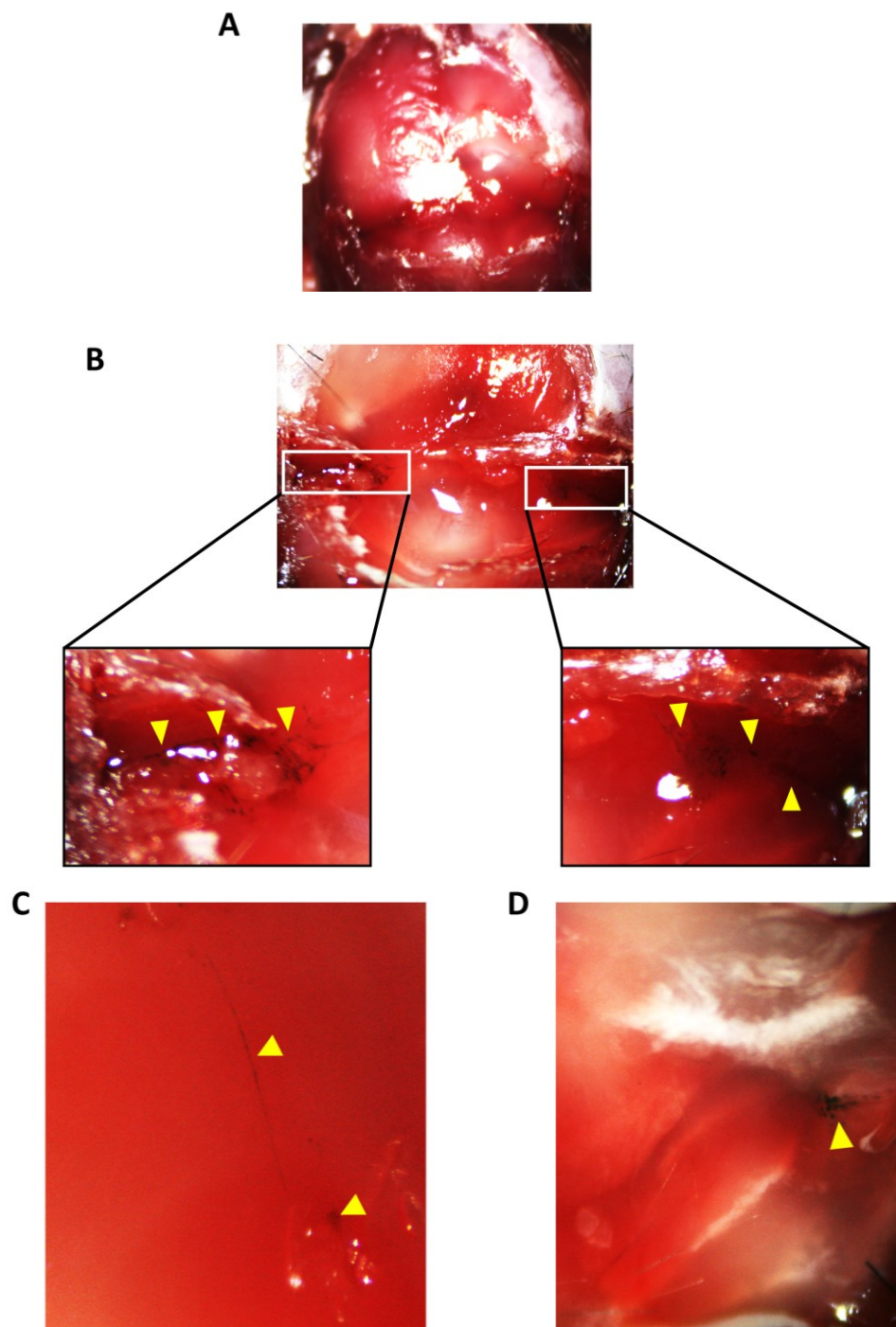


Figure 19. Deep cervical lymph node injection of Chinese ink. (A) shows a control mouse brain and meninges without dye administration. (B) Staining of reticular vessels surrounding the region of the transverse venous sinuses. (C) Stained parietal vessels and a confined area of parietal brain parenchyma. (D) Staining of the meninges in the region of the right transverse venous sinus.

4.6 Specific objective 2c

4.6.1 MRI imaging of SPIONs and SPION-loaded exosomes through cervical and meningeal lymphatic vessels

Anterograde pathway: Both SPIONs and SPION-loaded exosomes showed hypointense signals of cervical lymphatic structures after intracerebroventricular injections through the cisterna magna in the T2w and T2* MRI images (Figure 20). *Retrograde pathway:* Both SPIONs and SPION-loaded exosomes revealed hypointense signals in the brain ventricles and parenchyma in MRI T2w images and T2* maps (Figure 21). Hypointense signals were also detected at the level of the neck where the injections were administered. These results show that the cervical and meningeal lymphatic system can transport SPIONs and SPION-labeled exosomes both towards the thorax and in the direction of the brain.

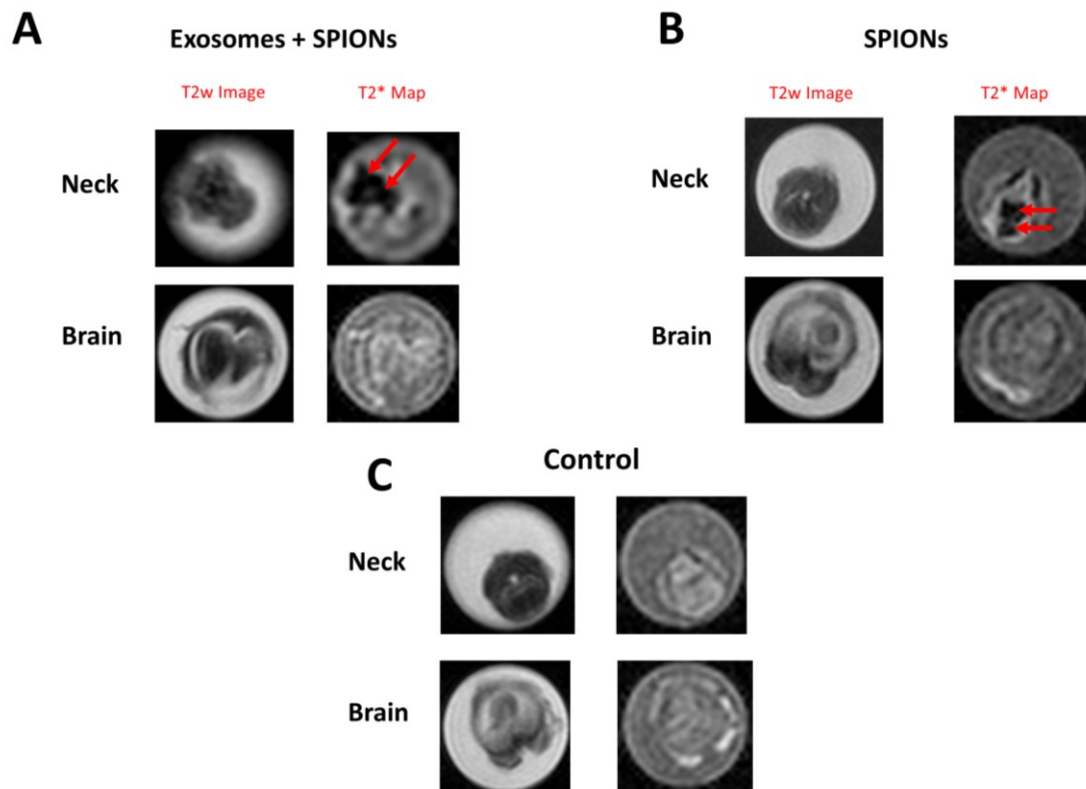


Figure 20. MRI analysis of the anterograde flow of SPIONs and SPION-labeled exosomes through the cervical and meningeal lymphatic system. (A and B) Neck images show the detection of nanoparticles at this region 30 min after the injection at the cisterna magna (n=3). (C) These two conditions were compared to control mice with no injected solutions (n=3).

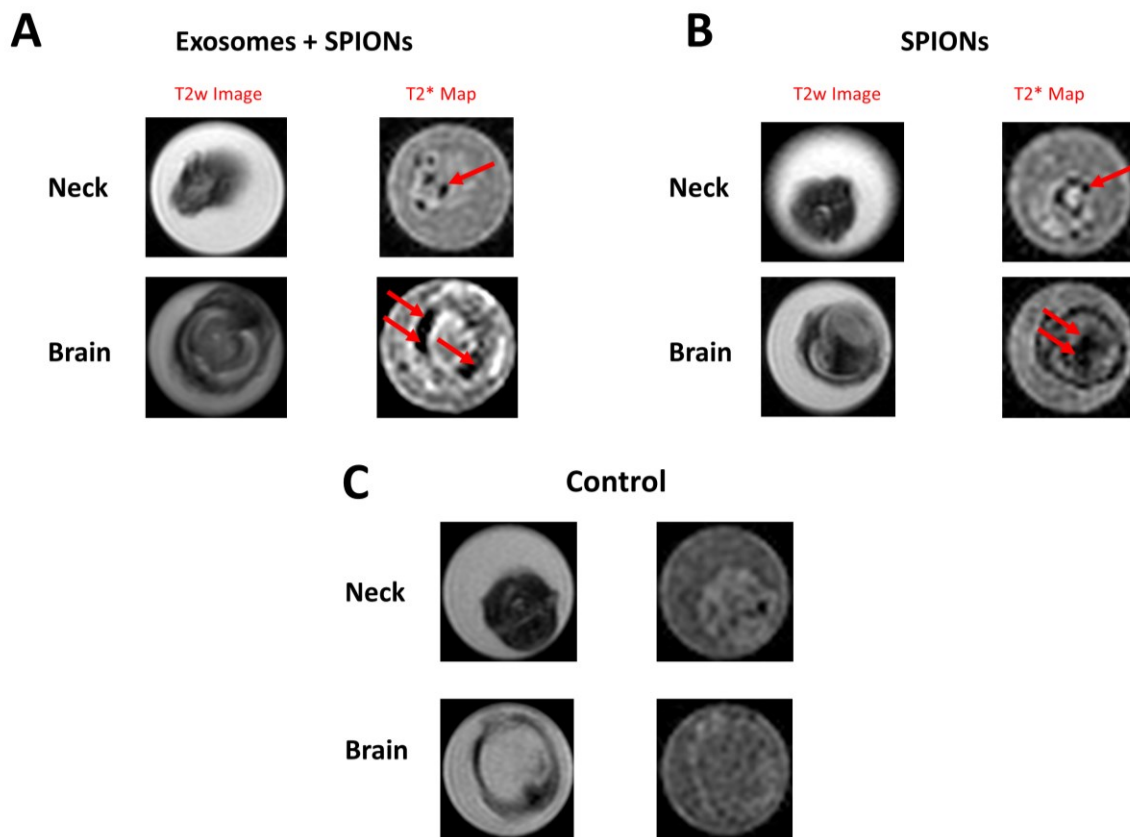


Figure 21. MRI analysis of the retrograde flow of SPIONs and SPION-labeled exosomes through the cervical and meningeal lymphatic system. (A and B) Brain images show the detection of nanoparticles at this region 30 min after the injection at the deep cervical lymph node (n=3). (C) These two conditions were compared to control mice with no injected solutions (n=3).

4.7 Specific objective 3 and histological analysis of retrograde and anterograde flow through the cervical and meningeal lymphatic system.

Histological analyses were performed on SPIONs and loaded exosomes by the Prussian Blue technique. Complementary analyses with gold nanoparticles and Chinese ink by *post-mortem* and *in vivo* injections into the cisterna magna and the deep cervical lymph nodes were also performed through the Gold Enhancement method. A brief description of the gold nanoparticles used follows before histological results. Chinese ink, SPIONs, and exosomes have been previously described.

4.7.1 Gold nanoparticles characterization

Gold nanoparticles with a mean size of 49.1 ± 0.9 nm and mean Z potential of 45 ± 8 mV were measured by DLS and NTA (Figure 22A). Nanorod morphology can be observed in the STEM image seen in Figure 22B.

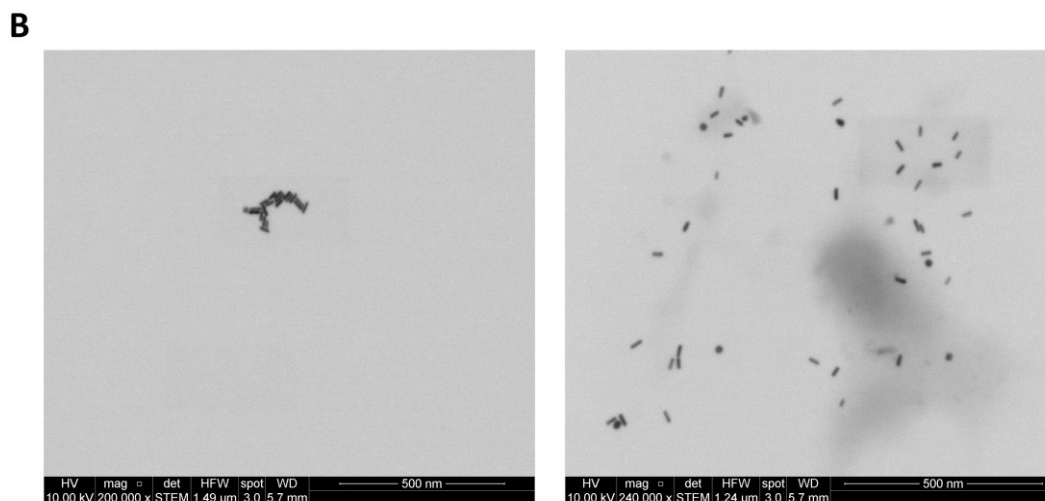
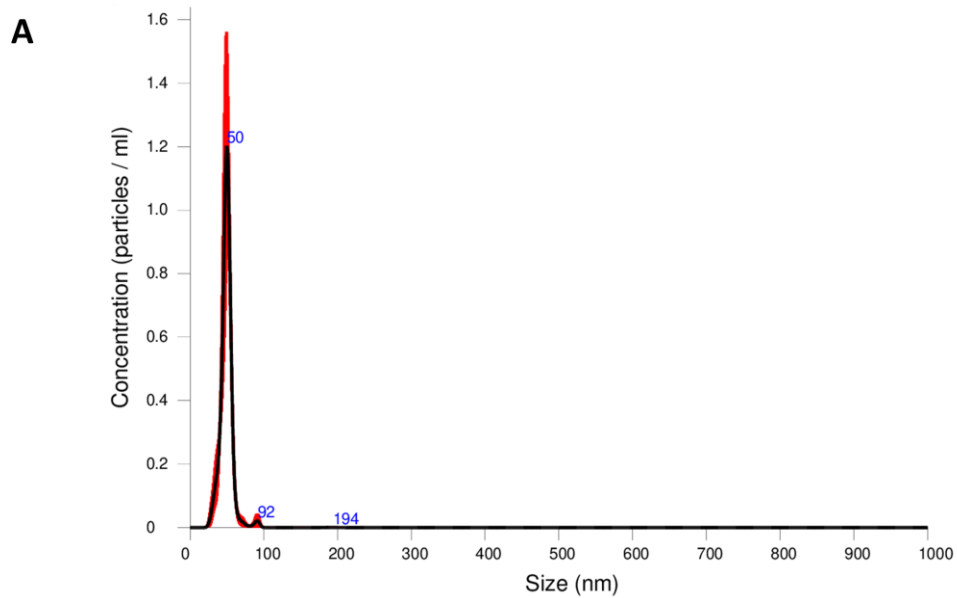


Figure 22. Gold nanoparticle characterization. (A) Nanoparticle size distribution measured by NTA. (B) Nanorod morphology of gold nanoparticles seen through electron microscopy.

4.7.2 Normal brain anatomy of controls

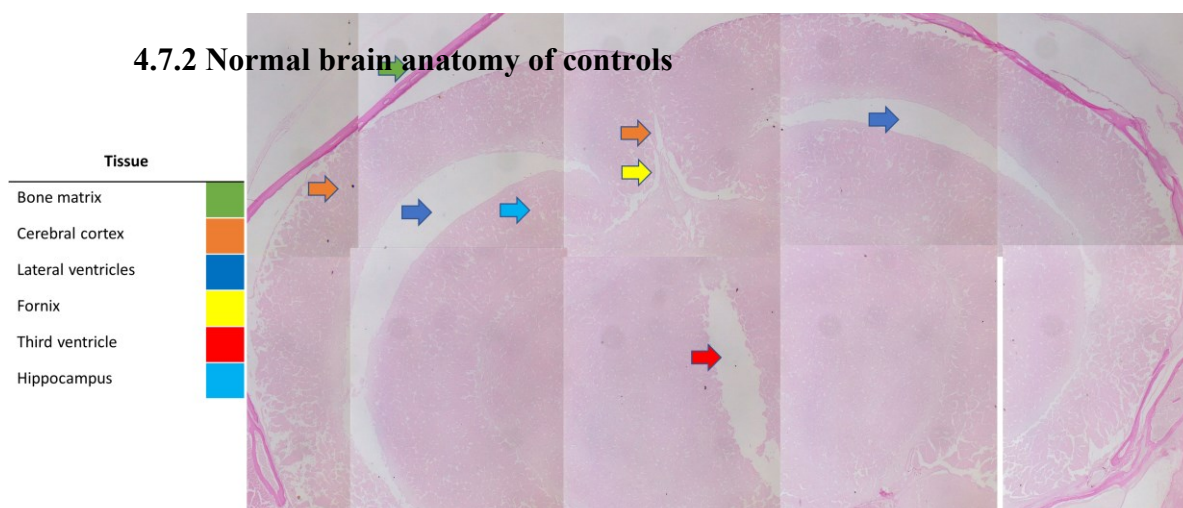


Figure 23. Normal mouse brain anatomy.

For reference, normal anatomy as seen in controls with Milli-Q water, PBS, distilled water, and controls without injection is shown in Figure 23.

4.7.3 Retrograde flow evaluation of gold nanoparticles *post-mortem*

Retrograde flow in *post-mortem* procedures (n=3) of gold nanoparticles after deep cervical lymph node administration was confirmed by the detection of Gold Enhancement staining at different CNS regions in all mice. These included the olfactory bulb (Figure 24A), the brain parenchyma (Figure 24B), and within the meningeal lymphatic vessels (Figure 24C). No staining was detected within arterial or venous structures within the head and neck, ruling out other sources of nanoparticle distribution to the brain in *post-mortem* gold nanoparticle assays.

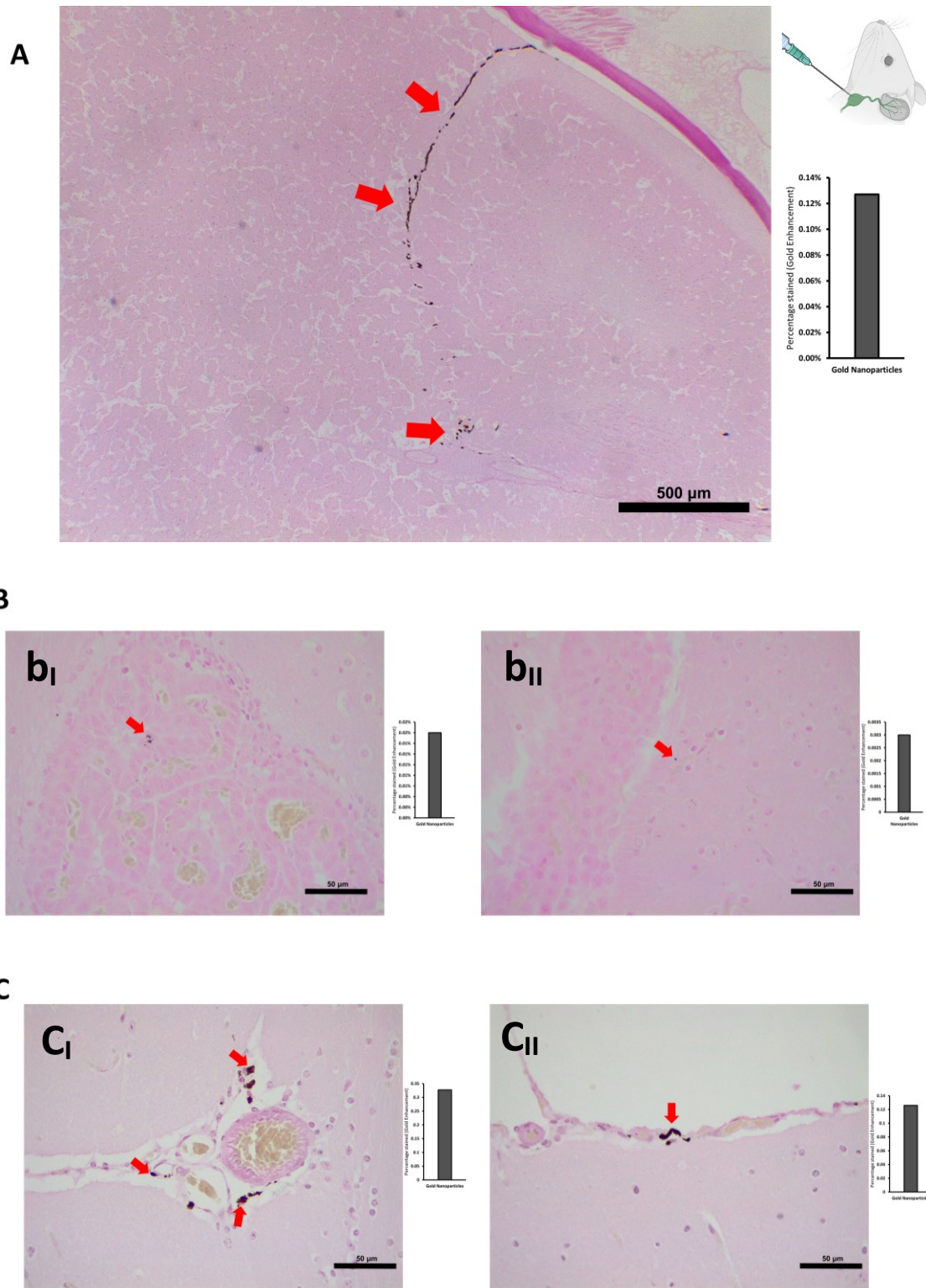


Figure 24. Retrograde flow of gold nanoparticles *post-mortem* using Gold Enhancement technique. (A) Injection of a gold nanoparticle solution at the deep cervical lymph node showed retrograde flow at the olfactory bulb. (B) Detection of Gold Enhancement staining at the mouse brain parenchyma. (C) Detection of Gold Enhancement staining at meningeal lymphatic vessels.

4.7.4 Retrograde flow evaluation of Chinese ink *post-mortem*

Retrograde flow in *post-mortem* procedures (n=3) was confirmed in all mice after deep cervical lymph node administration of 10% Chinese ink. Staining was detected within the meningeal lymphatic vessels (Figure 25A), the third ventricle (Figure 25B), and different cortical regions (Figure 25C). No staining was detected within arterial or venous structures within the head and neck, ruling out other sources of nanoparticle distribution to the brain in *post-mortem* Chinese ink assays.

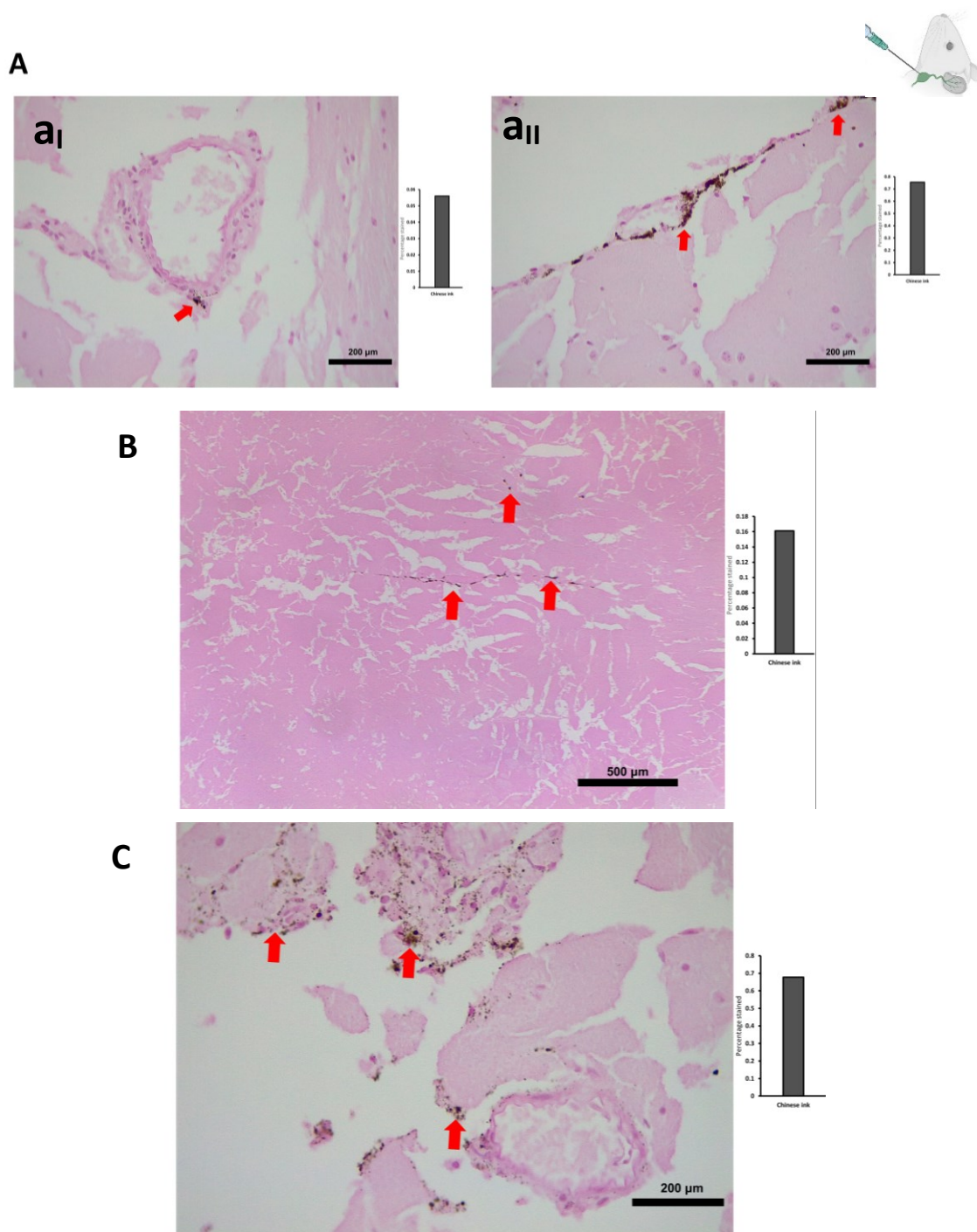
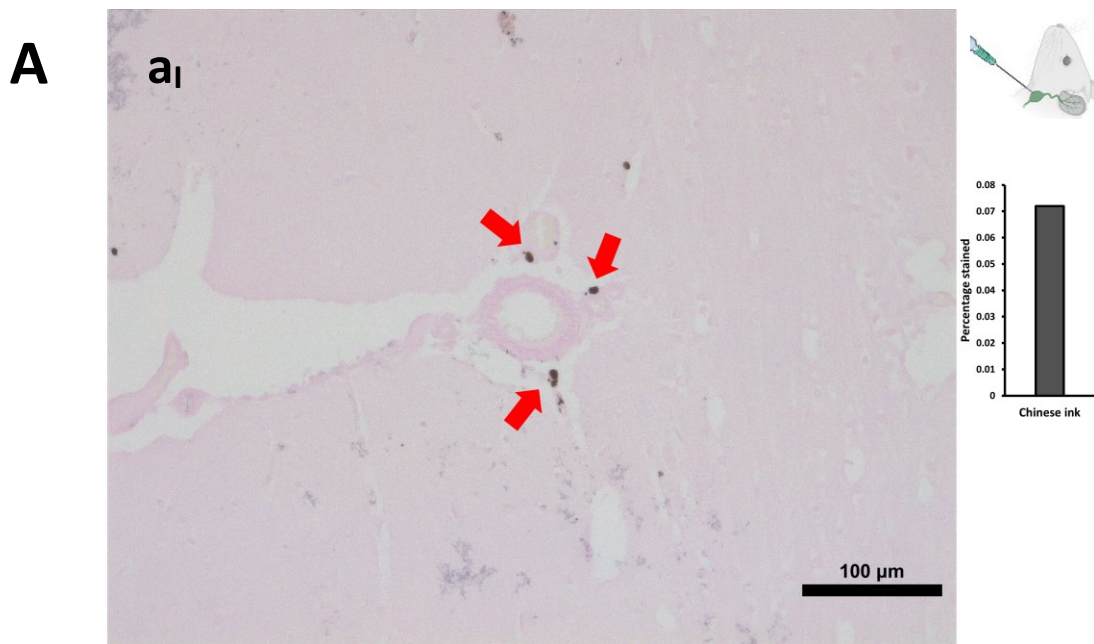
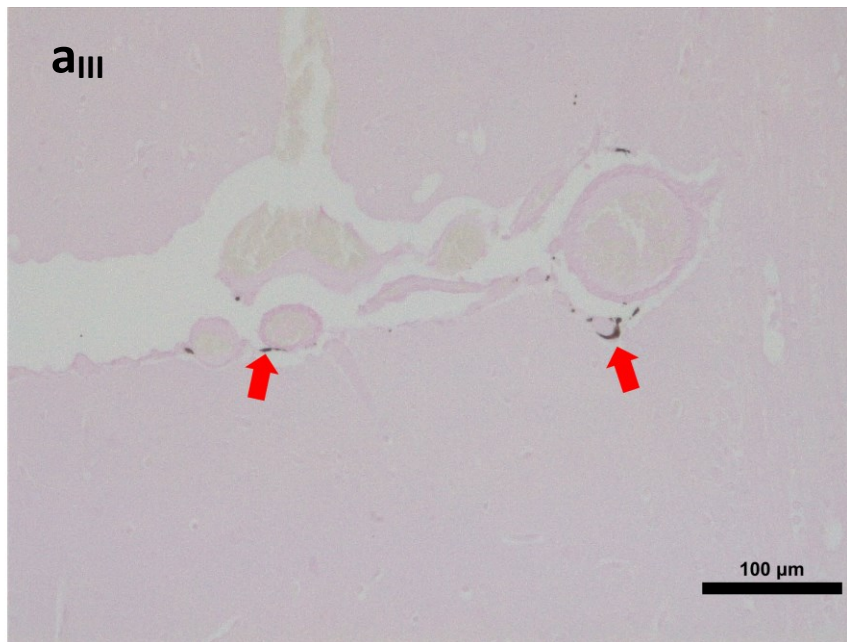
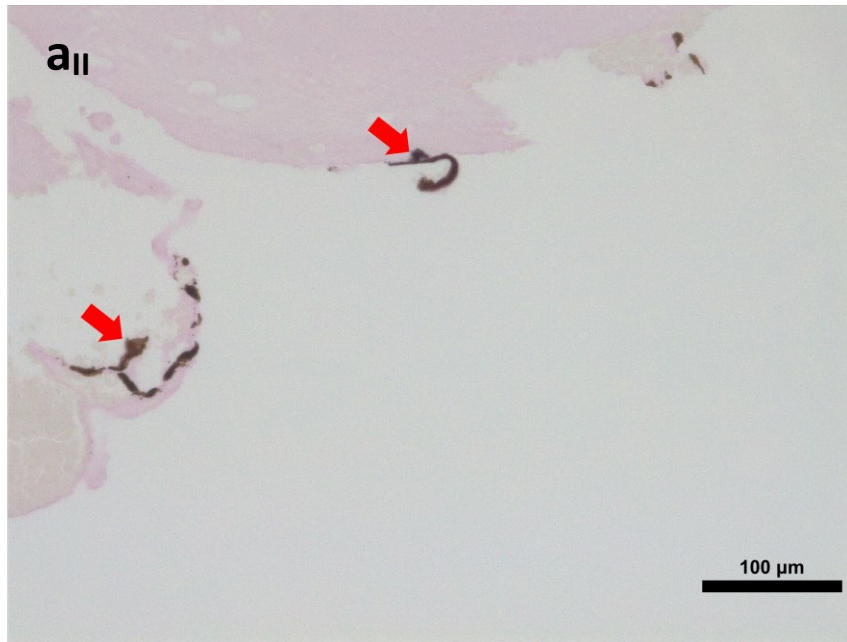


Figure 25. Retrograde flow of Chinese ink nanoparticles *post-mortem*. (A) Injection of a 10% Chinese ink solution at the deep cervical lymph node showed retrograde flow at meningeal lymphatic vessels. (B) Detection of staining at the third ventricle wall. (C) Nanoparticle identification at the brain parenchyma.

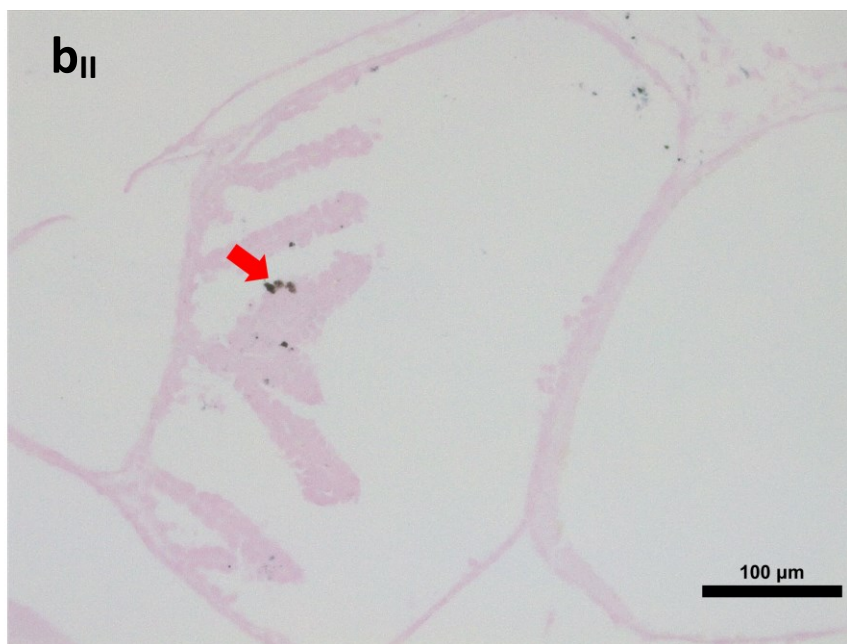
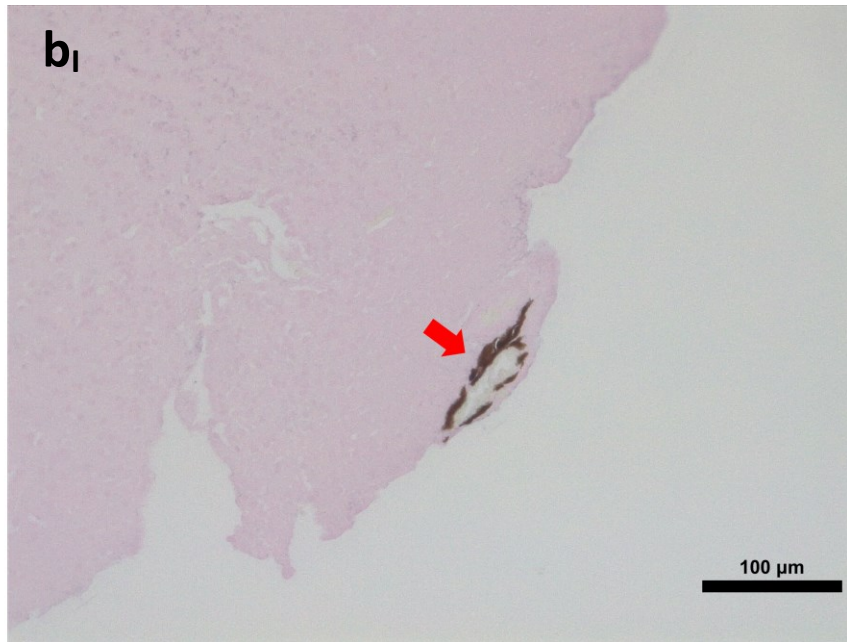
4.7.5 Retrograde flow evaluation of Chinese ink *in vivo*

Retrograde flow of *in vivo* procedures (n=3) was confirmed in all mice after deep cervical lymph node administration of a 10 μ L solution of 10% Chinese ink. Staining was detected within the meningeal lymphatic vessels (Figure 26A) and cortical regions (Figure 26B). No staining was detected within arterial or venous structures within the head and neck of two out of three mice. One mouse presented staining within the jugular vein but not the carotid artery (Figure 27), which also indicates that the observed nanoparticles at the meningeal lymphatic vessels and the brain parenchyma originate mainly from the lymphatic system distribution and not through arterial recirculation of cardiac and other thoracic vessels.





B



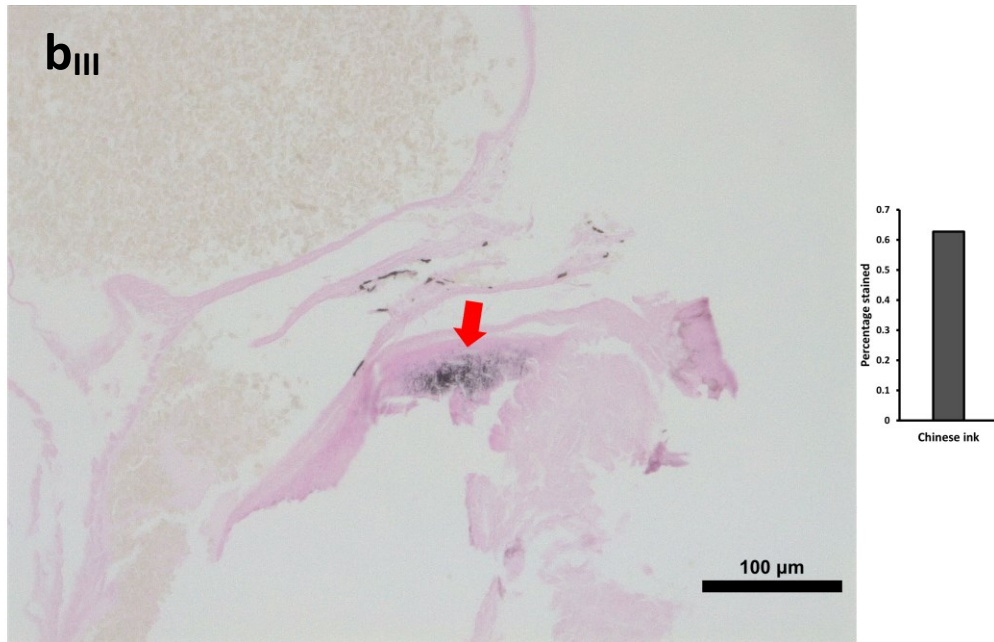


Figure 26. Retrograde flow of Chinese ink nanoparticles in vivo. (A) Injection of 10μL of a 10% Chinese ink solution at the deep cervical lymph node showed retrograde flow at meningeal lymphatic vessels. (B) Chinese ink nanoparticles were detected at the brain parenchyma.

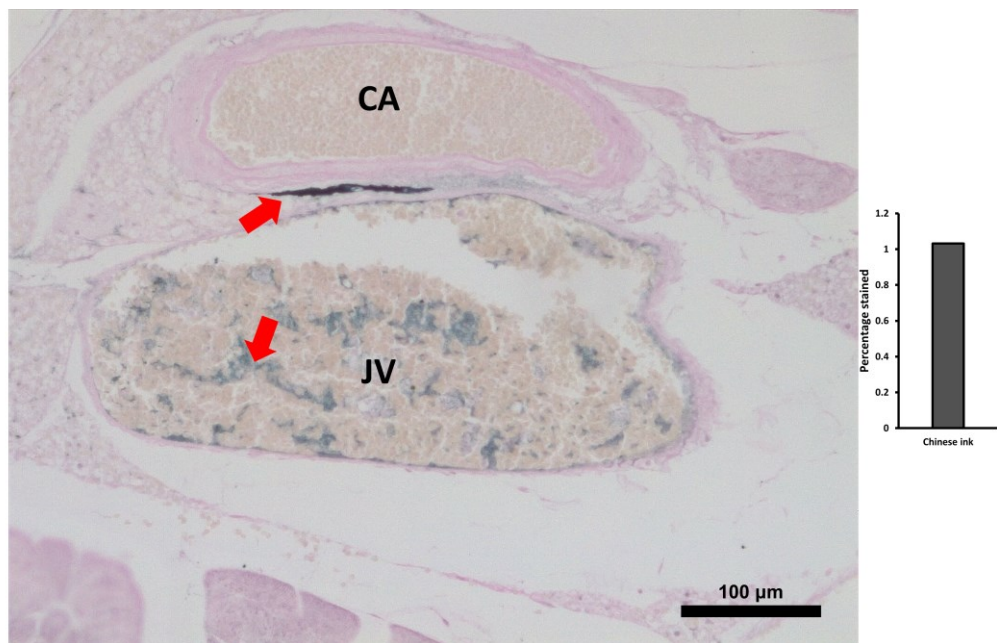
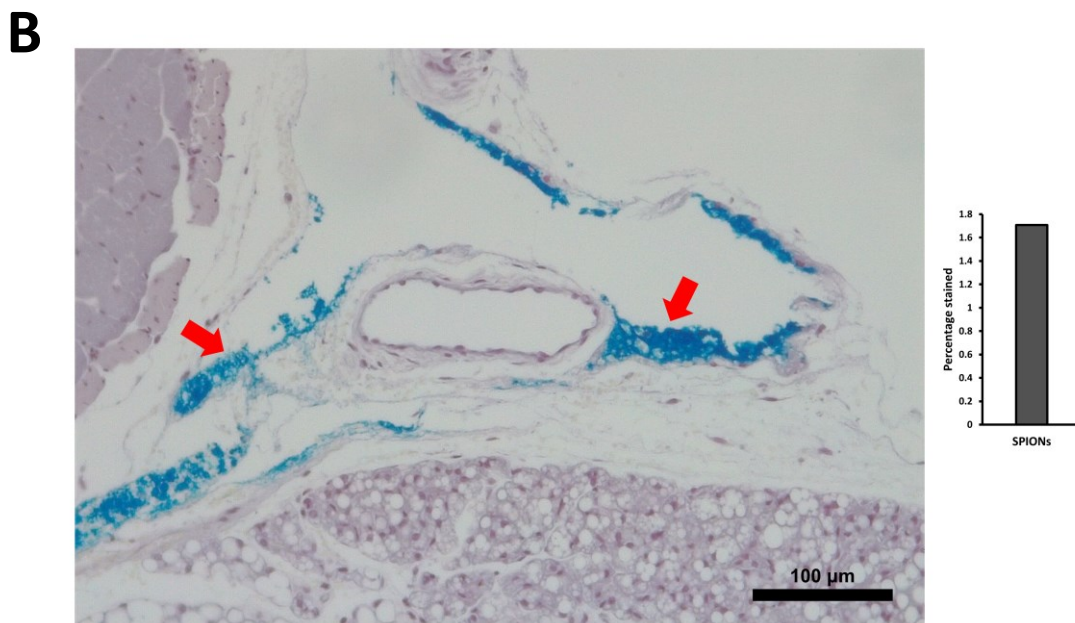
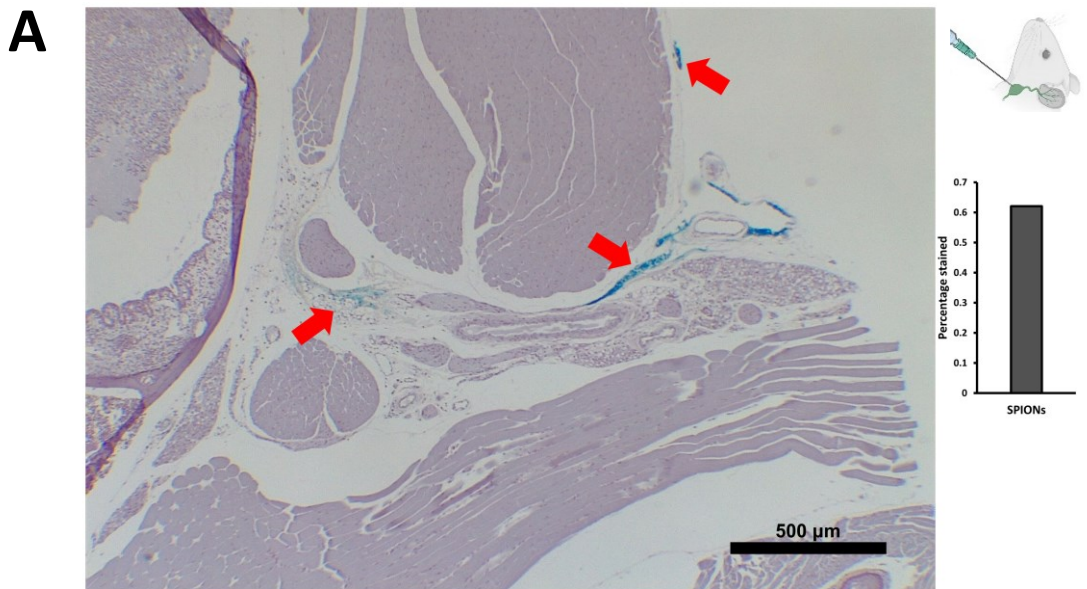


Figure 27. Carotid artery and jugular vein of a mouse injected with Chinese ink nanoparticles at the deep cervical lymph node in vivo. Two out of three mice did not stain arterial or venous structures. One presented with Chinese ink in the jugular vein and connective tissue. Red arrows show Chinese ink nanoparticles. CA: Carotid artery; JV: jugular vein.

4.7.6 Retrograde flow evaluation of SPIONs and SPION-loaded exosomes *in vivo*

Retrograde flow of SPIONs injected into the deep cervical lymph node *in vivo* was observed in staining of neck lymphatic vessels anatomically located towards the head and meningeal lymphatic vessels, in all mice (n=3) (Figure 28 A-C). However, no staining was observed within the brain parenchyma with the Perls' Prussian Blue technique. No staining was detected within arterial or venous structures within the head and neck. Exosomes loaded with SPIONs did not stain in both the anterograde and retrograde evaluations, as expected for unexposed iron nanoparticles within exosome membranes.



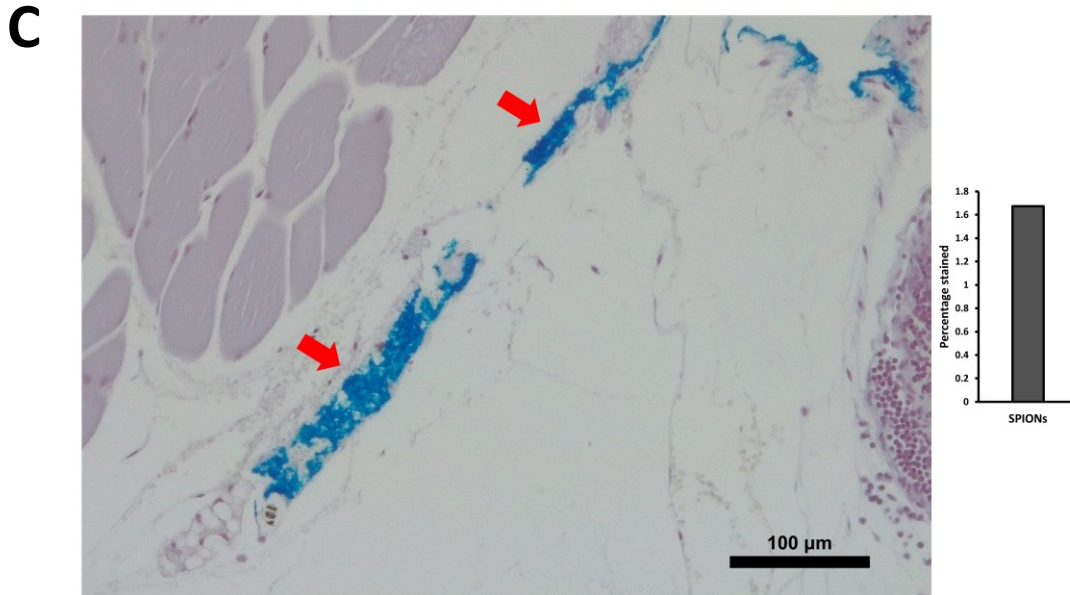


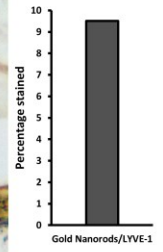
Figure 28. Retrograde flow evaluation of SPIONs *in vivo* using Perls' Prussian Blue. (A-C) Injection of 10 μ L of a SPION solution at the deep cervical lymph node showed staining of cervical and meningeal lymphatic vessels.

4.7.7 Immunohistochemistry evaluation of nanoparticles and the lymphatic marker LYVE-1 in the retrograde flow analysis

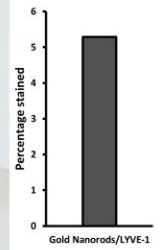
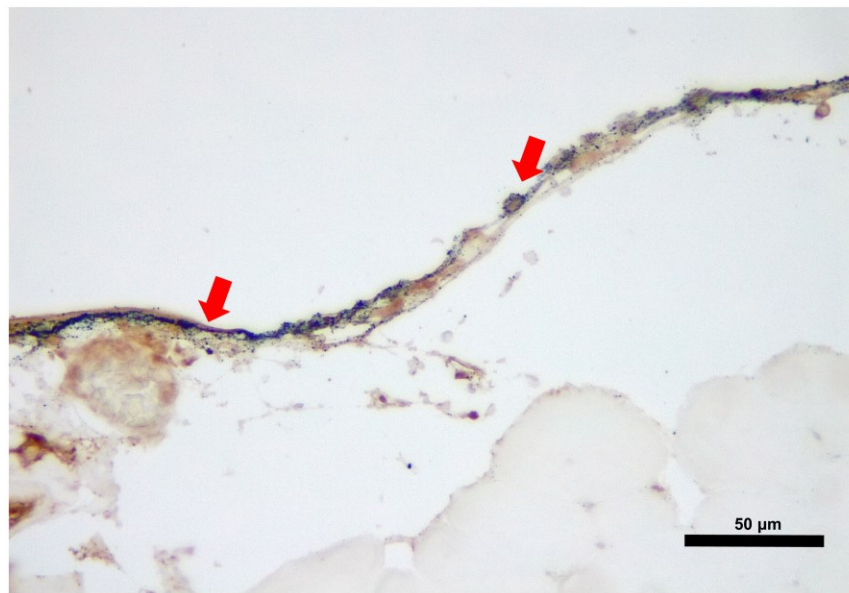
4.7.7.1 Gold nanoparticles and LYVE-1 *in vivo*

Anti-LYVE-1 immunohistochemistry successfully stained the cervical and meningeal lymphatic vessels. Gold Enhancement revealed gold nanoparticles travelling only within the cervical (Figure 29 A-D) and meningeal lymphatic vessels (Figure 30 A and B) in the *in vivo* retrograde flow experiments performed on all C57BL/6 mice (n=3). Gold nanoparticles reached the brain parenchyma (Figure 30B) through the retrograde flow from the cervical lymphatic vessels. No staining was detected within arterial or venous structures within the head and neck, ruling out other sources of nanoparticle distribution to the brain in *in vivo* gold nanoparticle assays.

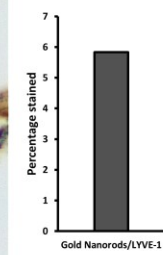
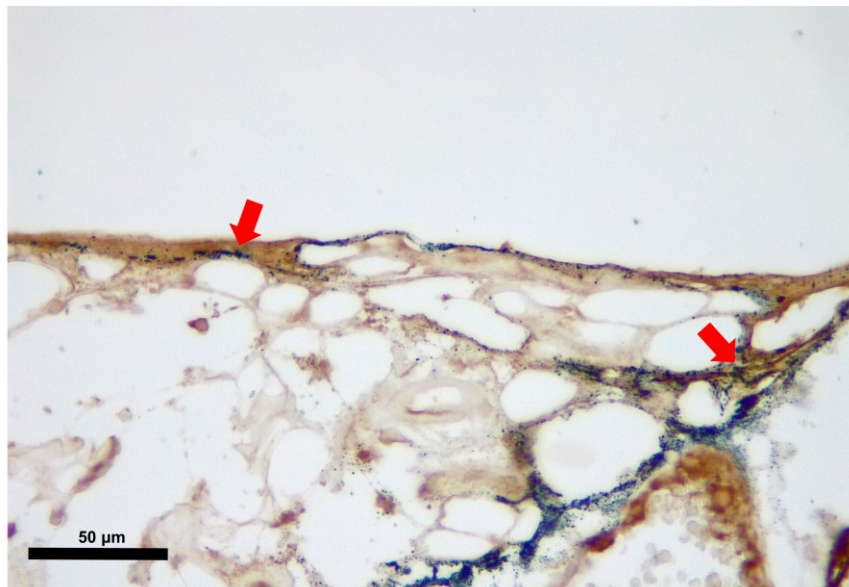
A



B



C



D

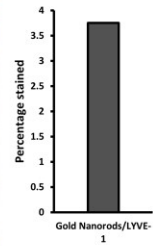
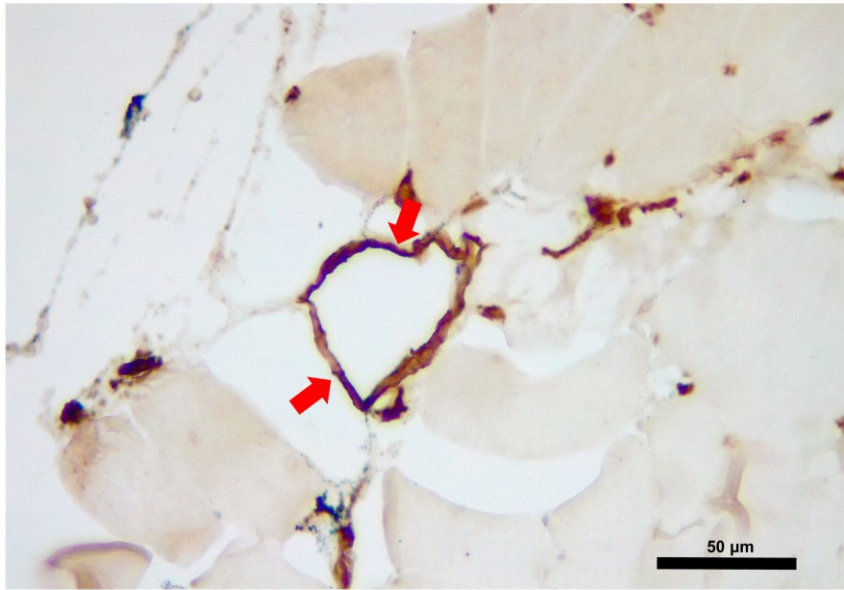


Figure 29. Gold nanoparticles and LYVE-1 immunohistochemistry of cervical lymphatic vessels. (A-D) Red arrows show gold nanoparticles within the cervical lymphatic vessels identified after *in vivo* retrograde flow experiments.

A

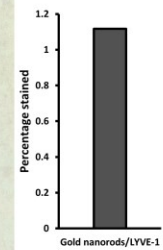
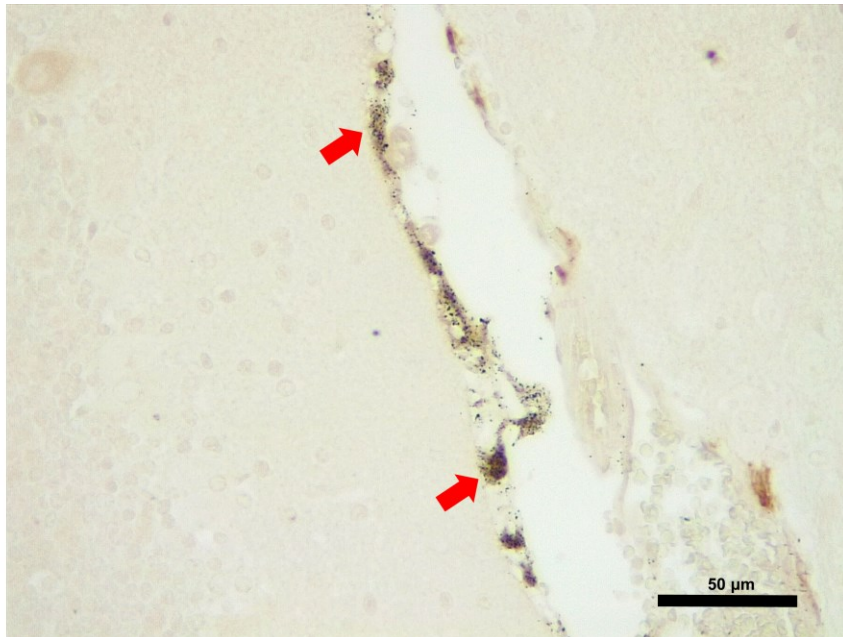




Figure 30. Gold nanoparticles and LYVE-1 immunohistochemistry. (A) Meningeal lymphatic vessel stained with anti-LYVE-1 colocalizing with gold nanoparticles stained with Gold Enhancement. (B) Gold nanoparticles colocalizing with the meningeal lymphatic vessel (red arrows). Gold nanoparticles are also identified within the brain parenchyma (yellow arrows).

4.7.7.2 Chinese ink nanoparticles and LYVE-1 *in vivo*

Anti-LYVE-1 immunohistochemistry successfully stained the cervical and meningeal lymphatic vessels. Chinese ink staining revealed nanoparticles within the cervical (Figure 31 A and B) and meningeal lymphatic vessels (Figure 32 A-C) in the *in vivo* retrograde flow experiments performed on all C57BL/6 mice (n=3). As described for Chinese ink without anti-Lyve-1, nanoparticles reached the brain parenchyma (Figure 32C) through the retrograde flow from the cervical lymphatic vessels. Figure 31B shows the injection site at the deep cervical lymph node, associated with a lymphatic vessel positive for LYVE-1, where Chinese ink nanoparticles are colocalizing. No staining was detected within arterial or venous structures within the head and neck of two out of three mice. As previously described with the assay not stained for LYVE-1, one mouse showed jugular vein marks, sparing the carotid artery.

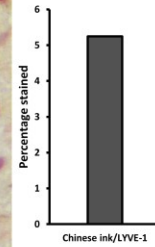
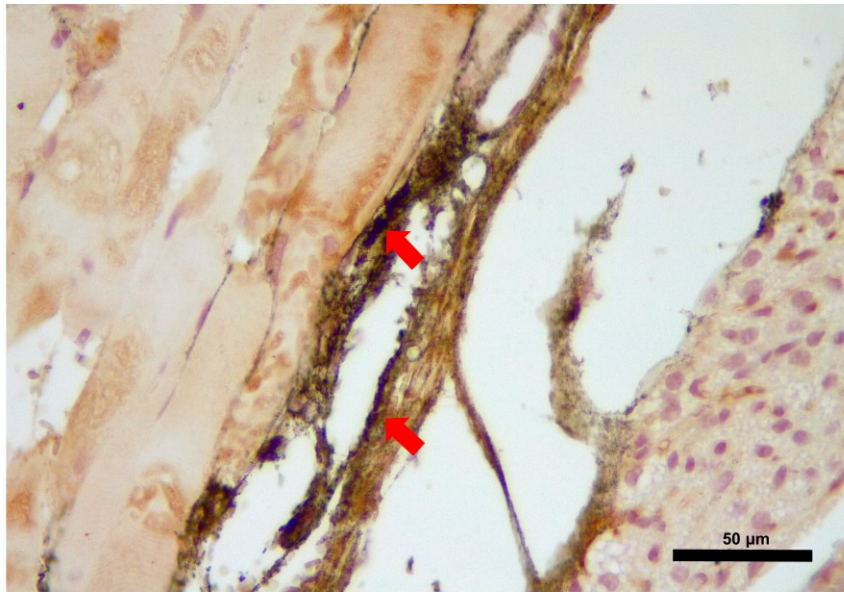
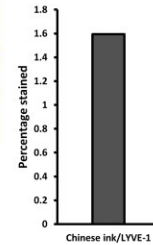
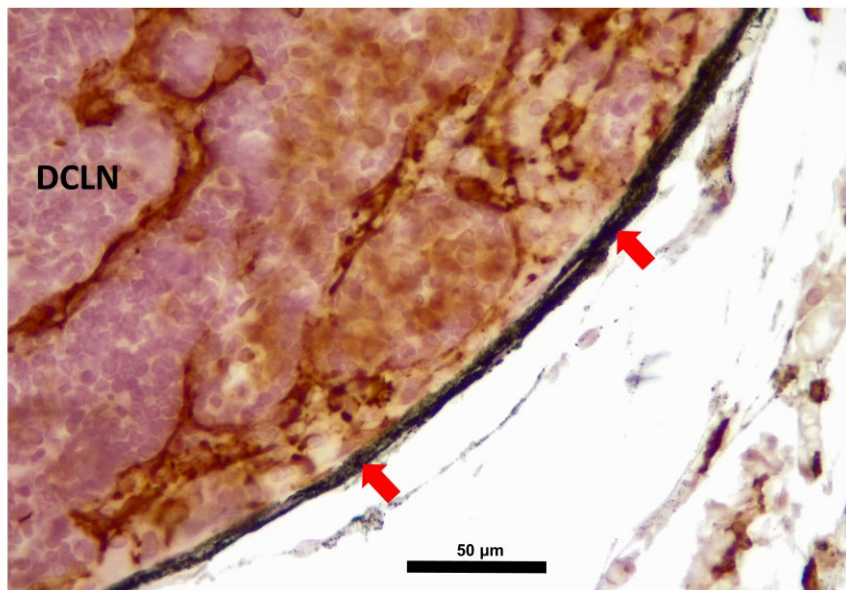
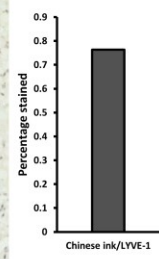
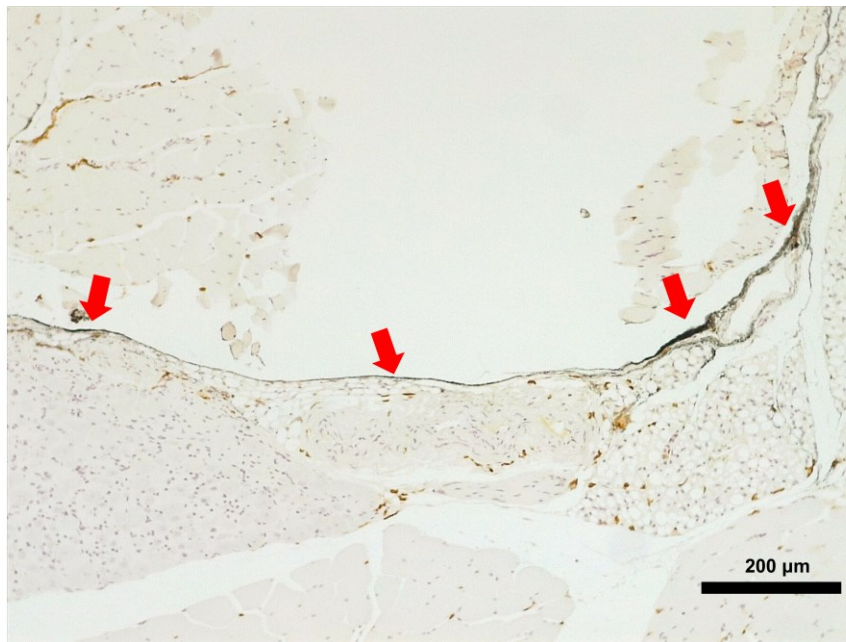
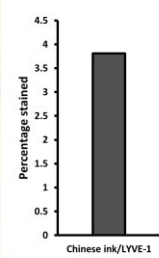
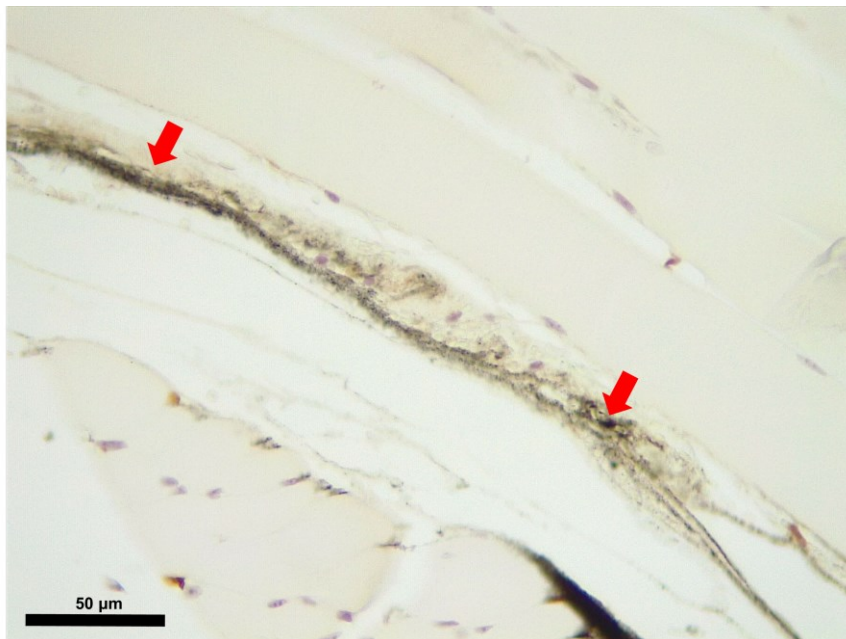
A**B**

Figure 31. Chinese ink and LYVE-1 immunohistochemistry. (A) Red arrows show Chinese ink nanoparticles within the cervical lymphatic vessels identified after *in vivo* retrograde flow experiments. (B) Injection site at the deep cervical lymph node with associated cervical lymphatic vessel stained with anti-LYVE-1 and colocalizing with Chinese ink nanoparticles (red arrows). DCLN: deep cervical lymph node

A



B



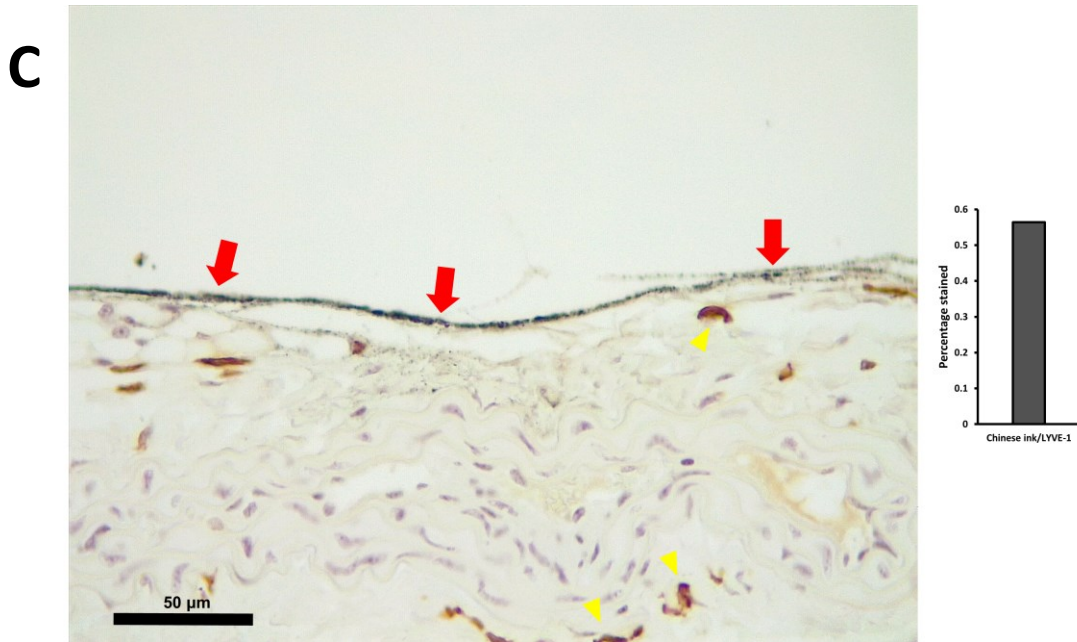


Figure 32. Chinese ink and LYVE-1 immunohistochemistry. (A-B) Meningeal lymphatic vessel stained with anti-LYVE-1 colocalizing with Chinese ink nanoparticles. (C) Chinese ink colocalizing with the meningeal lymphatic vessel (red arrows). Chinese ink nanoparticles are also identified within the brain parenchyma (yellow arrows).

4.7.7.3 SPIONs and LYVE-1 *in vivo*

Anti-LYVE-1 immunohistochemistry successfully stained the cervical and meningeal lymphatic vessels. Perls' Prussian Blue revealed nanoparticles within the cervical lymphatic vessels towards the meningeal lymphatic vessels in the *in vivo* retrograde flow experiments performed on all C57BL/6 mice (n=3) (Figure 33 A and B). Colocalization of both anti-LYVE-1 and Perls' Prussian Blue produced a green color at the immunochemistry slides. Figure 33B shows the injection site at the deep cervical lymph node, associated with a lymphatic vessel positive for LYVE-1, where SPIONs are colocalizing. No staining was detected within arterial or venous structures within the head and neck.

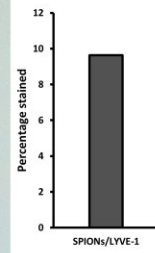
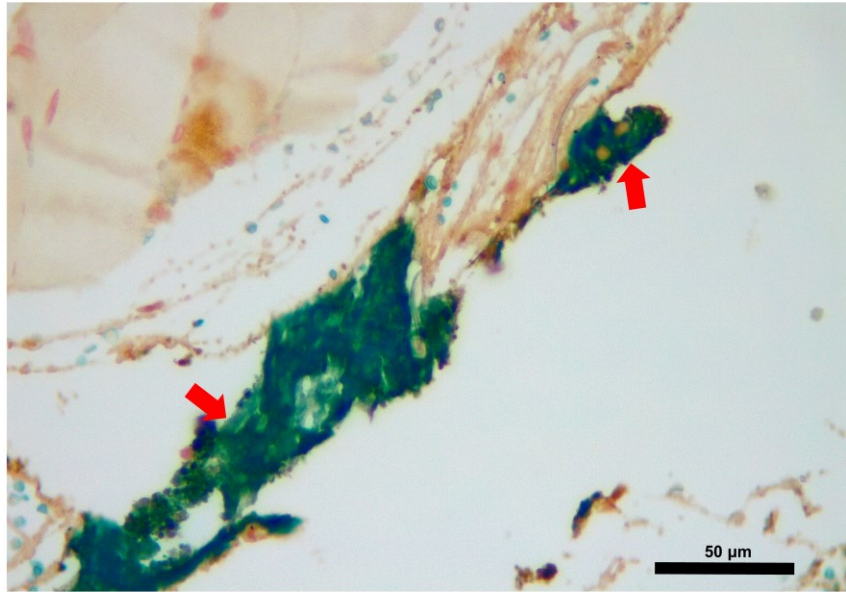
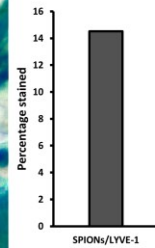
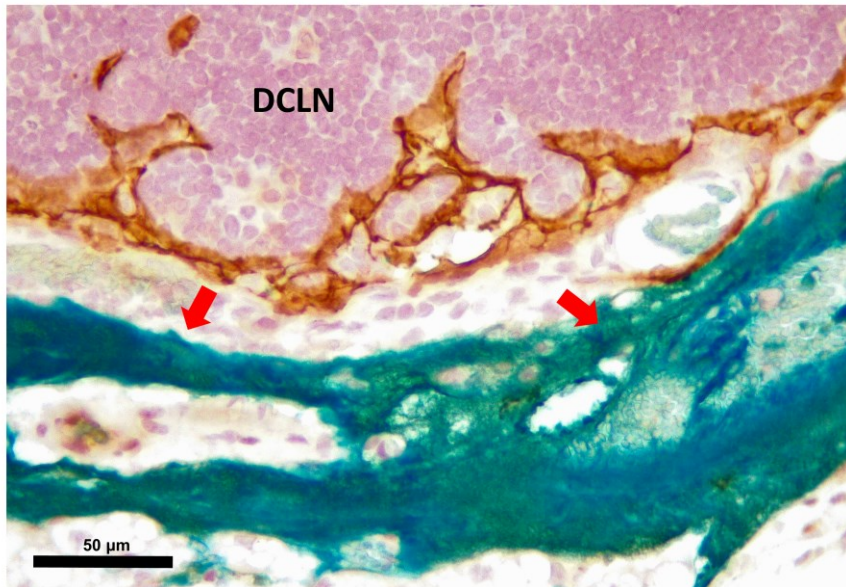
A**B**

Figure 33. SPIONs and LYVE-1 immunohistochemistry. (A) SPIONs within the cervical lymphatic vessels identified after *in vivo* retrograde flow experiments. (B) Injection site at the deep cervical lymph node with associated cervical lymphatic vessel stained with anti-LYVE-1 and colocalizing with SPIONs. DCLN: deep cervical lymph node.

4.7.8 Anterograde flow evaluation of gold nanoparticles *post-mortem*

Anterograde flow in *post-mortem* procedures (n=3) of gold nanoparticles after administration into the cisterna magna was confirmed by the detection of Gold Enhancement staining in cervical lymphatic vessels in all mice, as well as in connective tissue of the neck (Figure 34A). Gold nanoparticles were also identified in the cervical spinal cord as well as its surrounding subdural space and associated peripheral nerves (Figure 34A). At the level of the head, the injection into the cisterna magna also showed staining within lateral ventricles (Figure 35A), the third ventricle (Figure 35B), the olfactory bulb (Figure 35C), and the optic chiasm (Figure 35C) in all mice.

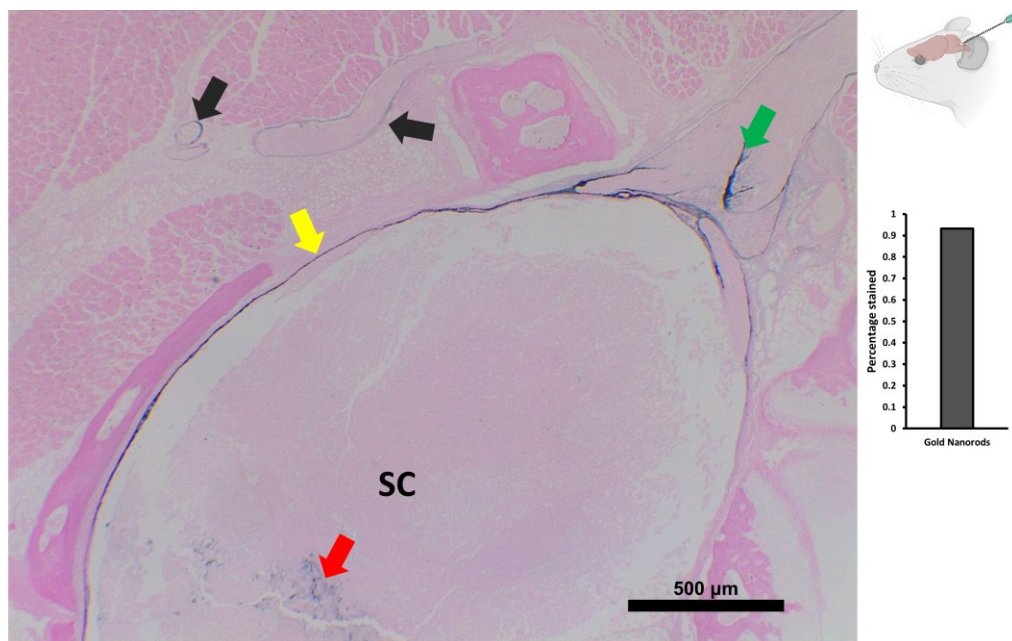
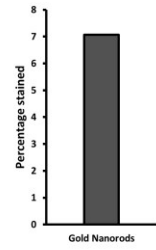
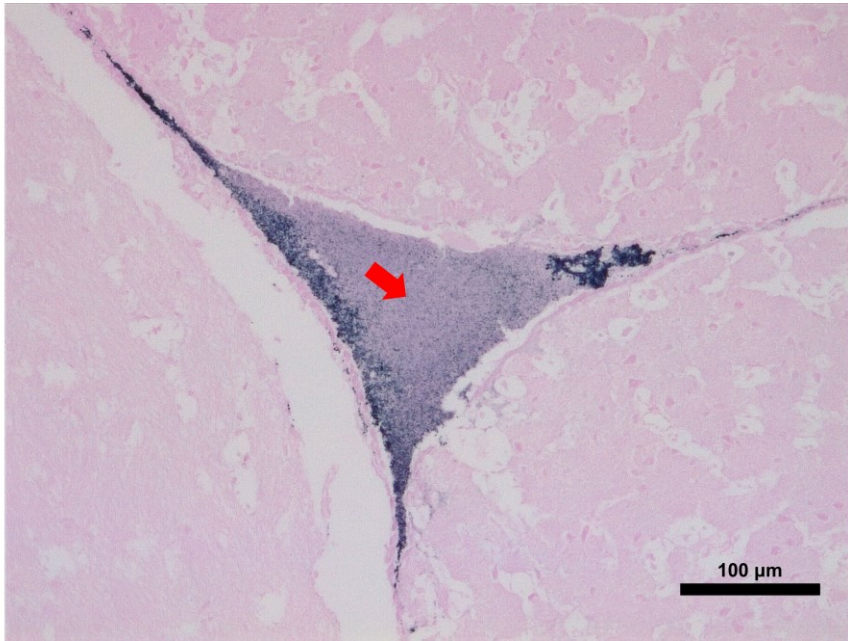


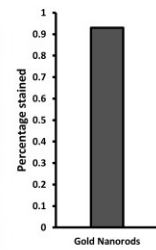
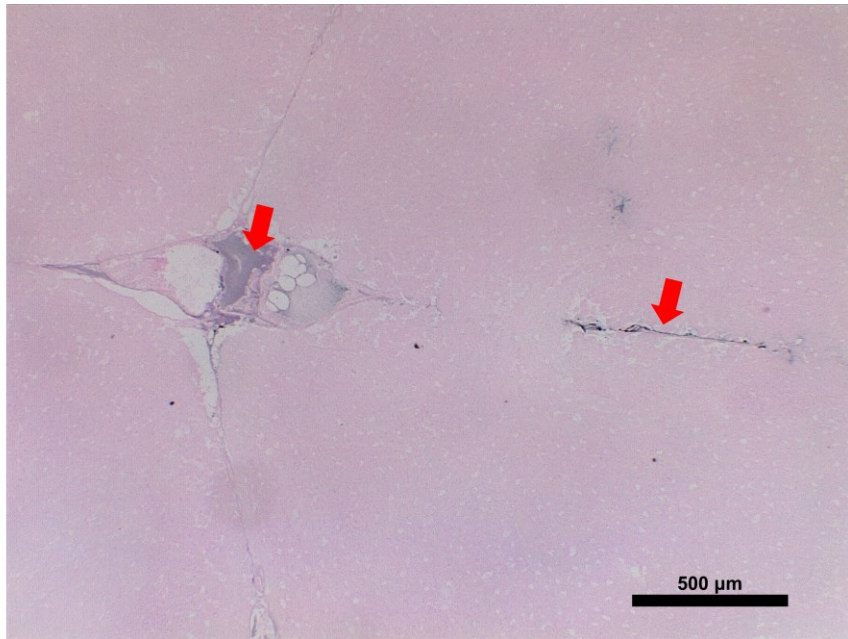
Figure 34. Anterograde flow of gold nanoparticles *post-mortem* using Gold Enhancement technique. Injection of a gold nanoparticle solution at the cisterna magna showed staining of the cervical spinal cord (red arrow), its surrounding subdural space (yellow arrow) and associated peripheral nerves (green arrow). Gold nanoparticles were also detected in cervical lymphatic vessels and connective tissue (black arrows). SC: spinal cord.



A



B



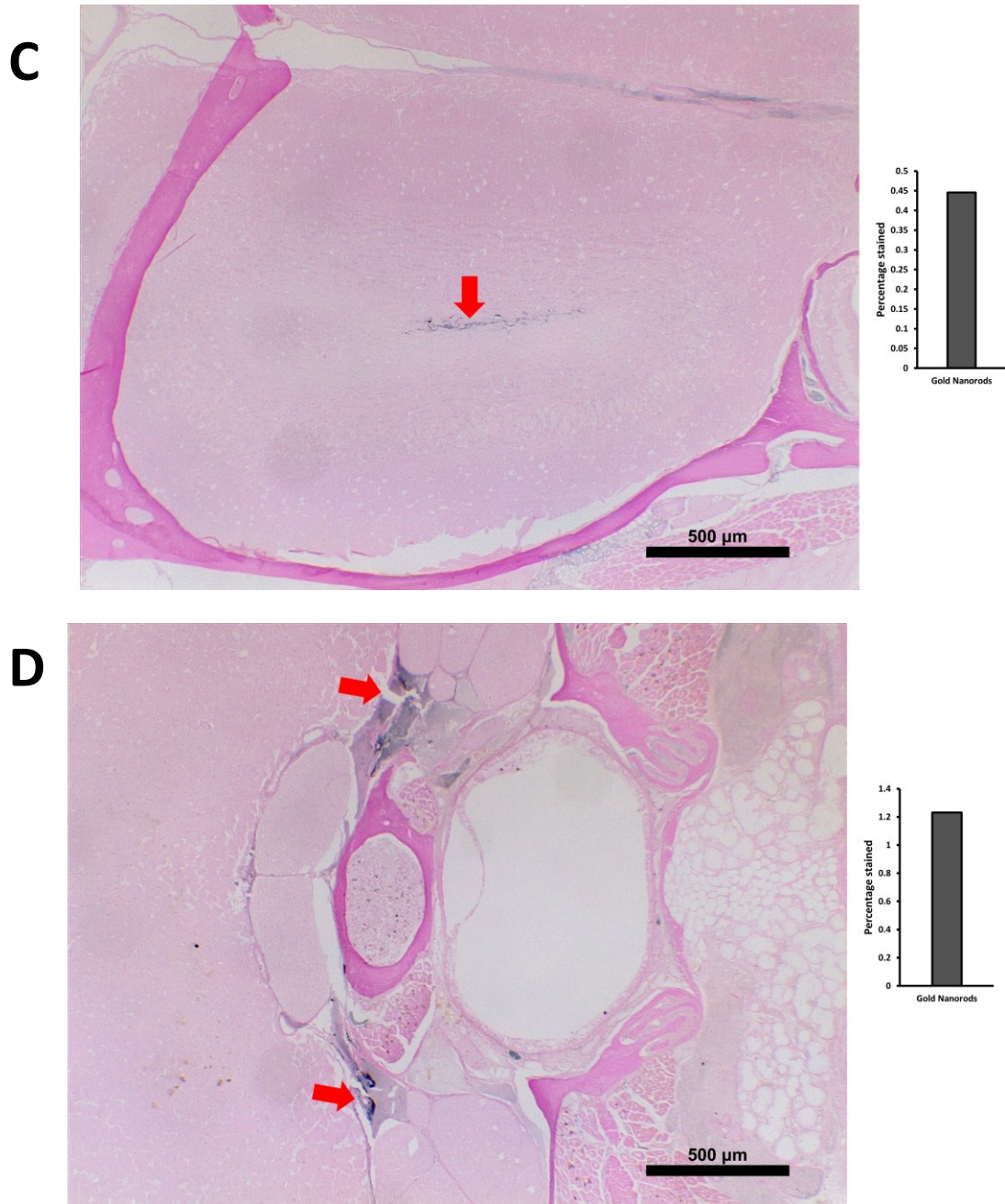


Figure 35. Cephalic structures stained after injection into the cisterna magna of gold nanoparticles. (A) Red arrow shows Gold Enhancement detection of gold nanorods within a lateral ventricle. (B) Staining at the third ventricle and subarachnoid space (red arrows). (C) Detection of gold nanoparticles in the parenchyma of the olfactory bulb (red arrow). (D) Stained optic chiasm (red arrows).

4.7.9 Anterograde flow evaluation of Chinese ink *post-mortem*

Anterograde flow in *post-mortem* procedures (n=3) of Chinese ink nanoparticles after administration into the cisterna magna was confirmed by the detection of staining in cervical lymphatic vessels in all mice, as well as in connective tissue of the neck (Figure 36A). Chinese ink nanoparticles were also identified in the cervical spinal cord as well as its surrounding subdural space (Figure 36B). At the level of the head, the injection into the cisterna magna also showed staining within lateral ventricles (Figure 37).

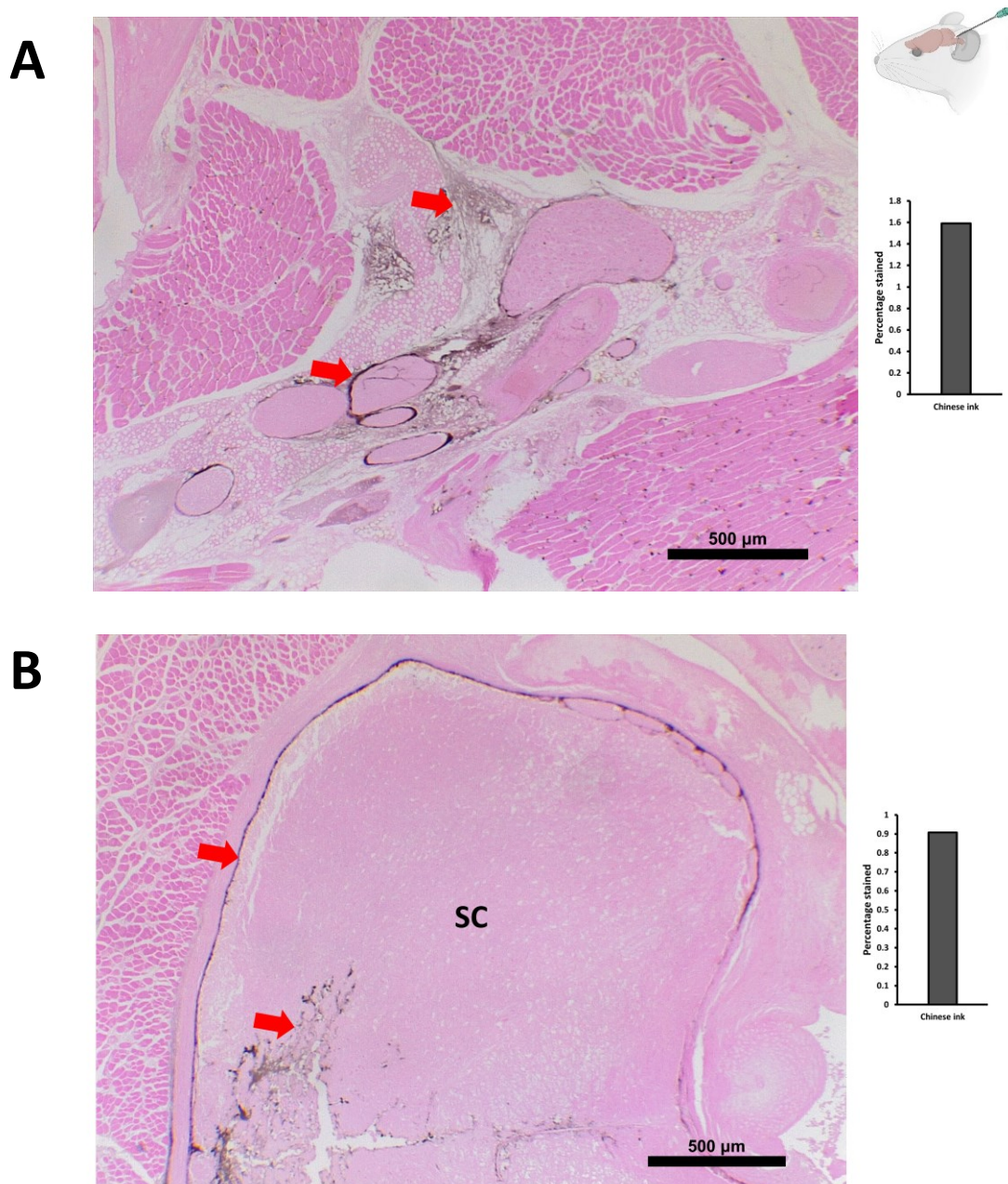


Figure 36. Anterograde flow of Chinese ink in *post-mortem* evaluations. (A) Injection of a Chinese ink solution at the cisterna magna showed staining of cervical lymphatic vessels and connective tissue (red arrows). (B) Nanoparticles were detected in the cervical spinal cord and its surrounding subdural space (red arrows). SC: spinal cord.

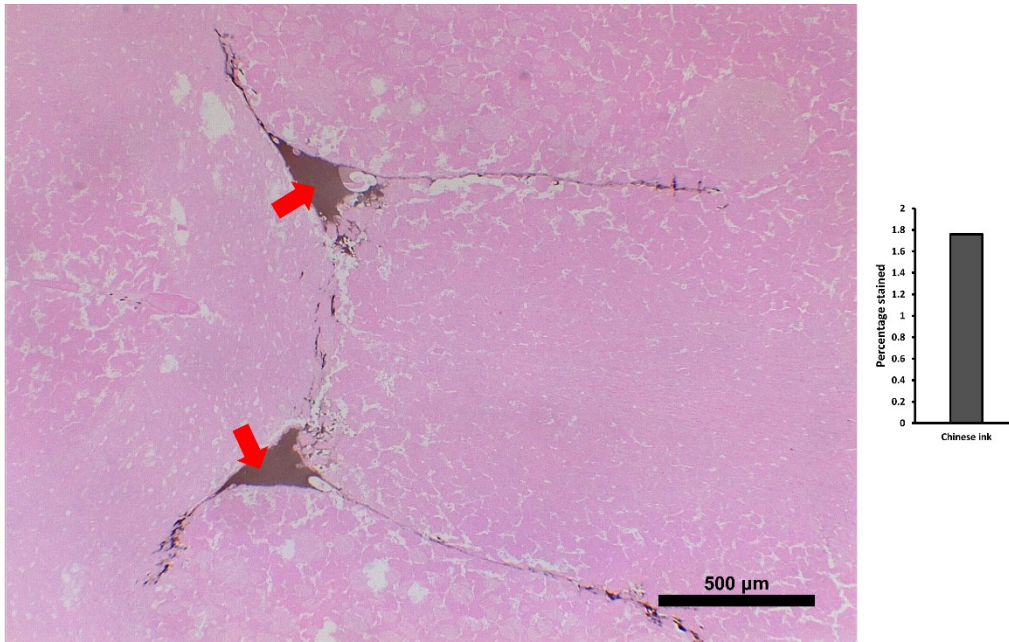


Figure 37. Cephalic structures stained after injection into the cisterna magna of Chinese ink. (A) Nanoparticles within the lateral ventricles.

4.7.10 Anterograde flow evaluation of gold nanoparticles *in vivo*

Anterograde flow in *in vivo* procedures (n=3) of gold nanoparticles after administration into the cisterna magna was confirmed by the detection of Gold Enhancement staining in cervical lymphatic vessels in all mice (Figure 38).

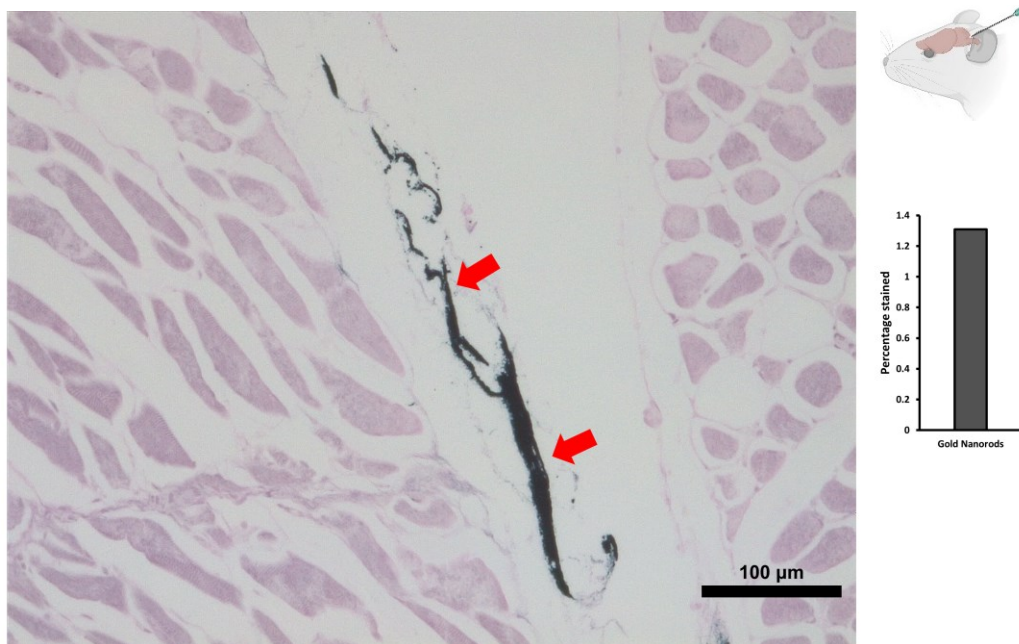
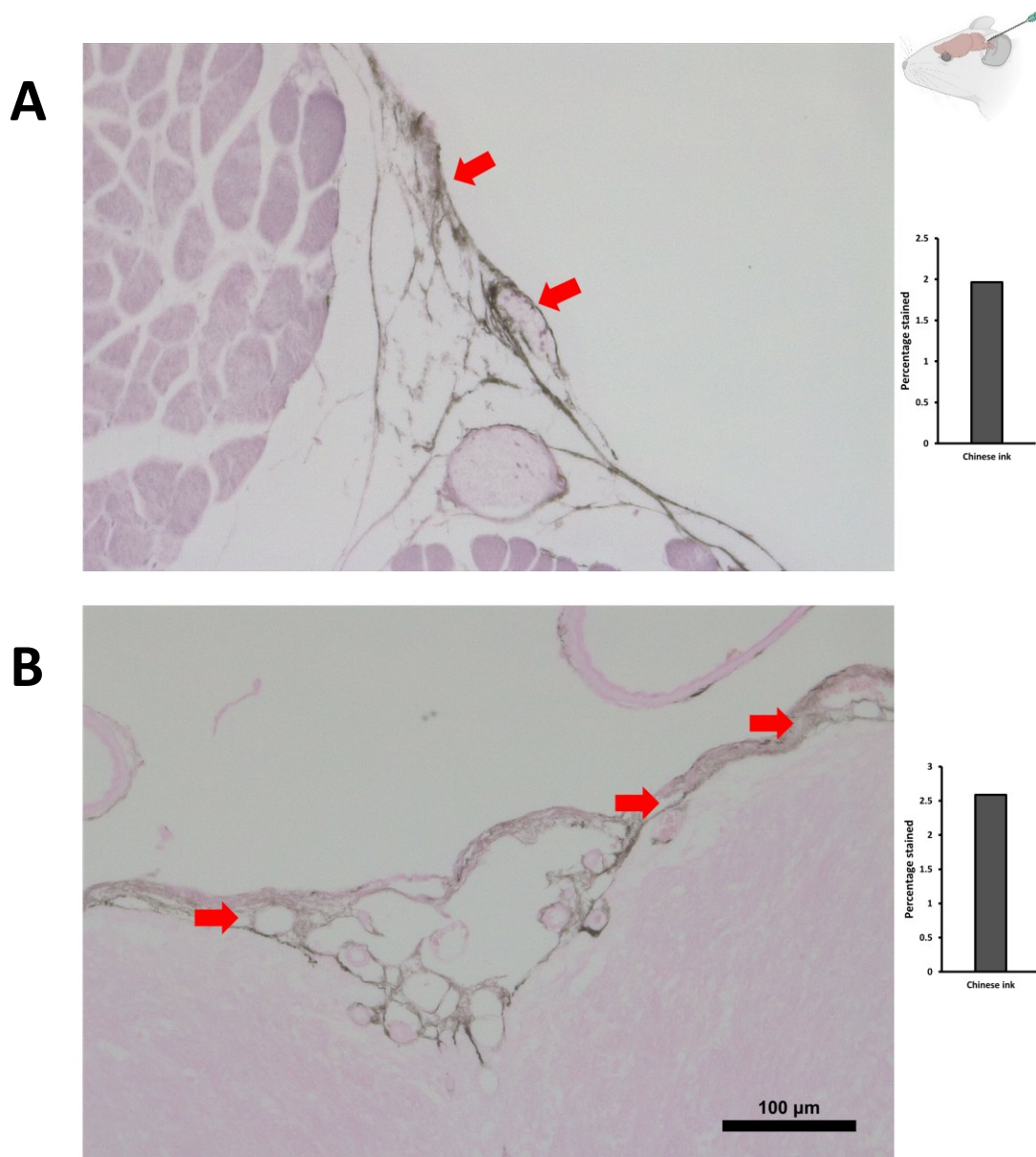


Figure 38. Anterograde flow evaluation of gold nanorods *in vivo*. Gold Enhancement shows staining of lymphatic vessels in the cervical region (red arrows).

4.7.11 Anterograde flow evaluation of Chinese ink *in vivo*

Anterograde flow in *in vivo* procedures (n=3) of Chinese ink nanoparticles after administration into the cisterna magna was confirmed by the detection of staining in cervical lymphatic vessels in all mice (Figure 39A). Chinese ink nanoparticles were also identified in the subarachnoid space (Figure 39B), the cervical spinal cord (Figure 39C), and peripheral nerves (Figure 39C).



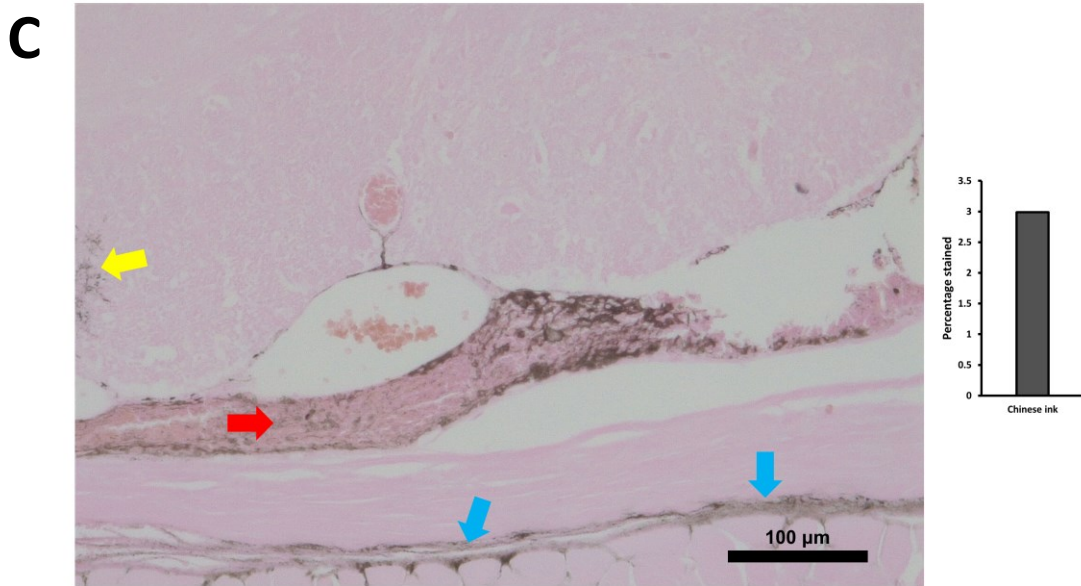


Figure 39. Anterograde flow of Chinese ink in *in vivo* evaluations. (A) Injection of a Chinese ink solution at the cisterna magna showed staining of cervical lymphatic vessels and connective tissue. (B) Nanoparticles were detected in the subarachnoid space. (C) The cervical spinal cord (yellow arrow), peripheral nerves (red arrow), and connective tissue (blue arrows) were identified to contain Chinese ink nanoparticles.

4.7.12 Anterograde flow evaluation of SPIONs and SPION-loaded exosomes *in vivo*

Anterograde flow in *in vivo* procedures (n=3) of SPIONs after administration into the cisterna magna was confirmed by the detection of Perls' Prussian Blue staining in cervical lymphatic vessels in all mice (Figure 40A). At the level of the head, the injection into the cisterna magna also showed staining within the ventricles (Figure 40B). Exosomes loaded with SPIONs did not stain in both the anterograde and retrograde evaluations, as expected for unexposed iron nanoparticles within exosome membranes.

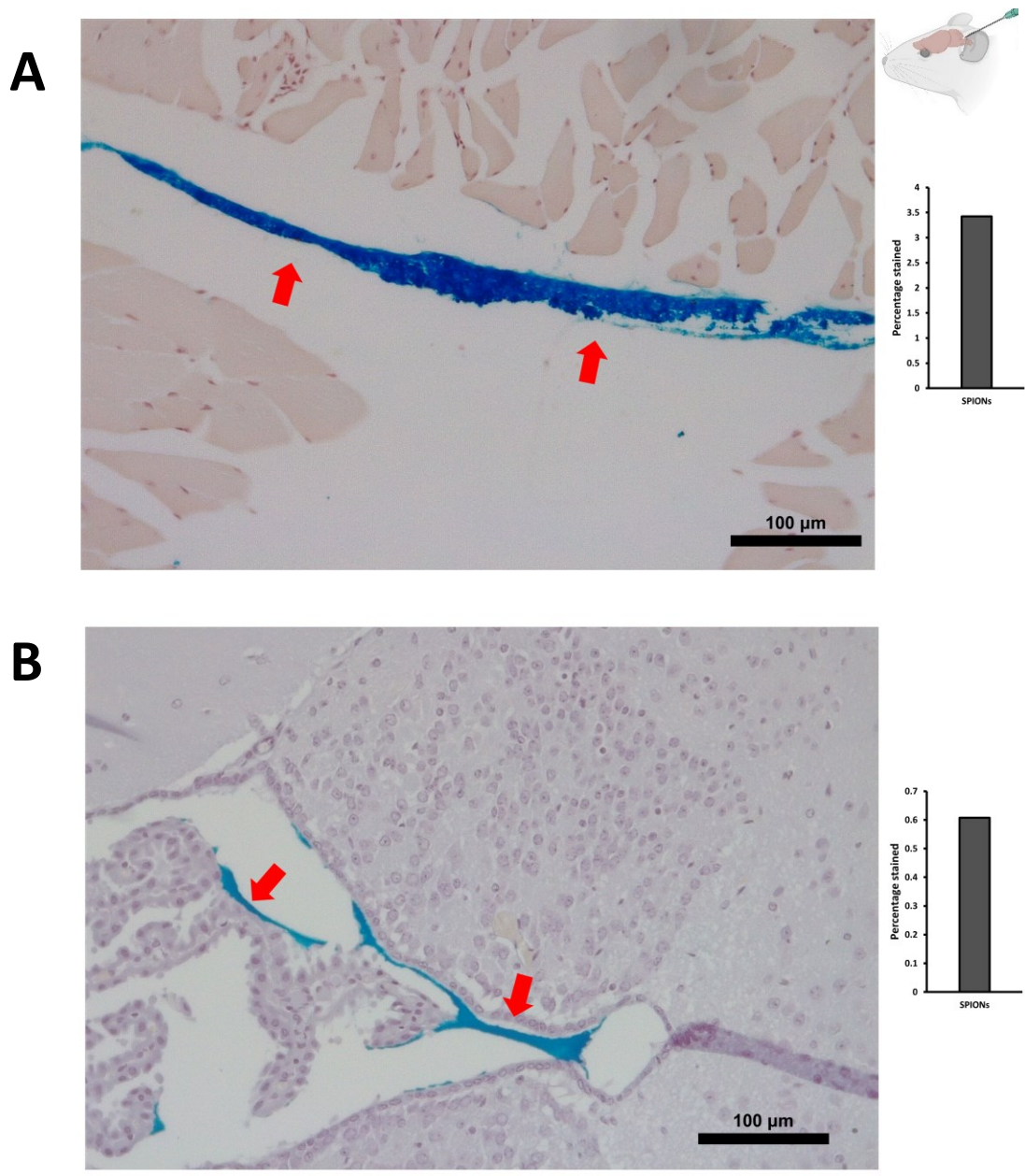


Figure 40. Anterograde flow of SPIONs in in vivo evaluations. (A) Injection of SPIONs at the cisterna magna showed staining of cervical lymphatic vessels. (B) SPIONs were identified within ventricular spaces of the brain.

Chapter 5: Discussion

Understanding the mechanisms used by cancer exosomes to reach the brain is crucial to develop better diagnostic and therapeutic techniques. The field of extracellular vesicles has emerged as a central subject of the medical sciences due to their potential role in many pathological processes(89,100). As highlighted by Wang et al., after a revision of almost five thousand publications in this area, the efforts should be put into mechanism studies, which are predicted to be the next topical issue in exosome research(101). In this regard, as described by Saeedi et al., even though evidence of exosomes bypassing the BBB in a bidirectional manner exists, the exact pathway of crossing remains unclear(100). Therefore, the lymphatic connection to the CNS might contain critical answers to this problem. It is worth highlight that in the process of evaluating the transport of cancer exosomes from the cervical lymphatic vessels to the meningeal lymphatics, we have discovered that the cervical and meningeal lymphatic system can transport nanoparticles not only towards the thorax but can also serve as a way to carry particles towards the brain.

5.1 Reproducibility and repeatability on the connection between the meningeal and cervical lymphatic vessels

Reproducibility of previous findings (89,90) was crucial before attempting to demonstrate the traveling of exosomes from cervical lymphatic vessels to the CNS. *Post-mortem* intracerebroventricular injections with Evans Blue in the cisterna magna of mice confirmed the anatomical connection between CNS spaces and the neck lymphatic system. Repeatability was also achieved in our administrations, as injections in every mouse resulted in stained deep cervical lymph nodes. Further evaluation of the opposite direction by injection of Evans Blue directly into the lymph node also showed the anatomical relationship of cervical lymphatic vessels to the CNS structures. This is the first report that shows that retrograde flow of a dye from this site of cervical lymphatic administration to the CNS is possible in the mouse. Results from Chinese ink injections also showed repeatability in every injected mouse, which becomes highly relevant, as characterization revealed similar size and surface charge properties to exosomes purified from the B16F10 cell line.

5.2 Bidirectional motion of SPIONs, SPION-loaded exosomes, Chinese ink, and gold nanoparticles through the cervical and meningeal lymphatic system

After the *post-mortem* approach demonstrated anatomical relationships between the spaces of interest, the *in vivo* assays performed allow for several conclusions on the behavior of different nanoparticle solutions through the cervical and meningeal lymphatic vessels under physiological conditions. Regarding SPIONs and labeled exosomes, MRI imaging proved that bidirectional motion of these nanoparticles is possible through the cervical and meningeal lymphatic vessels. Hypointense images clearly seen in the T2* maps of mouse brains show the presence of the superparamagnetic signals compared to the homogenous image of control mouse brains. The Perls' Prussian Blue technique only partially confirmed the retrograde flow up to the lymphatic vessels entering the head towards the brain. However, iron detection through this technique is prone to yield false negatives, as the detection requires the accumulation of several hundreds of nm in diameter (102), which could hinder signals from SPIONs smaller than 10 nm diluted in the volume of the brain parenchyma as it occurred in our studies. Incorporation of SPIONs into cells could also prevent their detection by this technique. In fact, lack of detection of exosomes labeled with iron nanoparticles can be explained by the concealing of SPIONs by the membrane of the extracellular vesicles. Perls' Prussian Blue cannot always detect intracellular or iron protected by cellular membranes (102). Therefore, MRI imaging is more sensible for the detection of iron nanoparticles of <10 nm within the brain, which was confirmed in our experiments. Chinese ink and gold nanoparticles *post-mortem* and *in vivo* administrations were consistent with a bidirectional motion through the cervical and meningeal lymphatic system, which adds to the evidence from macroscopic staining of Evans Blue assays and MRI imaging on SPIONs and cancer exosomes labeled with iron nanoparticles.

5.3 Future perspectives of the study

The lymphatic system, including the meningeal lymphatic vessels, has been usually described as a unidirectional transport system of fluid and macromolecules from tissues to venous circulation (91,103). The confirmation of exosome transport from the cervical lymphatic vessels to the brain parenchyma will open a wide range of possibilities for future research and advances in translational medicine. Some areas will be described as

points of reference. However, the scope could include several other potential applications in the theranostic field of nanomedicine.

In oncology, cytotoxicity, distribution, and the ability to cross the BBB have been the all-time obstacles for developing efficient chemotherapy treatments for brain tumors (104). The methodology used for labeling exosomes in this project could be modified to carry drugs through the lymphatic system and improve specific distribution to the brain. Functionalization of nanoparticles for targeting of tumor cells could be used in magnetic nanoparticle hyperthermia for cancer treatment, which has been successfully applied by direct injection to glioblastoma multiforme (105). Further studies can evaluate if an unspecific interstitial injection in the neck could deliver enough nanoparticles through this system to develop noninvasive treatment procedures. Additionally, the use of exosomes in the present study could reveal a similar homing and specialized motion of these vesicles, as seen in the popliteal region of the mouse (94), which would facilitate targeting. Exosome cover could reduce cytotoxicity of nanoparticles, improving the stabilization of new cancer treatments.

Conservative estimates of the global prevalence of brain metastases ranges from 8.5% to 9.6%, based on population studies (106,107). However, autopsy studies on cancer patients have revealed prevalence statistics of 15% to 40% of brain metastases (106–108). Lung, melanoma, breast, colorectal, and renal cell carcinoma are the most common primary sites that produce this kind of cell migration (108). Mortality in these patients would be substantially reduced if cerebral metastatic mechanisms could be prevented. In this regard, results from this study could lead to further investigations for the creation of cancer exosome lymphatic inhibitors, by regulating or blocking movement through these vessels.

An important role different from cancer would be in the field of neurodegenerative diseases. In Huntington's disease, the use of promising peptide inhibitors of polyglutamine aggregation (QBP1, NT17, and PGQ9P2) has been hindered precisely because of poor BBB penetration and low bioavailability (109). A cervical lymphatic route could be an attractive pathway to evaluate more efficient means for accessing the brain without complex nanoparticle constructions. A recent publication by Dominy et al. has associated *P. gingivalis* with Alzheimer's disease (110). Bacterial DNA and RNA found in the brain of patients with this disease could be transported by exosomes through the lymphatic system. Our findings could offer a deeper understanding of this association,

with the possibility of developing treatments to avoid pathological exosomes from reaching the brain and preventing Alzheimer's disease (given the validity of Dominy et al. theory). Other more classical theories of Alzheimer's and nanoparticle theranostic techniques would also benefit from this potential new route of administration.

Other rapidly rising fields, such as the connection between the gut microbiota with diseases such as autism, neurological disorders like multiple sclerosis, and mental disorders, could potentially be sources of new applications for this research (114). Exosomes and the cervical-meningeal lymphatic pathway might play an important part in their association.

Finally, our group at GIMUNICAH has developed a new hypothesis that indicates the probable existence of tumors originating from lymphatic vessels that could be clinically mistaken for meningiomas. We have described a case report that fulfills this profile. We identified a 31-year-old female patient from Honduras with collaboration of the Grupo de Investigación Médica de la Universidad Católica de Honduras (GIMUNICAH). A sample from the tumor was analyzed for RNA sequence at the laboratory of Dr. Vasan Yegnasubramanian at Johns Hopkins University, and immunohistochemistry analysis for confirming protein expression was performed in collaboration with the Pontificia Universidad Católica de Chile and Universidad de Chile at the histology department of ACCDiS. Informed consent and IRB approval from the Universidad Católica de Honduras CEI #COM-2017-002, were obtained for these analyses. RNA sequence lymphatic gene expression and immunohistochemistry analysis can be seen in the Supplementary Table 1. The discovery of the bilateral transport of nanoparticles through the cervical and meningeal lymphatic system will potentially impact the diagnosis and treatment of this newly described tumor of the meningeal lymphatic vessels.

5.4 Conclusion

In conclusion, the cervical and meningeal lymphatic system can transport nanoparticles not only in the classically described lymphatic drainage towards the thorax but can also serve as an access gate to the brain. This newly discovered mechanism for the meningeal lymphatic pathway could be exploited in the theranostic field of nanomedicine to deliver drugs for the treatment of various neurological diseases and the developing of diagnostic contrast media. The understanding of cancer exosome distribution through the cervical

and meningeal lymphatic system will aid in a more profound comprehension of brain metastasis pathophysiology.

References

1. Théry C, Witwer KW, Aikawa E, Alcaraz MJ, Anderson JD, Andriantsitohaina R, et al. Minimal information for studies of extracellular vesicles 2018 (MISEV2018): a position statement of the International Society for Extracellular Vesicles and update of the MISEV2014 guidelines. *J Extracell Vesicles* [Internet]. 2018 Jan 1 [cited 2020 Jul 31];7(1). Available from: [/pmc/articles/PMC6322352/?report=abstract](#)
2. Doyle L, Wang M. Overview of Extracellular Vesicles, Their Origin, Composition, Purpose, and Methods for Exosome Isolation and Analysis. *Cells* [Internet]. 2019 Jul 15 [cited 2020 Jul 31];8(7):727. Available from: [/pmc/articles/PMC6678302/?report=abstract](#)
3. Cocucci E, Meldolesi J. Ectosomes and exosomes: shedding the confusion between extracellular vesicles. *Trends Cell Biol.* 2015 Jun;25(6):364–72.
4. Zhang Y, Liu Y, Liu H, Tang WH. Exosomes: Biogenesis, biologic function and clinical potential [Internet]. Vol. 9, *Cell and Bioscience*. BioMed Central Ltd.; 2019 [cited 2020 Jul 31]. Available from: [/pmc/articles/PMC6377728/?report=abstract](#)
5. Desdín-Micó G, Mittelbrunn M. Role of exosomes in the protection of cellular homeostasis [Internet]. Vol. 11, *Cell Adhesion and Migration*. Taylor and Francis Inc.; 2017 [cited 2020 Jul 31]. p. 127–34. Available from: [/pmc/articles/PMC5351736/?report=abstract](#)
6. Harding C V., Heuser JE, Stahl PD. Exosomes: Looking back three decades and into the future [Internet]. Vol. 200, *Journal of Cell Biology*. The Rockefeller University Press; 2013 [cited 2020 Jul 31]. p. 367–71. Available from: [/pmc/articles/PMC3575527/?report=abstract](#)
7. Raposo G, Stoorvogel W. Extracellular vesicles: Exosomes, microvesicles, and friends [Internet]. Vol. 200, *Journal of Cell Biology*. The Rockefeller University Press; 2013 [cited 2020 Jul 31]. p. 373–83. Available from: [/pmc/articles/PMC3575529/?report=abstract](#)
8. Rajagopal C, Harikumar KB. The Origin and Functions of Exosomes in Cancer. *Front Oncol.* 2018;8:66.
9. Sun W, Luo J-D, Jiang H, Duan DD. Tumor exosomes: a double-edged sword in cancer therapy. *Acta Pharmacol Sin.* 2018 Apr;39(4):534–41.
10. Azmi AS, Bao B, Sarkar FH. Exosomes in cancer development, metastasis, and drug resistance: a comprehensive review. *Cancer Metastasis Rev.* 2013 Dec;32(3–4):623–42.
11. Lee Y, El Andaloussi S, Wood MJA. Exosomes and microvesicles: extracellular vesicles for genetic information transfer and gene therapy. *Hum Mol Genet.* 2012 Oct;21(R1):R125-34.
12. Qin J, Xu Q. Functions and application of exosomes. *Acta Pol Pharm.* 2014;71(4):537–43.
13. Roy S, Hochberg FH, Jones PS. Extracellular vesicles: the growth as diagnostics

- and therapeutics; a survey [Internet]. Vol. 7, *Journal of Extracellular Vesicles*. Taylor and Francis Ltd.; 2018 [cited 2020 Jul 14]. Available from: </pmc/articles/PMC5827771/?report=abstract>
14. Samanta S, Rajasingh S, Drosos N, Zhou Z, Dawn B, Rajasingh J. Exosomes: New molecular targets of diseases [Internet]. Vol. 39, *Acta Pharmacologica Sinica*. Nature Publishing Group; 2018 [cited 2020 Jul 14]. p. 501–13. Available from: </pmc/articles/PMC5888687/?report=abstract>
 15. Zhou X, Xie F, Wang L, Zhang L, Zhang S, Fang M, et al. The function and clinical application of extracellular vesicles in innate immune regulation. *Cell Mol Immunol* [Internet]. 2020;17(4):323–34. Available from: <https://doi.org/10.1038/s41423-020-0391-1>
 16. Xu R, Rai A, Chen M, Suwakulsiri W, Greening DW, Simpson RJ. Extracellular vesicles in cancer — implications for future improvements in cancer care [Internet]. Vol. 15, *Nature Reviews Clinical Oncology*. Nature Publishing Group; 2018 [cited 2020 Jul 14]. p. 617–38. Available from: <http://www.nature.com/articles/s41571-018-0036-9>
 17. Escudier B, Dorval T, Chaput N, André F, Caby M-P, Novault S, et al. Vaccination of metastatic melanoma patients with autologous dendritic cell (DC) derived-exosomes: results of the first phase I clinical trial. *J Transl Med*. 2005 Mar;3(1):10.
 18. Morse MA, Garst J, Osada T, Khan S, Hobeika A, Clay TM, et al. A phase I study of dexosome immunotherapy in patients with advanced non-small cell lung cancer. *J Transl Med*. 2005 Feb;3(1):9.
 19. Besse B, Charrier M, Lapierre V, Dansin E, Lantz O, Planchard D, et al. Dendritic cell-derived exosomes as maintenance immunotherapy after first line chemotherapy in NSCLC. *Oncoimmunology*. 2016 Apr;5(4):e1071008.
 20. Dai S, Wei D, Wu Z, Zhou X, Wei X, Huang H, et al. Phase I clinical trial of autologous ascites-derived exosomes combined with GM-CSF for colorectal cancer. *Mol Ther*. 2008 Apr;16(4):782–90.
 21. Guo M, Wu F, Hu G, Chen L, Xu J, Xu P, et al. Autologous tumor cell-derived microparticle-based targeted chemotherapy in lung cancer patients with malignant pleural effusion. *Sci Transl Med*. 2019 Jan;11(474).
 22. Sun H, Burrola S, Wu J, Ding W-Q. Extracellular Vesicles in the Development of Cancer Therapeutics. *Int J Mol Sci*. 2020 Aug;21(17).
 23. Goetzl EJ, Boxer A, Schwartz JB, Abner EL, Petersen RC, Miller BL, et al. Altered lysosomal proteins in neural-derived plasma exosomes in preclinical Alzheimer disease. *Neurology*. 2015 Jul;85(1):40–7.
 24. Thompson AG, Gray E, Heman-Ackah SM, Mäger I, Talbot K, Andaloussi S El, et al. Extracellular vesicles in neurodegenerative disease — pathogenesis to biomarkers. *Nat Rev Neurol* [Internet]. 2016;12(6):346–57. Available from: <https://doi.org/10.1038/nrneurol.2016.68>
 25. Liu C-G, Song J, Zhang Y-Q, Wang P-C. MicroRNA-193b is a regulator of amyloid precursor protein in the blood and cerebrospinal fluid derived exosomal

- microRNA-193b is a biomarker of Alzheimer's disease. *Mol Med Rep*. 2014 Nov;10(5):2395–400.
26. Lu M, DiBernardo E, Parks E, Fox H, Zheng S-Y, Wayne E. The Role of Extracellular Vesicles in the Pathogenesis and Treatment of Autoimmune Disorders. *Front Immunol*. 2021;12:566299.
 27. Tao S-C, Yuan T, Zhang Y-L, Yin W-J, Guo S-C, Zhang C-Q. Exosomes derived from miR-140-5p-overexpressing human synovial mesenchymal stem cells enhance cartilage tissue regeneration and prevent osteoarthritis of the knee in a rat model. *Theranostics*. 2017;7(1):180–95.
 28. Bai L, Shao H, Wang H, Zhang Z, Su C, Dong L, et al. Effects of Mesenchymal Stem Cell-Derived Exosomes on Experimental Autoimmune Uveitis. *Sci Rep*. 2017 Jun;7(1):4323.
 29. Cai Z, Zhang W, Yang F, Yu L, Yu Z, Pan J, et al. Immunosuppressive exosomes from TGF- β 1 gene-modified dendritic cells attenuate Th17-mediated inflammatory autoimmune disease by inducing regulatory T cells. *Cell research*. 2012. p. 607–10.
 30. Sabanovic B, Piva F, Cecati M, Giuliatti M. Promising Extracellular Vesicle-Based Vaccines against Viruses, Including SARS-CoV-2. *Biology (Basel)*. 2021 Jan;10(2).
 31. Liu D, Li C, Trojanowicz B, Li X, Shi D, Zhan C, et al. CD97 promotion of gastric carcinoma lymphatic metastasis is exosome dependent. *Gastric cancer Off J Int Gastric Cancer Assoc Japanese Gastric Cancer Assoc*. 2016 Jul;19(3):754–66.
 32. Ohshima K, Inoue K, Fujiwara A, Hatakeyama K, Kanto K, Watanabe Y, et al. Let-7 microRNA family is selectively secreted into the extracellular environment via exosomes in a metastatic gastric cancer cell line. *PLoS One*. 2010 Oct;5(10):e13247.
 33. McCready J, Sims JD, Chan D, Jay DG. Secretion of extracellular hsp90alpha via exosomes increases cancer cell motility: a role for plasminogen activation. *BMC Cancer*. 2010 Jun;10:294.
 34. Hoshino A, Costa-Silva B, Shen T-L, Rodrigues G, Hashimoto A, Tesic Mark M, et al. Tumour exosome integrins determine organotropic metastasis. *Nature*. 2015 Nov;527(7578):329–35.
 35. Zhou W, Fong MY, Min Y, Somlo G, Liu L, Palomares MR, et al. Cancer-secreted miR-105 destroys vascular endothelial barriers to promote metastasis. *Cancer Cell*. 2014 Apr;25(4):501–15.
 36. Isola AL, Eddy K, Chen S. Biology, Therapy and Implications of Tumor Exosomes in the Progression of Melanoma. *Cancers (Basel)*. 2016 Dec;8(12).
 37. You Y, Shan Y, Chen J, Yue H, You B, Shi S, et al. Matrix metalloproteinase 13-containing exosomes promote nasopharyngeal carcinoma metastasis. *Cancer Sci*. 2015 Dec;106(12):1669–77.
 38. Hakulinen J, Sankkila L, Sugiyama N, Lehti K, Keski-Oja J. Secretion of active membrane type 1 matrix metalloproteinase (MMP-14) into extracellular space in

- microvesicular exosomes. *J Cell Biochem.* 2008 Dec;105(5):1211–8.
39. Hardesty DA, Nakaji P. The Current and Future Treatment of Brain Metastases. *Front Surg.* 2016;3:30.
 40. Siegel RL, Miller KD, Jemal A. Cancer statistics, 2016. *CA Cancer J Clin.* 2016;66(1):7–30.
 41. Balch CM, Gershenwald JE, Soong S-J, Thompson JF, Atkins MB, Byrd DR, et al. Final version of 2009 AJCC melanoma staging and classification. *J Clin Oncol Off J Am Soc Clin Oncol.* 2009 Dec;27(36):6199–206.
 42. Sloan AE, Nock CJ, Einstein DB. Diagnosis and treatment of melanoma brain metastasis: a literature review. *Cancer Control.* 2009 Jul;16(3):248–55.
 43. McKelvey KJ, Powell KL, Ashton AW, Morris JM, McCracken SA. Exosomes: Mechanisms of Uptake. *J Circ biomarkers.* 2015;4:7.
 44. Mulcahy LA, Pink RC, Carter DRF. Routes and mechanisms of extracellular vesicle uptake. *J Extracell vesicles.* 2014;3.
 45. Zhang J, Li S, Li L, Li M, Guo C, Yao J, et al. Exosome and exosomal microRNA: trafficking, sorting, and function. *Genomics Proteomics Bioinformatics.* 2015 Feb;13(1):17–24.
 46. Margolis L, Sadovsky Y. The biology of extracellular vesicles: The known unknowns. *PLoS Biol [Internet].* 2019 Jul 1 [cited 2020 Jul 14];17(7). Available from: [/pmc/articles/PMC6667152/?report=abstract](https://pubmed.ncbi.nlm.nih.gov/33411111/)
 47. Lino MM, Simões S, Tomatis F, Albino I, Barrera A, Vivien D, et al. Engineered extracellular vesicles as brain therapeutics. *J Control release Off J Control Release Soc.* 2021 Oct;338:472–85.
 48. Morad G, Carman C V., Hagedorn EJ, Perlin JR, Zon LI, Mustafaoglu N, et al. Tumor-Derived Extracellular Vesicles Breach the Intact Blood-Brain Barrier via Transcytosis. *ACS Nano [Internet].* 2019 Dec 24 [cited 2020 Jul 15];13(12):13853–65. Available from: [/pmc/articles/PMC7169949/?report=abstract](https://pubmed.ncbi.nlm.nih.gov/33411111/)
 49. Tominaga N, Kosaka N, Ono M, Katsuda T, Yoshioka Y, Tamura K, et al. Brain metastatic cancer cells release microRNA-181c-containing extracellular vesicles capable of destructing blood-brain barrier. *Nat Commun [Internet].* 2015 Apr 1 [cited 2020 Aug 1];6. Available from: [/pmc/articles/PMC4396394/?report=abstract](https://pubmed.ncbi.nlm.nih.gov/26411111/)
 50. Chen CC, Liu L, Ma F, Wong CW, Guo XE, Chacko J V., et al. Elucidation of Exosome Migration Across the Blood–Brain Barrier Model In Vitro. *Cell Mol Bioeng [Internet].* 2016 Dec 1 [cited 2020 Jul 15];9(4):509–29. Available from: [/pmc/articles/PMC5382965/?report=abstract](https://pubmed.ncbi.nlm.nih.gov/26411111/)
 51. Matsumoto J, Stewart T, Sheng L, Li N, Bullock K, Song N, et al. Transmission of α -synuclein-containing erythrocyte-derived extracellular vesicles across the blood-brain barrier via adsorptive mediated transcytosis: another mechanism for initiation and progression of Parkinson’s disease? *Acta Neuropathol Commun [Internet].* 2017 Sep 13 [cited 2020 Jul 15];5(1):71. Available from: [/pmc/articles/PMC5598000/?report=abstract](https://pubmed.ncbi.nlm.nih.gov/26411111/)

52. Kuroda H, Tachikawa M, Yagi Y, Umetsu M, Nurdin A, Miyauchi E, et al. Cluster of Differentiation 46 Is the Major Receptor in Human Blood-Brain Barrier Endothelial Cells for Uptake of Exosomes Derived from Brain-Metastatic Melanoma Cells (SK-Mel-28). *Mol Pharm*. 2019 Jan;16(1):292–304.
53. Daneman R, Prat A. The blood–brain barrier. *Cold Spring Harb Perspect Biol* [Internet]. 2015 Jan 1 [cited 2020 Jul 15];7(1). Available from: [/pmc/articles/PMC4292164/?report=abstract](https://www.ncbi.nlm.nih.gov/pmc/articles/PMC4292164/?report=abstract)
54. Tominaga N, Kosaka N, Ono M, Katsuda T, Yoshioka Y, Tamura K, et al. Brain metastatic cancer cells release microRNA-181c-containing extracellular vesicles capable of destructing blood-brain barrier. *Nat Commun* [Internet]. 2015 Apr 1 [cited 2020 Sep 4];6. Available from: [/pmc/articles/PMC4396394/?report=abstract](https://www.ncbi.nlm.nih.gov/pmc/articles/PMC4396394/?report=abstract)
55. Foroozandeh P, Aziz AA. Insight into Cellular Uptake and Intracellular Trafficking of Nanoparticles. *Nanoscale Res Lett* [Internet]. 2018;13(1):339. Available from: <https://doi.org/10.1186/s11671-018-2728-6>
56. Tuma PL, Hubbard AL. Transcytosis: crossing cellular barriers. *Physiol Rev*. 2003 Jul;83(3):871–932.
57. Matsumoto J, Stewart T, Banks WA, Zhang J. The Transport Mechanism of Extracellular Vesicles at the Blood-Brain Barrier. *Curr Pharm Des*. 2017;23(40):6206–14.
58. Abbott NJ, Rönnbäck L, Hansson E. Astrocyte–endothelial interactions at the blood–brain barrier. *Nat Rev Neurosci* [Internet]. 2006;7(1):41–53. Available from: <https://doi.org/10.1038/nrn1824>
59. Fiandaca MS, Kapogiannis D, Mapstone M, Boxer A, Eitan E, Schwartz JB, et al. Identification of preclinical Alzheimer’s disease by a profile of pathogenic proteins in neurally derived blood exosomes: A case-control study. *Alzheimer’s Dement* [Internet]. 2015 Jun 1 [cited 2020 Sep 5];11(6):600–607.e1. Available from: [/pmc/articles/PMC4329112/?report=abstract](https://www.ncbi.nlm.nih.gov/pmc/articles/PMC4329112/?report=abstract)
60. Winston CN, Goetzl EJ, Akers JC, Carter BS, Rockenstein EM, Galasko D, et al. Prediction of conversion from mild cognitive impairment to dementia with neuronally derived blood exosome protein profile. *Alzheimer’s Dement Diagnosis, Assess Dis Monit* [Internet]. 2016 [cited 2020 Sep 5];3:63–72. Available from: [/pmc/articles/PMC4925777/?report=abstract](https://www.ncbi.nlm.nih.gov/pmc/articles/PMC4925777/?report=abstract)
61. Abner EL, Jicha GA, Shaw LM, Trojanowski JQ, Goetzl EJ. Plasma neuronal exosomal levels of Alzheimer’s disease biomarkers in normal aging. *Ann Clin Transl Neurol* [Internet]. 2016 May 1 [cited 2020 Sep 5];3(5):399–403. Available from: [/pmc/articles/PMC4863753/?report=abstract](https://www.ncbi.nlm.nih.gov/pmc/articles/PMC4863753/?report=abstract)
62. Goetzl EJ, Abner EL, Jicha GA, Kapogiannis D, Schwartz JB. Declining levels of functionally specialized synaptic proteins in plasma neuronal exosomes with progression of Alzheimer’s disease. *FASEB J* [Internet]. 2018 Feb 1 [cited 2020 Sep 5];32(2):888–93. Available from: [/pmc/articles/PMC5888398/?report=abstract](https://www.ncbi.nlm.nih.gov/pmc/articles/PMC5888398/?report=abstract)
63. Goetzl EJ, Boxer A, Schwartz JB, Abner EL, Petersen RC, Miller BL, et al. Low neural exosomal levels of cellular survival factors in Alzheimer’s disease. *Ann*

- Clin Transl Neurol [Internet]. 2015 Jul 1 [cited 2020 Sep 5];2(7):769–73. Available from: [/pmc/articles/PMC4531059/?report=abstract](#)
64. Shi M, Liu C, Cook TJ, Bullock KM, Zhao Y, Gingham C, et al. Plasma exosomal α -synuclein is likely CNS-derived and increased in Parkinson's disease. *Acta Neuropathol* [Internet]. 2014 [cited 2020 Aug 19];128(5):639–50. Available from: [/pmc/articles/PMC4201967/?report=abstract](#)
 65. Norman M, Ter-Ovanesyan D, Trieu W, Lazarovits R, Kowal EJK, Lee JH, et al. L1CAM is not associated with extracellular vesicles in human cerebrospinal fluid or plasma. *Nat Methods* [Internet]. 2021;18(6):631–4. Available from: <https://doi.org/10.1038/s41592-021-01174-8>
 66. Record M, Subra C, Silvente-Poirot S, Poirot M. Exosomes as intercellular signalosomes and pharmacological effectors. *Biochem Pharmacol*. 2011 May;81(10):1171–82.
 67. Chertova E, Chertov O, Coren L V, Roser JD, Trubey CM, Bess JWJ, et al. Proteomic and biochemical analysis of purified human immunodeficiency virus type 1 produced from infected monocyte-derived macrophages. *J Virol*. 2006 Sep;80(18):9039–52.
 68. Izquierdo-Useros N, Naranjo-Gómez M, Archer J, Hatch SC, Erkizia I, Blanco J, et al. Capture and transfer of HIV-1 particles by mature dendritic cells converges with the exosome-dissemination pathway. *Blood*. 2009 Mar;113(12):2732–41.
 69. García-Romero N, Carrión-Navarro J, Esteban-Rubio S, Lázaro-Ibáñez E, Peris-Celda M, Alonso MM, et al. DNA sequences within glioma-derived extracellular vesicles can cross the intact blood-brain barrier and be detected in peripheral blood of patients. *Oncotarget* [Internet]. 2017 [cited 2020 Sep 4];8(1):1416–28. Available from: [/pmc/articles/PMC5352065/?report=abstract](#)
 70. Banks WA, Sharma P, Bullock KM, Hansen KM, Ludwig N, Whiteside TL. Transport of Extracellular Vesicles across the Blood-Brain Barrier: Brain Pharmacokinetics and Effects of Inflammation. *Int J Mol Sci* [Internet]. 2020 Jun 21 [cited 2020 Sep 5];21(12). Available from: [/pmc/articles/PMC7352415/?report=abstract](#)
 71. Jeong J-Y, Kwon H-B, Ahn J-C, Kang D, Kwon S-H, Park JA, et al. Functional and developmental analysis of the blood-brain barrier in zebrafish. *Brain Res Bull*. 2008 Mar;75(5):619–28.
 72. Eliceiri BP, Gonzalez AM, Baird A. Zebrafish model of the blood-brain barrier: morphological and permeability studies. *Methods Mol Biol* [Internet]. 2011 [cited 2020 Aug 19];686:371–8. Available from: [/pmc/articles/PMC4222041/?report=abstract](#)
 73. Fleming A, Diekmann H, Goldsmith P. Functional Characterisation of the Maturation of the Blood-Brain Barrier in Larval Zebrafish. *PLoS One* [Internet]. 2013 Oct 16 [cited 2020 Aug 19];8(10):77548. Available from: [/pmc/articles/PMC3797749/?report=abstract](#)
 74. Umans RA, Henson HE, Mu F, Parupalli C, Ju B, Peters JL, et al. CNS angiogenesis and barrierogenesis occur simultaneously. *Dev Biol* [Internet]. 2017 May 15 [cited 2020 Aug 19];425(2):101–8. Available from:

/pmc/articles/PMC5682946/?report=abstract

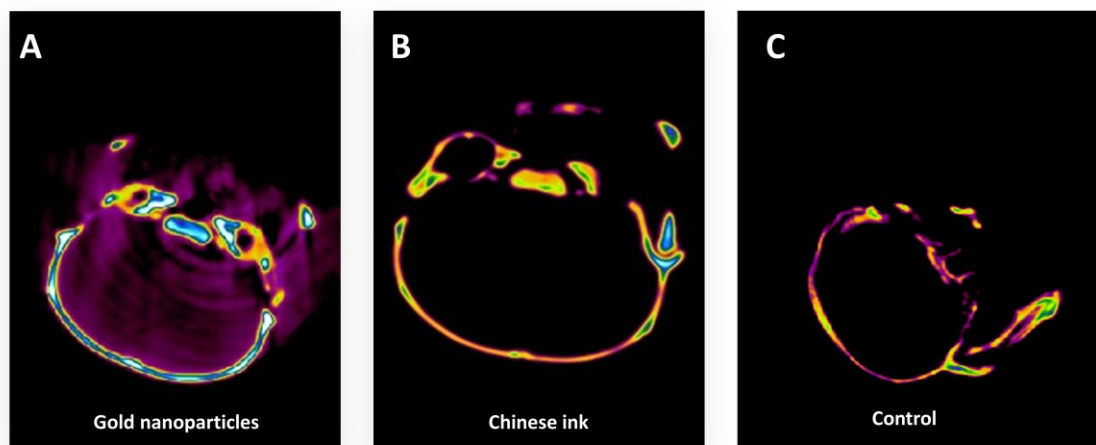
75. O’Brown NM, Megason SG, Chenghua G. Suppression of transcytosis regulates zebrafish blood-brain barrier function. *Elife*. 2019 Aug 1;8.
76. O’Brown NM, Pfau SJ, Gu C. Bridging barriers: A comparative look at the blood-brain barrier across organisms [Internet]. Vol. 32, *Genes and Development*. Cold Spring Harbor Laboratory Press; 2018 [cited 2020 Aug 19]. p. 466–78. Available from: /pmc/articles/PMC5959231/?report=abstract
77. Wang YY, Pan LY, Moens CB, Appel B. Notch3 establishes brain vascular integrity by regulating pericyte number. *Dev* [Internet]. 2014 Jan 15 [cited 2020 Aug 19];141(2):307–17. Available from: /pmc/articles/PMC3879812/?report=abstract
78. Ando K, Fukuhara S, Izumi N, Nakajima H, Fukui H, Kelsh RN, et al. Clarification of mural cell coverage of vascular endothelial cells by live imaging of zebrafish. *Dev* [Internet]. 2016 Apr 15 [cited 2020 Aug 19];143(8):1328–39. Available from: /pmc/articles/PMC4852519/?report=abstract
79. Bergwerff M, Verberne ME, DeRuiter MC, Poelmann RE, Gittenberger-de Groot AC. Neural crest cell contribution to the developing circulatory system: implications for vascular morphology? *Circ Res*. 1998 Feb;82(2):221–31.
80. Etchevers HC, Vincent C, Le Douarin NM, Couly GF. The cephalic neural crest provides pericytes and smooth muscle cells to all blood vessels of the face and forebrain. *Development*. 2001 Apr;128(7):1059–68.
81. Korn J, Christ B, Kurz H. Neuroectodermal origin of brain pericytes and vascular smooth muscle cells. *J Comp Neurol*. 2002 Jan;442(1):78–88.
82. Wilm B, Ipenberg A, Hastie ND, Burch JBE, Bader DM. The serosal mesothelium is a major source of smooth muscle cells of the gut vasculature. *Development*. 2005 Dec;132(23):5317–28.
83. Que J, Wilm B, Hasegawa H, Wang F, Bader D, Hogan BLM. Mesothelium contributes to vascular smooth muscle and mesenchyme during lung development. *Proc Natl Acad Sci U S A* [Internet]. 2008 Oct 28 [cited 2020 Aug 19];105(43):16626–30. Available from: /pmc/articles/PMC2567908/?report=abstract
84. Asahina K, Zhou B, Pu WT, Tsukamoto H. Septum transversum-derived mesothelium gives rise to hepatic stellate cells and perivascular mesenchymal cells in developing mouse liver. *Hepatology* [Internet]. 2011 Mar [cited 2020 Aug 19];53(3):983–95. Available from: /pmc/articles/PMC3078645/?report=abstract
85. Yamanishi E, Takahashi M, Saga Y, Osumi N. Penetration and differentiation of cephalic neural crest-derived cells in the developing mouse telencephalon. *Dev Growth Differ*. 2012 Dec;54(9):785–800.
86. Grupp L, Wolburg H, Mack AF. Astroglial structures in the zebrafish brain. *J Comp Neurol*. 2010 Nov;518(21):4277–87.
87. Grapp M, Wrede A, Schweizer M, Hüwel S, Galla H-J, Snaidero N, et al. Choroid plexus transcytosis and exosome shuttling deliver folate into brain

- parenchyma. *Nat Commun*. 2013;4:2123.
88. Mezey É, Palkovits M. Neuroanatomy: Forgotten findings of brain lymphatics. Vol. 524, *Nature*. England; 2015. p. 415.
 89. Louveau A, Smirnov I, Keyes TJ, Eccles JD, Rouhani SJ, Peske JD, et al. Structural and functional features of central nervous system lymphatic vessels. *Nature*. 2015 Jul;523(7560):337–41.
 90. Aspelund A, Antila S, Proulx ST, Karlsen TV, Karaman S, Detmar M, et al. A dural lymphatic vascular system that drains brain interstitial fluid and macromolecules. *J Exp Med*. 2015 Jun;212(7):991–9.
 91. Hershenhouse KS, Shaully O, Gould DJ, Patel KM. Meningeal Lymphatics: A Review and Future Directions From a Clinical Perspective. *Neurosci insights*. 2019;14:1179069519889027.
 92. Ha S-K, Nair G, Absinta M, Luciano NJ, Reich DS. Magnetic Resonance Imaging and Histopathological Visualization of Human Dural Lymphatic Vessels. *Bio-protocol*. 2018 Apr;8(8).
 93. Absinta M, Ha S-K, Nair G, Sati P, Luciano NJ, Palisoc M, et al. Human and nonhuman primate meninges harbor lymphatic vessels that can be visualized noninvasively by MRI. *Elife*. 2017 Oct;6.
 94. Hu L, Wickline SA, Hood JL. Magnetic resonance imaging of melanoma exosomes in lymph nodes. *Magn Reson Med* [Internet]. 2015 Jul 1 [cited 2020 Dec 29];74(1):266–71. Available from: [/pmc/articles/PMC4422779/?report=abstract](https://pubmed.ncbi.nlm.nih.gov/26011111/)
 95. Da Mesquita S, Louveau A, Vaccari A, Smirnov I, Cornelison RC, Kingsmore KM, et al. Functional aspects of meningeal lymphatics in ageing and Alzheimer’s disease. *Nature*. 2018 Aug;560(7717):185–91.
 96. Ahn JH, Cho H, Kim J-H, Kim SH, Ham J-S, Park I, et al. Meningeal lymphatic vessels at the skull base drain cerebrospinal fluid. *Nature*. 2019 Aug;572(7767):62–6.
 97. CAO Q, WANG S, XU K, LIU X, LIU L. Experimental Study of Chinese Ink as a New Type of Dye Tracer in Sentinel Lymph Node Biopsy. *Chinese-German J Clin Oncol* [Internet]. 2006;5(1):36–9. Available from: <https://doi.org/10.1007/s10330-005-0434-1>
 98. Mori K. Identification of lymphatic vessels after intra-arterial injection of dyes and other substances. *Microvasc Res* [Internet]. 1969;1(3):268–74. Available from: <https://www.sciencedirect.com/science/article/pii/0026286269900296>
 99. Kato S, Shirai Y, Sakamoto M, Mori S, Kodama T. Use of a Lymphatic Drug Delivery System and Sonoporation to Target Malignant Metastatic Breast Cancer Cells Proliferating in the Marginal Sinuses. *Sci Rep* [Internet]. 2019;9(1):13242. Available from: <https://doi.org/10.1038/s41598-019-49386-5>
 100. Saeedi S, Israel S, Nagy C, Turecki G. The emerging role of exosomes in mental disorders. *Transl Psychiatry* [Internet]. 2019;9(1):122. Available from: <https://doi.org/10.1038/s41398-019-0459-9>

101. Wang B, Xing D, Zhu Y, Dong S, Zhao B. The State of Exosomes Research: A Global Visualized Analysis. *Biomed Res Int.* 2019;2019:1495130.
102. Curdt F, Haase K, Ziegenbalg L, Greb H, Heyers D, Winklhofer M. Prussian blue technique is prone to yield false negative results in magnetoreception research. *Sci Rep [Internet].* 2022;12(1):8803. Available from: <https://doi.org/10.1038/s41598-022-12398-9>
103. Jiang H, Wei H, Zhou Y, Xiao X, Zhou C, Ji X. Overview of the meningeal lymphatic vessels in aging and central nervous system disorders. *Cell Biosci [Internet].* 2022;12(1):202. Available from: <https://doi.org/10.1186/s13578-022-00942-z>
104. Kang C, Sun Y, Zhu J, Li W, Zhang A, Kuang T, et al. Delivery of Nanoparticles for Treatment of Brain Tumor. *Curr Drug Metab.* 2016;17(8):745–54.
105. Giustini AJ, Petryk AA, Cassim SM, Tate JA, Baker I, Hoopes PJ. MAGNETIC NANOPARTICLE HYPERTHERMIA IN CANCER TREATMENT. *Nano Life.* 2010 Mar;1(1n02).
106. Nayak L, Lee EQ, Wen PY. Epidemiology of brain metastases. *Curr Oncol Rep.* 2012 Feb;14(1):48–54.
107. Tabouret E, Chinot O, Metellus P, Tallet A, Viens P, Gonçalves A. Recent trends in epidemiology of brain metastases: an overview. *Anticancer Res.* 2012 Nov;32(11):4655–62.
108. Achrol AS, Rennert RC, Anders C, Soffiatti R, Ahluwalia MS, Nayak L, et al. Brain metastases. *Nat Rev Dis Prim.* 2019 Jan;5(1):5.
109. Joshi AS, Singh V, Gahane A, Thakur AK. Biodegradable Nanoparticles Containing Mechanism Based Peptide Inhibitors Reduce Polyglutamine Aggregation in Cell Models and Alleviate Motor Symptoms in a *Drosophila* Model of Huntington's Disease. *ACS Chem Neurosci.* 2019 Mar;10(3):1603–14.
110. Dominy SS, Lynch C, Ermini F, Benedyk M, Marczyk A, Konradi A, et al. *Porphyromonas gingivalis* in Alzheimer's disease brains: Evidence for disease causation and treatment with small-molecule inhibitors. *Sci Adv.* 2019 Jan;5(1):eaau3333.
111. Morales-Zavala F, Arriagada H, Hassan N, Velasco C, Riveros A, Álvarez AR, et al. Peptide multifunctionalized gold nanorods decrease toxicity of β -amyloid peptide in a *Caenorhabditis elegans* model of Alzheimer's disease. *Nanomedicine.* 2017 Oct;13(7):2341–50.
112. Prades R, Guerrero S, Araya E, Molina C, Salas E, Zurita E, et al. Delivery of gold nanoparticles to the brain by conjugation with a peptide that recognizes the transferrin receptor. *Biomaterials.* 2012 Oct;33(29):7194–205.
113. Ruff J, Hüwel S, Kogan MJ, Simon U, Galla H-J. The effects of gold nanoparticles functionalized with β -amyloid specific peptides on an in vitro model of blood-brain barrier. *Nanomedicine.* 2017 Jul;13(5):1645–52.
114. Ahmadi Badi S, Moshiri A, Fateh A, Rahimi Jamnani F, Sarshar M, Vaziri F, et al. Microbiota-Derived Extracellular Vesicles as New Systemic Regulators. *Front Microbiol.* 2017;8:1610.

Supplementary Material

1. MicroCT analysis of the retrograde flow of gold nanoparticles from the cervical lymphatic vessels to the brain.



Supplementary Figure 1. MicroCT scan analysis of the retrograde flow of gold nanoparticles from the cervical lymphatic vessels to the brain. (A) Hypodense signal distributed throughout the brain of the mouse injected with gold nanoparticles. (B) No signal was observed in the brain of the Chinese ink injected mouse. (C) No signal was observed in the control mouse with no solution administered.

An injection of 10 μL of a solution of gold nanoparticles was performed at the deep cervical lymph node of a C57BL/6 mouse *in vivo* ($n=1$). This was compared by MicroCT analysis to a mouse injected with 10 μL of a 10% Chinese ink solution ($n=1$), and a control animal with no injection. Hypodense signals were detected within the skull of the mouse through the mouse brain (Supplementary Figure 1A). No signal was observed in the brains of the Chinese ink mouse and control animal.

2. Transcriptome analysis on tumor sample.

Supplementary Table 1. Transcriptome analysis of a meningeal lymphatic tumor (Genes associated with lymphatic system)

Gene ID	Transcripts per Million (TPM)
VEGFA	51.160
VEGFC	1.290
TIE1	4.660
CXADR	38.280
TLR2	55.310
TLR4	16.86
FGFR1	87.820
FGFR2	6.910
FGFR3	41.000
EDNRB	41.560
IGF1R	84.850
IGF2R	123.350
PDGFRA	3.800
PDGFRB	65.550
HGF	4.930
IL20RA	1.290
IL20RB	2.280
IL22RA1	0.100
IL22RA2	0.060
ITGA1	50.530
ITGA9	10.750
PTK2	73.160
F11R(JAM1)	14.210
JAM2	583.200
JAM3	425.930
PECAM1	18.920
ICAM1	20.540
LGALS8 (Galectin-8)	30.140
CCL2	20.780
CXCL12	37.320
CCL5 (RANTES)	4.780
CXCR4	65.660
CCR7	0.070
ANGPT2	7.360
TEK (Tie2)	16.350
TGFBI	48.420
FOXC2	68.300
PPP1R13B(ASPP1)	16.700
YKT6	28.190
STX1A	1.550

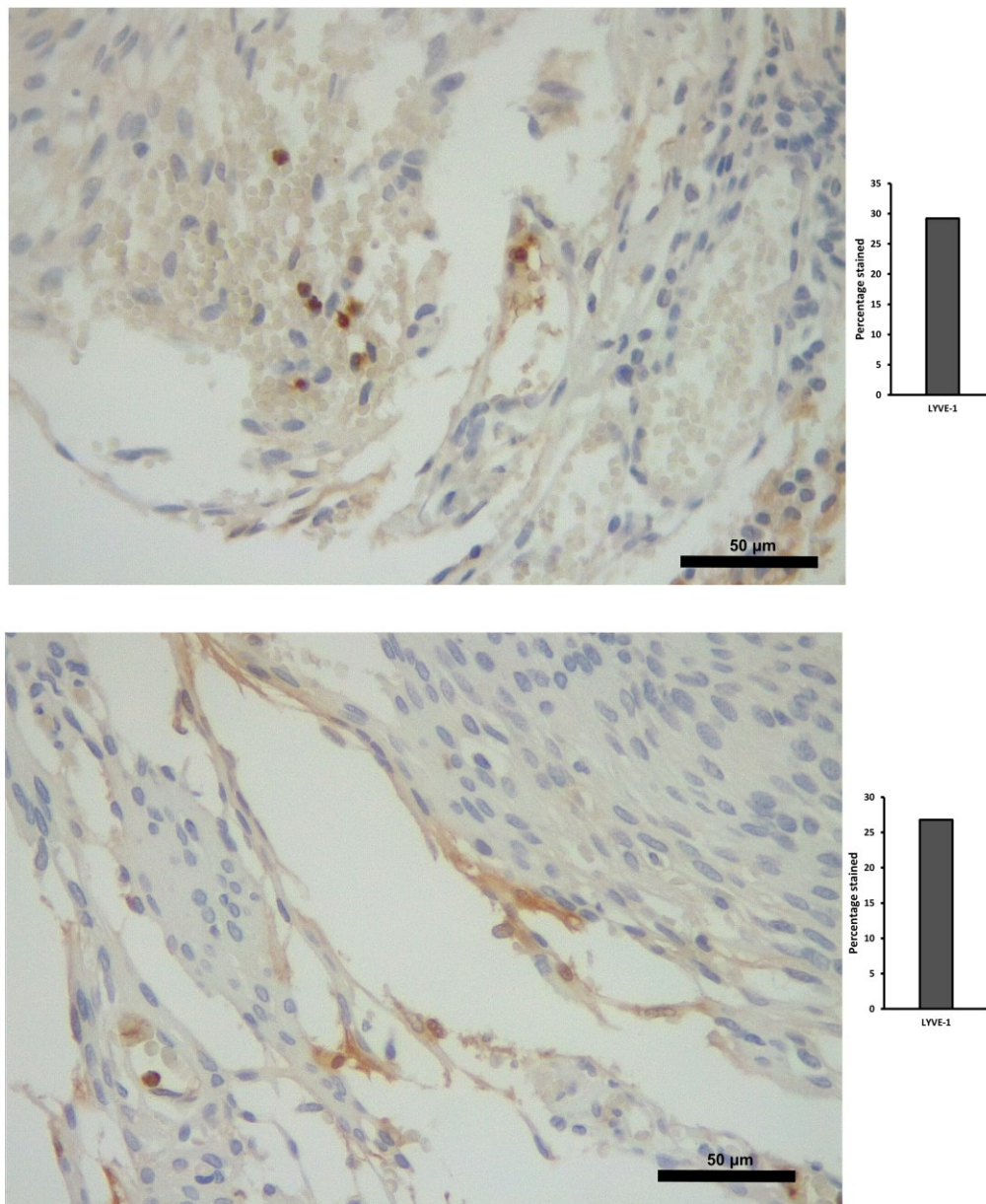
STX1B	0.250
STX2	23.520
STX3	4.180
STX4	36.550
STX5	38.000
STX6	18.160
STX7	80.170
STX8	51.290
STX10	28.120
STX11	2.920
STX12	52.220
STX16	45.520
STX17	24.330
STX18	23.830
STX19	0.280
NFATC1	3.600
THY1	24.820
NOS3	3.910
NOS2	0.620
NOSTRIN	11.330
CAV1	42.200
AKT1	82.270
NOS1	0.070
HSP90AA1	621.830
ACE	7.700
NOSIP	51.450
MTHFR	26.990
KDR	18.160
VWF(FVIIIIRA)	92.540
PLAT (tPA)	14.710
SERPINE1(PAI-1)	33.250
SEMA4C	11.640
FDCSP(C4orf7)	0
TBXA2R	1.940
CD34	12.200
EFNB2(efrin B2)	44.620
SOX18	6.630
CHRNA1	0.080
FGF2(bFGF)	31.090
TNF	8.780
ADM (adrenomedullin)	57.740
IL7	0.080
TGFB1	21.780
COL18A1	22.760
EMILIN1	59.060

Most characteristic lymphatic markers

Gene ID	Transcripts per Million (TPM)
PROX1	0.660
PDPN	53.650
FLT4 (VEGFR3)	4.050
LYVE1	6.470
NT5E	259.960
DSP	648.580
DPP4	0.520
CCL21	0.190
CCL20	0
NRP2	134.130
MRC1	12.170
ITGA9	10.750
ACKR2	3.820

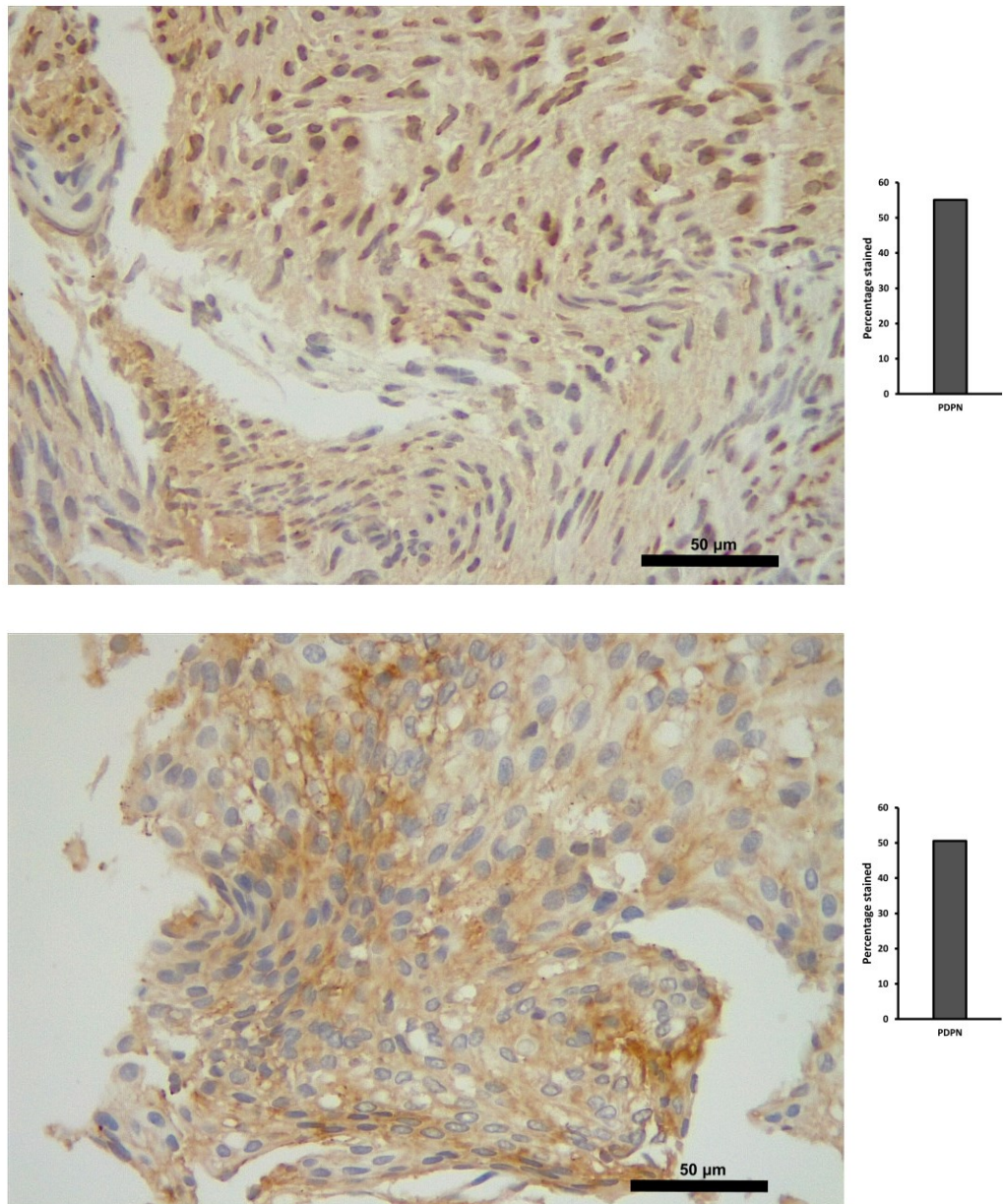
3. Immunohistochemistry of four positive lymphatic markers performed on the meningeal lymphatic tumor sample.

3.1 LYVE-1



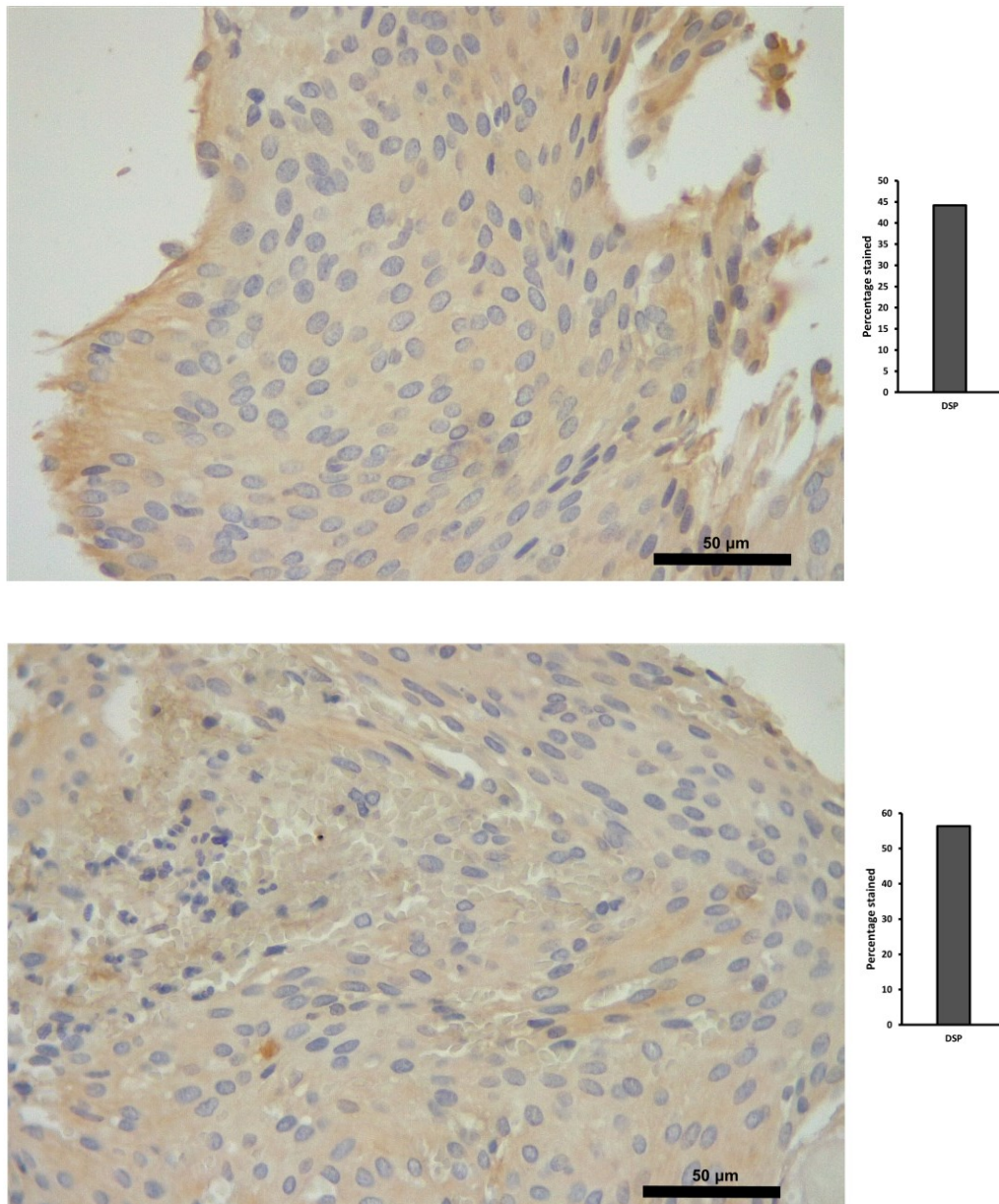
Supplementary Figure 2. Immunohistochemistry analysis for LYVE-1 on a meningeal lymphatic tumor sample.

3.2 PDPN



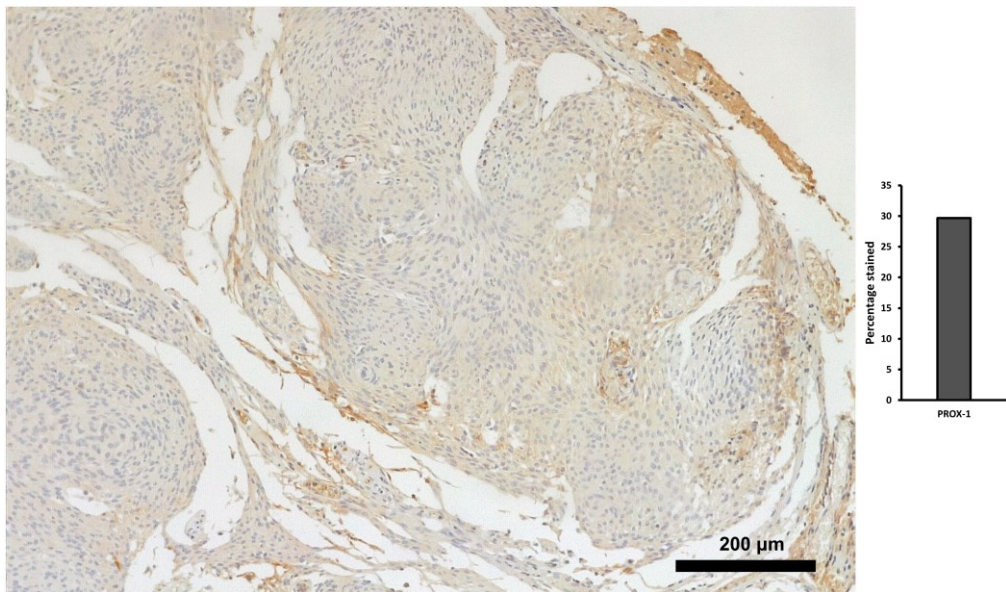
Supplementary Figure 3. Immunohistochemistry analysis for PDPN on a meningeal lymphatic tumor sample.

3.3 DSP



Supplementary Figure 4. Immunohistochemistry analysis for DSP on a meningeal lymphatic tumor sample.

3.4 PROX1



Supplementary Figure 5. Immunohistochemistry analysis for PROX-1 on a meningeal lymphatic tumor sample.